Simulating Miocene Warmth: Insights From an Opportunistic Multi-Model Ensemble (MioMIP1)

N. Burls, C. Bradshaw, A. de Boer, N. Herold, M. Huber, M. Pound, Yannick Donnadieu, A. Farnsworth, A. Frigola, E. Gasson, et al.

Paleoceanography and Paleoclimatology

RESEARCH ARTICLE
10.1029/2020PA004054

Special Section:
The Miocene: The Future of the Past

Simulating Miocene Warmth: Insights From an Opportunistic Multi-Model Ensemble (MioMIP1)

N. J. Burls[1], C. D. Bradshaw[2,3], A. M. De Boer[4], N. Herold[5], M. Huber[6], M. Pound[7], Y. Donnadieu[8], A. Farnsworth[9], A. Frigola[10], E. Gasson[11], A. S. von der Heydt[12], D. K. Hutchinson[4], G. Knorr[13], K. T. Lawrence[14], C. H. Lear[15], X. Li[16], G. Lohmann[13], D. J. Lunt[11], A. Marzocchi[17], M. Prange[10], C. A. Riihimaki[18], A.-C. Sarr[8], N. Siler[19], and Z. Zhang[16,20]

[1]Department of Atmospheric, Oceanic and Earth Sciences, Center for Ocean-Land-Atmosphere Studies, George Mason University, Fairfax, VA, USA, [2]Met Office Hadley Centre, Exeter, UK, [3]The Global Systems Institute, University of Exeter, Exeter, UK, [4]Department of Geological Sciences, Bolin Center for Climate Research, Stockholm University, Stockholm, Sweden, [5]Science Division, The NSW Department of Planning, Industry and Environment, Climate and Atmospheric Science, Parramatta, NSW, Australia, [6]Department of Earth, Atmospheric, and Planetary Sciences, Purdue University, West Lafayette, IN, USA, [7]Department of Geography and Environmental Sciences, Northumbria University, Newcastle, UK, [8]Aix Marseille University, CNRS, IRD, Coll France, INRA, CEREGE, Aix en Provence, France, [9]School of Geographical Sciences, University of Bristol, Bristol, UK, [10]MARUM – Center for Marine Environmental Sciences, University of Bremen, Bremen, Germany, [11]School of Geographical Sciences, University of Bristol, Bristol, UK, [12]Department of Physics, Faculty of Science, Institute for Marine and Atmospheric Research, Utrecht University, Utrecht, The Netherlands, [13]Alfred Wegener Institute Helmholtz Centre for Polar and Marine Research, Bremerhaven, Germany, [14]Department of Geology and Environmental Geosciences, Lafayette College, Easton, PA, USA, [15]School of Earth and Environmental Sciences, Cardiff University, Cardiff, UK, [16]Department of Atmospheric Science, School of Environmental Studies, China University of Geoscience, Wuhan, China, [17]National Oceanography Centre, Southampton, UK, [18]Council on Science and Technology, Princeton University, Princeton, NJ, USA, [19]College of Earth, Ocean, and Atmospheric Sciences, Oregon State University, Corvallis, OR, USA, [20]NORCE Norwegian Research Centre, Bjerknes Centre for Climate Research, Bergen, Norway

Key Points:

- A synthesis of Miocene modeling efforts, and surface temperature reconstructions, is presented within a single analysis framework
- Miocene global mean surface temperature estimates span ~5.3°C–11.5°C higher than preindustrial, only ~2°C is explained by non–CO_2 boundary conditions in climate models
- Some simulations overlap with reconstructed global mean surface temperature estimates but fail to capture the weak temperature gradient

Supporting Information:

Supporting Information may be found in the online version of this article.

Correspondence to:

N. J. Burls,
nburls@gmu.edu

Citation:

Burls, N. J., Bradshaw, C. D., De Boer, A. M., Herold, N., Huber, M., et al. (2021). Simulating Miocene warmth: Insights from an opportunistic multi-model ensemble (MioMIP1). *Paleoceanography and Paleoclimatology*, *36*, e2020PA004054. https://doi.org/10.1029/2020PA004054

Received 20 JUN 2020
Accepted 24 MAR 2021

Abstract

The Miocene epoch, spanning 23.03–5.33 Ma, was a dynamic climate of sustained, polar amplified warmth. Miocene atmospheric CO_2 concentrations are typically reconstructed between 300 and 600 ppm and were potentially higher during the Miocene Climatic Optimum (16.75–14.5 Ma). With surface temperature reconstructions pointing to substantial midlatitude and polar warmth, it is unclear what processes maintained the much weaker-than-modern equator-to-pole temperature difference. Here, we synthesize several Miocene climate modeling efforts together with available terrestrial and ocean surface temperature reconstructions. We evaluate the range of model-data agreement, highlight robust mechanisms operating across Miocene modeling efforts and regions where differences across experiments result in a large spread in warming responses. Prescribed CO_2 is the primary factor controlling global warming across the ensemble. On average, elements other than CO_2, such as Miocene paleogeography and ice sheets, raise global mean temperature by ~2°C, with the spread in warming under a given CO_2 concentration (due to a combination of the spread in imposed boundary conditions and climate feedback strengths) equivalent to ~1.2 times a CO_2 doubling. This study uses an ensemble of opportunity: models, boundary conditions, and reference data sets represent the state-of-art for the Miocene, but are inhomogeneous and not ideal for a formal intermodel comparison effort. Acknowledging this caveat, this study is nevertheless the first Miocene multi-model, multi-proxy comparison attempted so far. This study serves to take stock of the current progress toward simulating Miocene warmth while isolating remaining challenges that may be well served by community-led efforts to coordinate modeling and data activities within a common analytical framework.

Plain Language Summary

As human activity continues to increase atmospheric carbon dioxide concentrations, scientists turn to warm intervals in Earth's history to develop insight into the behavior of the climate system under elevated carbon dioxide and temperature. One such interval is the Miocene epoch which has become increasingly relevant as reconstructions of Miocene atmospheric CO_2 concentrations point to values ranging between current concentrations of ~400 ppm and those projected for the end of this century under Shared Socioeconomic Pathways 3 and 4. In this study, we evaluate the

surface warming patterns simulated by a range of different climate models configured with Miocene paleogeography and CO_2 concentrations spanning 200–850 ppm. We also synthesize available Miocene surface temperature reconstructions. The primary factor controlling the amount of global warming seen across the Miocene simulations analyzed is the CO_2 concentration that was prescribed within a given simulation. On average, Miocene elements other than CO_2, such as Miocene paleogeography and ice sheets, raise global mean temperature by ~2°C. While some Miocene simulations with high CO_2 forcing overlap with the reconstructed global mean surface temperature estimates for their target Miocene interval, they still generally fail to capture the reconstructed pattern of warming.

1. Introduction

The Miocene epoch (23.03–5.33 Ma) encompasses much of the range of climate states between the Cenozoic endmembers of peak Eocene warmth and the modern ice-house state with extensive glaciation at both poles (Figure 1, Steinthorsdottir et al., 2020). Terrestrial and marine records show that Miocene climate

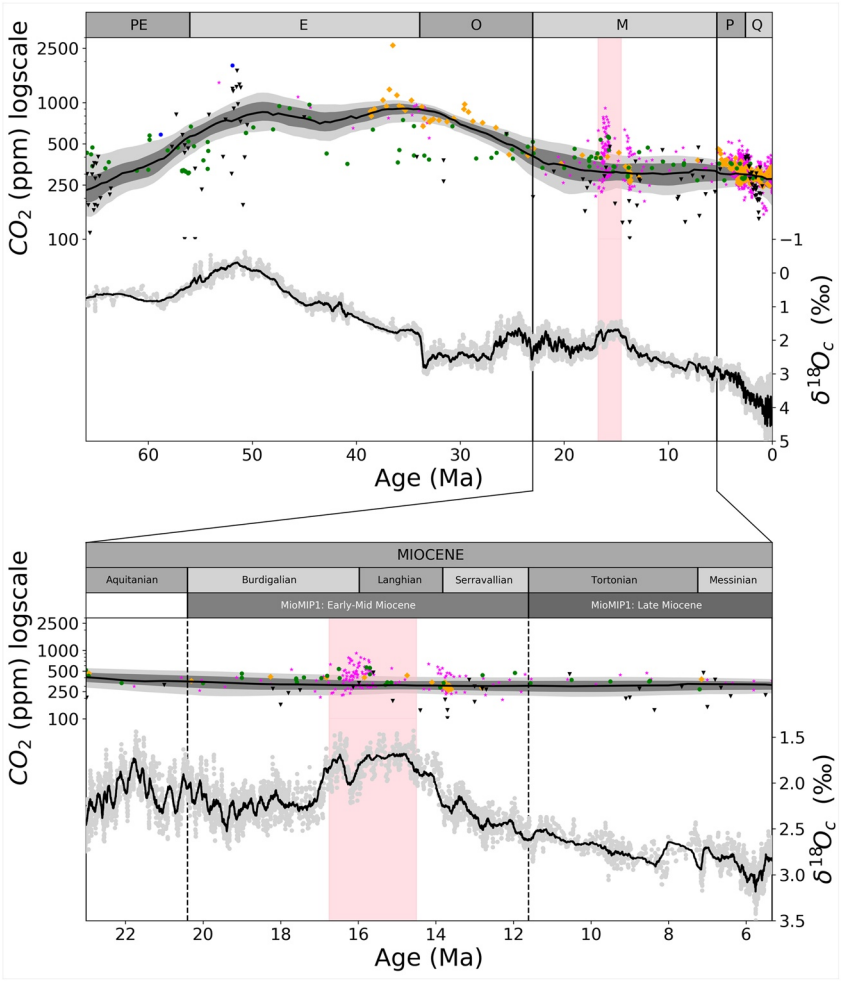

Figure 1. The Miocene within the Cenozoic. The Late Miocene (Tortonian and Messinian, 11.6–5.33 Ma) and Early Middle Miocene (Burdigalian, Langhian, and Serravallian, 20–11.6 Ma) are shown, as well as the MCO (16.75–14.5 Ma) shaded in pink. Multiproxy CO_2 reconstructions are from Foster et al. (2017) and Sosdian et al. (2018). CO_2 from leaf stomata is shown in green circles, pedogenic carbonate $\delta^{13}C$ as black triangles, boron isotopes in foraminifera as pink stars, liverwort $\delta^{13}C$ as blue octagons, and $\delta^{13}C$ of alkenones as orange diamonds. The most likely fit through the data is shown as the black line and 68% and 95% confidence intervals are shown as dark and light gray bands. Benthic oxygen isotopic composition ($\delta^{18}O_c$) taken from Zachos et al. (2001, 2008). The time period abbreviations shown in the top bar are as follows: E, Eocene; M, Miocene, O, Oligocene; PE, Paleocene; P, Pliocene; Q, Quaternary.

was significantly warmer than today and highly dynamic. Oxygen isotope records of benthic foraminifera ($\delta^{18}O_c$) show that peak Miocene warmth and minimum ice volume occurred in the Early to Middle Miocene (16.75–14.5 Ma), known as the Miocene Climate Optimum (MCO) (Figure 1). During the MCO, current reconstructions suggest that sea surface temperatures (SSTs) were 8°C–10°C warmer than present in the high southern latitudes (Shevenell et al., 2004) and 10°C–15°C warmer in the high northern latitudes (Super et al., 2020), while deep ocean temperatures were ~5°C–8°C warmer (Lear et al., 2000, 2015), leading to an estimated global mean surface temperature anomaly of 7.6°C ± 2.3°C compared to preindustrial (Goldner et al., 2014). The warmer conditions shifted the bioclimatic zones poleward (Pound et al., 2012). While the extent of the Greenland glaciation remains unclear (Thiede et al., 2011), it contributed negligibly to global ice volume and there is evidence to suggest that even during the late Miocene the Arctic experienced sea ice-free summers (Stein et al., 2016). Regions of Antarctica supported woody temperate vegetation that graded into tundra further inland with a much-reduced ice sheet extent (Pound et al., 2012; Sangiorgi et al., 2018; Warny et al., 2009). Although cooler than the peak warmth of the MCO, in the late Miocene (11.6–5.33 Ma), SSTs still ranged between 10°C and 15°C warmer than modern in the high latitudes, and 2°C–4°C warmer in the Tropics (Herbert et al., 2016; LaRiviere et al., 2012), while temperatures in the deep ocean are estimated to have been ~4°C warmer than present (LaRiviere et al., 2012). Geochemical and ice-rafted debris records indicate an increasing prevalence of colder temperatures as cooling progressed into the late Miocene (Stein et al., 2016; Winkler et al., 2002). The wide dynamic range of Miocene climate implies either strong sensitivity to forcing or strong and highly variable forcings through the Miocene.

The driving forces behind Miocene warmth and its fluctuations remain enigmatic, and several aspects have been difficult to reconcile with CO_2 reconstructions that are generally similar to modern or end-of-century projections (Figure 1). Typical proxy estimates for the Miocene are in the 300–600 ppmv range (Figure 1, Foster et al., 2012, 2017; Sosdian et al., 2018), although during the MCO, recent reconstructions suggest that CO_2 may have been as high as 800–1,100 ppm (Sosdian et al., 2018; Stoll et al., 2019). A full description of the Miocene CO_2 reconstructions and their uncertainties is given in Section 8 of (Steinthorsdottir et al., 2020). A prolonged carbon isotope excursion between ~16.7 Ma and ~13.5 Ma (the Monterey Excursion; Vincent & Berger, 1985) documents a marked perturbation of the carbon cycle at this time, modulated by orbital forcing. It is suggested that this excursion is due to enhanced organic matter burial on submerged continental shelves and higher CO_2 concentrations resulting in higher biological carbon isotope fractionation (Sosdian et al., 2020). A long-term decrease in the global carbon isotopic composition record for the late Miocene coincides with the long-term decrease in global temperatures, suggesting that carbon cycle changes were the driver for late Miocene global cooling. With CO_2 concentrations in the 300–600 ppmv range, it has not been possible to simulate the observed polar amplified warmth of the Miocene, as well as the lack of summer sea-ice more typical of mid-to-late Miocene conditions (Stein et al., 2016).

Numerous studies have therefore explored the role of other potential mechanisms. Although geologically recent, paleogeographic differences between the Miocene and today are substantial. There were major differences in ocean gateway configurations, such as connections between the Pacific and Atlantic Oceans, the Atlantic and Indian Oceans, and the Indian and Pacific Oceans, which today are either restricted or closed completely (Figure 2). Mountain building was occurring in all of the world's major mountain chains in the Miocene (see He et al., this issue), which transformed local hydrological regimes. Changes in the land surface itself may also be important for driving global warmth. Smaller ice sheets at both poles likely contributed to the polar amplified warmth and the weaker latitudinal temperature gradient of the time. Vegetation distributions resulting from a warmer global climate may itself provide a stabilizing feedback mechanism to maintain that warmth (e.g., Bradshaw et al., 2015; Knorr et al., 2011). As described in more depth in the following section, while these mechanisms have been shown to contribute to warming in models, they fall short of explaining the full extent, and the polar amplified spatial structure, of Miocene warmth (also see summary in Steinthorsdottir et al., 2020).

In this study, we synthesize available Miocene modeling efforts, together with available terrestrial and ocean surface temperature reconstructions, within a single analysis framework. We evaluate the current range of model-data agreement, highlight robust mechanisms operating across Miocene modeling efforts, as well as the regions where the differences across models (coming from a combination of model differences in imposed non–CO_2 Miocene boundary conditions and model feedbacks) result in a large spread in warming re-

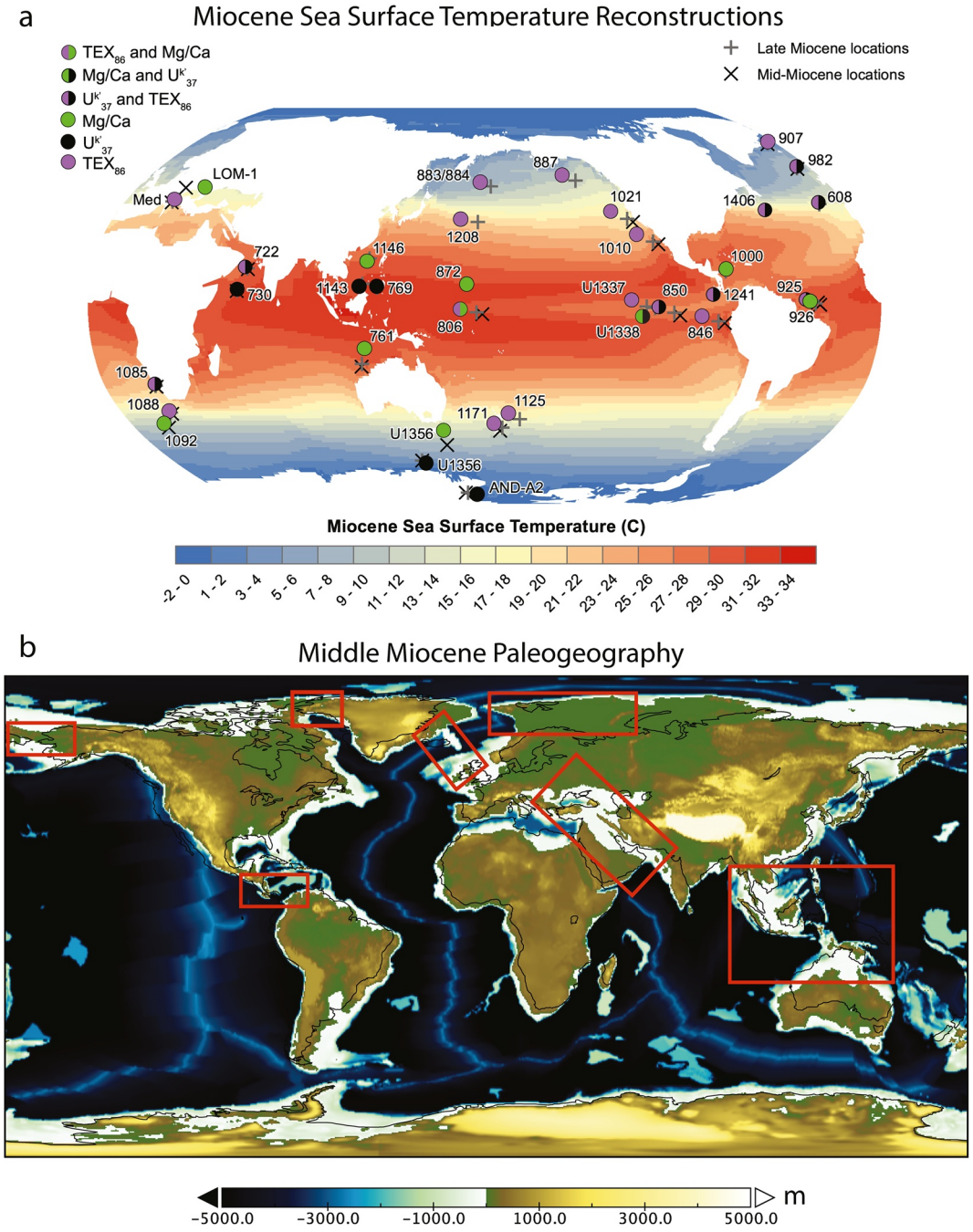

Figure 2. (a) The Middle and Late Miocene sea surface temperature reconstructions synthesized and used within our model-data comparison. The cross (plus) symbols indicate the average Middle (Late) Miocene site location, while filled circles indicate the modern site location. The color-coding of each circle indicates the type of proxy record available for each site. The contoured sea surface temperature field shown is derived from the multimodel mean of all of the simulations listed in Table 2 with Early Middle Miocene boundary conditions. (b) The Middle Miocene paleogeography is described and made available in this study (updated Herold, Huber, and Müller [2011], see supporting information). The red boxes highlight prominent paleogeographic features that evolved over the Miocene and into the Pliocene, namely: the Panama Gateway, Bering Strait, Barents Sea Landmass, Indonesian Seaway, Tethys Seaway, Greenland-Scotland Ridge, and the Canadian Archipelago. See Table 4 which describes the key characteristics associated with the various baseline paleogeographic forcings used across the MioMIP simulations.

sponses. In Section 2, we provide some background on Miocene modeling and the motivation for this study. In Section 3, we detail the Miocene modeling efforts analyzed, as well as the Miocene surface temperature records that we have synthesized to facilitate a model-data comparison and Miocene global mean surface temperature estimates. The intermodel analysis is presented in Section 4, where we discuss global mean warmth, simulated warming patterns and present the model-data comparison. We conclude with Section 5.

2. Background

Climate model simulations pertaining to the Miocene date to the early days of climate modeling itself. Experiments to assess the role of uplift of the Himalayas and the Tibetan Plateau and of the American Rockies found that lower orography resulted in marked changes in precipitation patterns and warmer winter temperatures, but that the magnitude of the temperature change simulated was insufficient to rule out the need for other climate forcings (Kutzbach et al., 1993; Ruddiman & Kutzbach, 1989). These early simulations used atmosphere-only models, however, and more recent coupled atmosphere-ocean models show that uplift of the Tibetan Plateau also impacts ocean circulation resulting in far-field warming (Su et al., 2018).

Several modeling studies have investigated the role of changes in ocean gateways. Miocene Ocean General Circulation Models (OGCMs) simulating an open Isthmus of Panama tend to have a net volume transport that is eastward from the Pacific to the Atlantic Ocean (Maier-Reimer et al., 1990; Mikolajewicz et al., 1993; X. Zhang et al., 2012). Water from the Pacific Ocean is fresher than that in the Atlantic Ocean, causing these modeling studies with an open Isthmus of Panama to simulate a freshening of the North Atlantic, a resulting weakening of North Atlantic Deep Water (NADW) formation and strength of the Atlantic Meridional Overturning Circulation (AMOC). This reorganization of ocean circulation results in cooling of the Northern Hemisphere and warming of the Southern Hemisphere, but the global mean annual temperature changes are small (∼+0.25°C or less, Lunt et al., 2008). With a wide-open Panama Gateway, there no longer needs to be a strong relationship between NADW formation and the AMOC, the North Atlantic can import water through the open Isthmus and through Tethys in the surface branch and export in through the Panama Gateway in the deep branch. Although the Isthmus would have been closing throughout the Miocene, most proxy records show that NADW did not strengthen significantly until after the Miocene (Bartoli et al., 2005; Burton et al., 1997; Haug & Tiedemann, 1998; Lear et al., 2003; Ling, 1997; O'Dea et al., 2016). That said, NADW probably initiated and fluctuated in strength since the late Eocene (Coxall et al., 2018). Therefore, although the timing of emergence of the Isthmus is still hotly debated (e.g., Montes et al., 2012), tectonic changes in this region are not thought to be the cause of Miocene warmth. Together with the Isthmus of Panama, the depth and width of other ocean gateways may have also played a role in the Miocene temperature distribution. It has been suggested that the closure of the Tethys tropical connection between Indian and Atlantic Oceans, together with a deepening or widening of the Drake Passage, induced a reversal of the net ocean flow through the Isthmus (Omta & Dijkstra, 2003; von der Heydt & Dijkstra, 2006) approximately in the Early Miocene. Before the Tethys closure, net transport through the Isthmus was toward the Pacific, while after closure, it was directed toward the Atlantic as several other Miocene GCMs have shown. Nevertheless, independent of the net flow direction in the Isthmus, GCM simulations show export of Northern Component Water formed in the Atlantic (though much weaker than present) toward the Pacific (von der Heydt & Dijkstra, 2006), keeping intermediate-to-deep waters relatively warm compared to the present day (Sijp et al., 2014); the latter holds in particular for the closed-Tethys situation, which is representative of most of the middle-to-late Miocene.

Modeling studies that have taken all of the reconstructed paleogeographic, ice sheet, and vegetation differences into account simultaneously show that these changes alone (discounting any CO_2 differences or orbital variability) make the Miocene world globally warmer than today. For preindustrial CO_2 concentrations, the models estimate that annual mean temperatures are warmer than preindustrial conditions by 0.3°C–3°C (Bradshaw et al., 2012; Herold, Huber, Greenwood, et al., 2011; Herold, Huber, & Müller, 2011; Knorr et al., 2011) for the late Miocene and 3.1°C for the middle Miocene (Stärz et al., 2017) due to these nongreenhouse gas forcings. For middle Miocene boundary conditions, even with a slightly lower CO_2 concentration than preindustrial (at 200 ppm), a global annual mean temperature of 1.7°C warmer than modern has been simulated (Frigola et al., 2018). The anomaly between the Miocene temperatures and modern temperatures scales nonlinearly with the CO_2 concentration however, because of higher Miocene climate

sensitivity at higher CO_2 concentrations (Bradshaw et al., 2015; Knorr & Lohmann, 2014). Miocene model experiments also show that the combined Miocene boundary conditions make the world wetter than today (Bradshaw et al., 2012, 2015; Frigola et al., 2018; Herold, Huber, Greenwood, et al., 2011; Herold, Huber, & Müller, 2011; Knorr et al., 2011; Stärz et al., 2017).

The inability of Miocene simulations to capture the full extent of the polar amplified warmth and meridional temperature gradient reduction reflected in reconstructions is a problem that is not unique to the Miocene. Historically, it has been equally challenging to fully simulate the high-latitude warmth of the Eocene (Huber & Caballero, 2011; Huber & Sloan, 2001). That said, the latest DeepMIP effort which targets the Eocene has seen some improvement in the ability of models to simulate high-latitude warmth—three of the DeepMIP models (NorESM, GFDL, and CESM1.2) show improved skill in capturing elements of the polar amplification (Lunt et al., 2020) as reconstructed by a comprehensive synthesis of all the available Eocene data (Hollis et al., 2019). In the DeepMIP ensemble, the non–CO_2 component of warming from preindustrial to Eocene boundary conditions ranges from 3°C to 5°C (Lunt et al., 2020). This indicates that a significant contribution to warming comes from paleogeographic forcing, including vegetation changes, and ice-albedo effects. The improved model-data agreement seen in these Eocene simulations is likely also related to the better representation of cloud microphysics overall (Kiehl & Shields, 2001; Sagoo et al., 2013; Zhu et al., 2019). Interestingly, two of the DeepMIP models that best represented the proxy data were also models that implemented adapted aerosol concentrations, either coupling aerosols to a new cloud microphysics scheme (CESM; Zhu et al., 2019) or including aerosol forcing as a new fixed boundary condition (GFDL; Hutchinson et al., 2018; Lunt et al., 2020). These aerosol changes influence cloud microphysics and hence the radiative properties of these simulations and represent a major advance in their physical realism, but one that is largely unconstrained by geological data (Huber, 2013).

If the Eocene is the warmer endmember for the Miocene, the Late Pliocene which has been a target of the Pliocene Model Intercomparison Project represents the cooler endmember. This model intercomparison project is now in its second phase (PlioMIP2, Haywood et al. 2016), with a more tightly constrained time slice defined compared to the first phase aimed at reducing uncertainty in the proxy data. Because the Late Pliocene paleogeography is much more similar to the modern day, the non–CO_2 component of warming is much smaller than for the Eocene. Global annual mean surface air warming for the multi-model ensemble of PlioMIP2 is 3.2°C (with a range between 1.7°C and 5.2°C) relative to pre-industrial. All of these simulations use an atmospheric CO_2 concentration of 400 ppm. The multi-model-mean warming for PlioMIP2 is larger than seen in PlioMIP1 and is the result of contributions from recent models with modified aerosol and cloud microphysics, that have a relatively high climate sensitivity (Haywood et al., 2020). PlioMIP2 models exhibit polar amplification that is in better agreement with proxies than in PlioMIP1 models (Haywood et al., 2011, 2013), at mid and high latitudes, in part due to re-assessment of high latitude proxy records (McClymont et al., 2020), and in part due to changes in the configuration of the Bering Straits (Haywood et al., 2020, Otto-Bliesner et al., 2017) in the model simulations. Pliocene model-data comparisons can also provide constraints on climate sensitivity (Hargreaves & Annan, 2016; Haywood et al., 2020; Renoult et al., 2020), the relationship between climate sensitivity and Earth system sensitivity (Haywood et al., 2020; Lunt et al., 2010), and the contribution to warming from non–CO_2 forcings (Chandan & Peltier, 2018; Lunt, Dunkley Jones, et al., 2012; Lunt, Haywood, et al., 2012). Overall, the Pliocene represents a world that is in equilibrium with near-modern CO_2 forcing, and exhibits a climate similar to that expected at the end of this century under relatively optimistic emissions scenarios (Burke et al., 2018).

Although the Miocene represents a climate state in-between that of the early Eocene and the mid-Pliocene, and presents unique modeling challenges, no formal MIP exists for the Miocene. The existing Miocene model-data comparison efforts have used different proxy data sets and validation techniques (Bradshaw et al., 2012; Goldner et al., 2014; Herold, Huber, Greenwood, et al., 2011; Herold, Huber, & Müller, 2011; Krapp & Jungclaus, 2011; Micheels et al., 2011), and are restricted to interpreting results in a single model framework. Here, we seek to take advantage of the fact that several Miocene modeling efforts have been conducted and evaluate them within a single, consistent, model-data comparison framework to establish not only the degree of model-data agreement in simulating Miocene warmth but also the spread in model responses.

As a community, we have endeavored to take the first step toward the ideal solution of having a model-model and model-data intercomparison effort with uniform boundary conditions and standardized reference proxy data sets. Taking a similar approach as in the early steps of the DeepMIP process (Lunt, Dunkley Jones, et al., 2012; Lunt, Haywood, et al., 2012), we have surveyed the existing modeling experiments and sorted them into two groups based on the Miocene time period they have targeted: (1) Late Miocene experiments with a paleogeography that falls within 11.6–5.33 Ma (Tortonian and Messinian) and (2) Middle to Early Miocene experiments with paleogeography that falls within 20–11.6 Ma (Burdigalian, Langhian, and Serravallian). Unlike a formal model intercomparison where the same boundary conditions are used in each model, it is difficult to isolate the model dependence of the climate response to specific forcing (e.g., CO_2 vs. paleogeography). Nevertheless, the informal model intercomparison presented in this paper serves to provide a "multi-model-ensemble of opportunity" view of the spread in model responses to a range of Miocene boundary conditions and CO_2 forcings, within a single model-data comparison framework; an approach that has previously been used in deep-time paleoclimate modeling (Lunt, Dunkley Jones, et al., 2012; Lunt, Haywood, et al., 2012). The results presented in this study serve to synthesize the current range of model-data agreement seen across Miocene modeling efforts to date, highlight robust mechanisms operating across Miocene modeling efforts, and take stock of the current progress toward simulating Miocene warmth while isolating remaining challenges. Our eventual aim is to catalyze a formalized and community-based MioMIP project.

3. Methods

3.1. Available Modeling Efforts

Several studies targeting the Miocene have been performed by modeling groups across the globe. In this section, we provide a brief overview of the simulations performed by these studies as summarized in Tables 1–3. Table 1 summarizes the modeling studies targeting the Late Miocene 11.6–5.33 Ma (Messinian and Tortonian), Table 2 summarizes the modeling studies targeting Middle/Early Miocene 11.6–20 Ma (Burdigalian, Langhian, and Serravallian). There are 10 Late Miocene and 31 Middle/Early Miocene experiments with a total of 41 experiments analyzed. Table 3 lists two additional sets of Miocene simulations from studies in which sensitivity to orbital changes was assessed. A summary of the key characteristics associated with the various baseline paleogeographic forcing used is provided in Table 4. All of the fully coupled model simulations have been run for at least 1,100 years and so the atmosphere and surface ocean have reached a state of near equilibrium.

CCSM3-NH: A series of simulations have been published using the National Center for Atmospheric Research (NCAR) Community Climate System Model (CCSM3) to simulate Middle to Early Miocene climate utilizing the boundary conditions of Herold et al. (2008), that is, Herold et al. (2010) and You et al. (2009), or the updated boundary conditions of Herold, Huber, and Müller (2011), that is, Herold, Huber, Greenwood, et al. (2011) and Herold et al. (2012). The details of these CCSM3 simulations are summarized in Tables 1 and 2. Table 4 summarizes the key features associated with the Herold, Huber, and Müller (2011) paleogeography boundary conditions which have been widely used by other groups and have formed the basis for some other Miocene boundary condition efforts. For the sake of this intercomparison study, output from the last 100 years of the CCSM3-NH simulation (Herold, Huber, Greenwood, et al., 2011; Herold et al., 2012; Table 2) run for 1,100 years have been provided, at which point global mean ocean temperature varied by less than 0.01° per century.

CCSM3 T42 (MARUM): CCSM3 T42 (MARUM) simulations have been performed for the periods just before (Middle Miocene Climate Optimum; MMCO) and after (Middle Miocene Glaciation; MMG) the Middle Miocene Climate Transition around 13–15 Ma (Table 2). These two experiments differ in the atmospheric CO_2 concentration (400 ppmv in MMCO and 200 ppmv in MMG) and the volume of the Antarctic ice sheet (43-m difference in sea-level equivalent). In addition, two sensitivity experiments with respect to atmospheric CO_2 have been carried out: experiment MMCO_200 uses the MMCO Antarctic ice sheet but an atmospheric CO_2 level of 200 ppmv, while MMG_400 uses the larger MMG ice sheet but an atmospheric CO_2 level of 400 ppm. All other greenhouse gases, as well as ozone distribution, aerosols, solar constant, and orbital configuration, were set to pre-industrial levels. All Miocene experiments use Middle Miocene

Paleoceanography and Paleoclimatology

10.1029/2020PA004054

Table 1
Late Miocene Experiments With Paleogeography That Falls Within 11.6–5.33 Ma (Tortonian & Messinian)

Modeling effort	Target time period	Resolution Atm/Ocn	Length (years analyzed)	CO_2 levels	Veg	Methane levels	Aerosols	Orbit	Greenland ice sheet	Antarctic ice sheet	Paleo-geographic forcing used	Exp. names (original study)	Exp. names (this study)	References
COSMOS T31	Tortonian (11–7 Ma)	3.75° × 3.75° /~3°	2,000 (last 100)	278 450	Prescribed Micheels et al. (2007, 2011)	PI (650)	PI	modern	No	Modern Antarctic IS height	Tortonian (11–7 Ma) Micheels et al. (2011) with minor modifications cf. Knorr et al. (2011)	MIO ICE_FULL_ CO2_450	"COSMOS Late Miocene 278/450 ppm"	Knorr et al. (2011) and Knorr and Lohmann (2014)
				278 450					No	25% modern Antarctic IS height		ICE_ Quarter_ CO2_278 ICE_ Quarter_ CO2_450	"COSMOS Late Miocene ICEQ 278/450 ppm"	Knorr and Lohmann (2014)
HadCM3L – Bradshaw	Late Miocene	3.75° × 2.5° /3.75° × 2.5°	2,100 (last 50)	280 400	Dynamic	PI (760)	PI	Modern	Yes	Yes	Markwick (2007)	Tczth tczti	"HadCM3L Late Miocene 280/400 ppm"	Bradshaw et al. (2012)
HadCM3L – Farnsworth	Tortonian	3.75° × 2.5°/ 3.75° × 2.5°	7,422 (last 100)	400	Dynamic	PI (760)	PI	Modern	Yes	Yes	Getech Plc.	teupn	"HadCM3L Tortonian 400 ppm"	Farnsworth, Lunt, O'Brien, et al. (2019)
	Messinian											teupo	"HadCM3L Messinian 400 ppm"	
NorESM-L	10 Ma	T31–3.75° /~3°	>2,000 (last 200)	420 560	Idealized	PI	PI	Modern	No	No	Zhang et al. (2014)	LM 420 LM 560	"NorESM-L 10 Ma 350/560 ppm"	Zhang et al. (2014)

Paleoceanography and Paleoclimatology

10.1029/2020PA004054

Table 2
Middle and Early Miocene Experiments With Paleogeography That Falls Within 20–11.6 Ma (Burdigalian, Langhian & Serravallian)

Modeling effort	Target time period	Resolution Atm/Ocn	Length (years analyzed)	CO_2 levels ppmv	Veg	Methane levels ppb	Aerosols	Orbit	Greenland ice sheet	Antarctic ice sheet	Paleo-geographic forcing used	Exp. name (original study)	Exp. name (this study)	References
CCSM-NH3	~20–14 Ma	T31–3.75° /~3 × 1.5°	1,100 (last 100)	355 560	Fixed – early Miocene	PI (760)	PI	modern	Herold et al. (2008)	Herold et al. (2008)	Herold, Huber, and Müller (2011)	m0015 m0025	"CCSM-NH3 355 ppm" "CCSM-NH3 560 ppm"	Herold, Huber, and Müller (2011), Herold, Huber, Greenwood, et al. (2011), and Herold et al. (2012)
CCSM3 T42 (MARUM)	MMCO	T42–2.8°/1°	1,500 (last 100)	400 200	Frigola et al. (2018) based on Pound et al. (2012), Wolfe (1985), and Morley (2011)	PI (760)	PI	modern	No	6.e6 km3	Frigola et al. (2018) based on Herold, Huber, and Müller (2011), Hall (2012), and Montes et al. (2012)	MMCO MMCO_200	"CCSM3 T42 MMCO 400 ppm" "CCSM3 T42 MMCO 200 ppm"	Frigola et al. (2018)
	MMG			200 400						23.e6 km3		MMG MMG_400	"CCSM3 T42 MMG 200 ppm" "CCSM3 T42 MMG 400 ppm"	Frigola et al. (2018)
CCSM4	~20–14 Ma	~1.9° × 2.5° /1°	2,000 (last 100)	400	Fixed – early Miocene	PI (791)	PI	Modern	0.29e6 km^3	6.5e6 km^3	As described in in this article (updated Herold, Huber, and Müller [2011])	B.MIO_400_C4	"CCSM4 400 ppm"	
CESM1 (CAM5)	~20–14 Ma	~1.9° × 2.5° /1°	3,000 (last 50)	400	Fixed early Miocene	PI (791)	PI (aerosol flux close to PI)	Modern	0.29e6 km^3	6.5e6 km^3	As described in in this article (updated Herold, Huber, and Müller [2011])	B.MIO_400_C5	"CESM1 400 ppm"	

Paleoceanography and Paleoclimatology

10.1029/2020PA004054

Table 2
Continued

Modeling effort	Target time period	Resolution Atm/Ocn	Length (years analyzed)	CO_2 levels ppmv	Veg	Methane levels ppb	Aerosols	Orbit	Greenland ice sheet	Antarctic ice sheet	Paleo-geographic forcing used	Exp. name (original study)	Exp. name (this study)	References
COSMOS T31	Middle Miocene (Herold ~20–14)	3.75° × 3.75° /~3°	2,000 (last 100)	278 450	Dynamic	PI (650)	PI	Modern	No	Herold et al. (2008)	Middle Miocene (Herold, Huber, & Müller (2011))+ regional bathymetry reconstruction (15 Ma) North Atlantic/Arctic (Ehlers & Jokat, 2013)	EO_278 EO_450	"COSMOS Mid Miocene 278 ppm" "COSMOS Mid Miocene 450 ppm"	Stärz et al. (2017)
HadCM3L - Bradshaw	Mid Miocene	3.75° × 2.5° /3.75° × 2.5°	2,000 (last 50)	850 560 400 280	Dynamic	760 (PI)	PI	Modern	No	90mSLE	Markwick (2007)	Teudt Teudl eudi teude	"HadCM3L Mid Miocene 90SLE 850/560 /400/280 ppm"	Bradshaw et al. (2021)
				850 560 400 280						55mSLE		teuds teudk teudc teudz	"HadCM3L Mid Miocene 55SLE 850/560 /400/280 ppm"	
				850 560 400 280						No		teudu teudq teudp teudo	"HadCM3L Mid Miocene NOSLE 850/560 /400/280 ppm"	
HadCM3L –Farnsworth	Langhian	3.75° × 2.5°/ 3.75° × 2.5°	7,422 (last 100)	280 400 560	Dynamic	760 (PI)	PI	Modern	No	Yes	Getech Plc.	teupl teupla	"HadCM3L Langhian 280/400/560 ppm"	Farnsworth, Lunt, O'Brien, et al. (2019)
IPSLCM5A2	20 Ma	3.75° × 1.875° /~2 × 0.5°	3,000 (last 100)	840 560 420 560	Idealized	291 (PI)	PI	Modern	Yes No	Yes	ERC MAGIC	C20M-ICE-GA-840 C20M-ICE-GA C20M-ICE-GA-420 C20M-ICE-NoGIS	"IPSLCM 20 Ma 840/560/420 ppm" "IPSLCM 20 Ma NoGIS 560 ppm"	
NorESM-L	20 Ma	T31–3.75°/~3°	>2,000 (last 200)	350 560	Idealized	PI	PI	Modern	No	No	Zhang et al. (2014)	EM 350 EM 560	"NorESM-L 20 Ma350 /560 ppm"	Zhang et al. (2014)

global topography, bathymetry, and vegetation as described in Frigola et al. (2018). The experiments were integrated for a total of 1,500 years each, where the last 100 years were used for analyses.

CCSM4: Following on from Goldner et al. (2014) which used a "slab ocean", fully coupled simulations have been conducted using version 1.0.5 of the Community Earth System Model with version 4 of the Community Atmosphere Model (the equivalent of CCSM4; Gent et al., 2011). The CESM1.0 model improvements, in comparison to older generation models, are described in previous study focused on both modern-day climate (Bitz et al., 2012; Neale et al., 2010) and paleoclimate (Goldner et al., 2014; Shields et al., 2012); >2,000 years were simulated. The simulations were initialized with initial conditions from the prior CCSM3-NH simulations so that they equilibrated quickly, and were run with Early to Middle Miocene boundary conditions updated from Herold et al. (2008), Herold, Huber, and Müller (2011), and Herold et al. (2012). These updates to the paleogeography were extensive (Figure 2b) and not previously described. We therefore provide a description of how these boundary conditions were constructed (supporting information S1) and make them available to the community (supporting information Data Set S1). These simulations used the bulk aerosol mode (BAM) with preindustrial aerosols prescribed.

CESM1-CAM5: The CESM1-CAM5 simulations are run using Miocene boundary conditions that are essentially identical to those used in the CCSM4 simulations. The updated paleogeography described above is used throughout. Orbital parameters and other boundary conditions follow the pre-industrial configuration.

The main difference between the CCSM4 and CESM1-CAM5 cases lies in the physics of the atmospheric component. CAM5 has many improvements over its predecessors in its handling of clouds and aerosols (Bacmeister et al., 2012; Gettleman et al., 2008, 2010, 2015; Neale et al., 2010), radiative transfer (Iacono et al., 2008), deep convection (Neale et al., 2010), and shallow convection and moist boundary layer processes (Bretherton & Park, 2009). The combination of these improvements in physical parameterization allows for the simulation of complete aerosol-cloud interactions of cloud droplet activation by aerosols, precipitation processes due to particle size-dependent behavior, and explicit radiative interaction of cloud particles. These simulations are run with the standard CAM5 3-mode modal aerosol mode (MAM3, X. Liu et al., 2012). The aerosol flux is tuned to be close to the preindustrial control flux (Dicks, 2019). Using MAM3 ensures self-consistent aerosol-cloud microphysical interaction.

As described in Zhou et al. (2018), these CESM1-CAM5 simulations were initialized from the end of the CCSM4 simulations (at 2,200 model years). The CCSM4 simulation was equilibrated with a surface radiative imbalance of 0.08 W m^{-2}. The CESM1-CAM5 simulation used here was continued for another 1,800 years at which point the global mean surface temperature was nearly unchanged and the long-term mean surface radiative imbalance was 0.07 W m^{-2}. These simulations were then extended, and the output was archived for this study.

COSMOS: COSMOS, with its ECHAM5 (Roeckner et al., 2003) atmospheric component and MPIOM (Marsland et al., 2003) oceanic component, has been used for simulating the Late Miocene in Knorr et al. (2011) and the Middle Miocene Climate transition in Knorr and Lohmann (2014). For further details regarding the paleogeography reconstruction and proxy-based reconstruction of the Late Miocene vegetation, refer to Micheels et al. (2007, 2011) and the references therein. The corresponding boundary conditions are available at PANGAEA (Knorr et al., 2019). Further details on ECHAM5/MPIOM are described in Jungclaus et al. (2006). Furthermore, Middle to Early Miocene simulations have been performed in a COSMOS model configuration (Huang et al., 2017; Stäerz et al., 2017) that additionally include dynamical vegetation as part of the land surface scheme JSBACH (Brovkin et al., 2009; Raddatz et al., 2007). The model setup targets the Middle to Early Miocene time period (~23–15 Ma) using the boundary conditions of Herold et al. (2008), including orography, paleobathymetry, and ice sheet adjustments. Additionally, a regional high-resolution bathymetric reconstruction comprising the North Atlantic/Arctic Ocean (Ehlers & Jokat, 2013) has been implemented.

Genesis-slab ocean: The Genesis simulations were performed to provide boundary meteorology to an Antarctic regional climate model; they have different Antarctic ice sheet extents and have extremes of astronomical parameters that lead to highs (ecc. = 0.05, obliquity = 24.5°, longitude of precession = 270°) and lows (ecc. = 0.05, obliquity = 22.5°, longitude of precession = 90°) of insolation for Antarctica. Simu-

Table 3
Orbital Parameter Sensitivity Experiments

Modeling effort	Target time period	Resolution Atm/Ocn	Length (years analyzed)	CO_2 levels (ppmv)	Veg	Aerosols
Genesis (slab ocean)	Middle Miocene (Herold ~20–14 Ma	T31/slab	50 (last 30)	280	Dynamic	PI
				840		
				2240		
				280		
				840		
				2,240		
				280		
				840		
				2,240		
HadCM3L – Marzocchi	Late Miocene (Messinian)	3.75° × 2.5°/3.75° × 2.5°	200 plus additional 2,100-year spin-up without orbital variability (last 50)	280	Dynamic	PI

lations were also performed with an astronomical configuration similar to the modern day (ecc. = 0, obliquity = 23.5°). The atmosphere is coupled to a 50-m slab diffusive mixed-layer ocean and dynamical sea-ice model (Thompson & Pollard, 1997). The runs include dynamic vegetation and oxygen isotope tracing. The paleogeography is from Herold et al. (2008) with modifications to Antarctica. Simulations were run for 50 years with 30 years used for analysis.

Orbit	Greenland ice sheet	Antarctic ice sheet	Paleo-geographic forcing used	Exp. names	Exp. names (this study)	References
3 different orbital configurations	No	Fully Glaciated	Herold et al. (2012)	1FUCObi	1FUCObi	Gasson et al. (2016)
				1FUMEbi	1FUMEbi	
				1FUWAbi	1FUWAbi	
				3FUCObi	3FUCObi	
				3FUMEbi	3FUMEbi	
				3FUWAbi	3FUWAbi	
				8FUCObi	8FUCObi	
				8FUMEbi	8FUMEbi	
				8FUWAbi	8FUWAbi	
		Partially glaciated		1MECObi	1MECObi	
				1MEMEbi	1MEMEbi	
				1MEWAbi	1MEWAbi	
				3MECObi	3MECObi	
				3MEMEbi	3MEMEbi	
				3MEWAbi	3MEWAbi	
				8MECObi	8MECObi	
				8MEMEbi	8MEMEbi	
				8MEWAbi	8MEWAbi	
		Unglaciated		1NOCObi	1NOCObi	
				1NOMEbi	1NOMEbi	
				1NOWAbi	1NOWAbi	
				3NOCObi	3NOCObi	
				3NOMEbi	3NOMEbi	
				3NOWAbi	3NOWAbi	
				8NOCObi	8NOCObi	
				8NOMEbi	8NOMEbi	
				8NOWAbi	8NOWAbi	
Modern	Reduced	Reduced	Markwick (2007)	Tdiub tdiud	"HadCM3L ModernOrbit" "HadCM3L 125kOrbit"	Marzocchi et al. (2015), Marzocchi et al. (2016), Simon et al. (2017), and Marzocchi et al. (2019)
125k orbit min seasonalityMax seasonality NH				tdiue		
Max seasonality SH				tdiuf tdiug	"HadCM3L min seasonality" "HadCM3L max seasonality NH" "max seasonality SH"	

HadCM3L-Bradshaw: These simulations use the HadCM3LB-M2.1aD and HadCM3LB-M2.1aE (Valdes et al., 2017) coupled atmosphere-ocean general circulation models with an interactive vegetation scheme. The late Miocene simulations (HadCM3LB-M2.1aD—vegetation model with a 10-day coupling period) were run for 2,100 years and the middle Miocene simulations (HadCM3LB-M2.1aE—vegetation model with a 5-year coupling period) continue on from the late Miocene simulations and have been run for a further 2,000 years. The last 50 years of the simulations are used for analyses. Both the late Miocene and the middle Miocene configurations use paleogeographies from Markwick (2007).

Table 4
Description of Key Characteristics Associated With the Various Baseline Paleogeographic Forcing Used

Baseline paleogeographic forcing used	Panama gateway	Bering strait	Barents sea landmass	Indonesian seaway	Tethys seaway	Greenland-Scotland ridge	Canadian archipelago
Middle and early Miocene							
Herold, Huber, and Müller (2011)	Open	Closed	Present	Open	Open	Deep	Closed
Described in this article (updated Herold, Huber, and Müller [2011], see supporting information)	Open	Closed	Present	Open	Open	Shallow	Closed
Frigola et al. (2018) which is based on Herold et al. (2012), Hall (2012), and Montes et al. (2012)	Open	Closed	Present	Open	Open	Deep	Closed
Middle Miocene (Herold) + regional bathymetry reconstruction (15 Ma) North Atlantic/Arctic (Ehlers & Jokat, 2013)	Open	Closed	Present	Open	Open	Deep	Closed
ERC MAGIC Poblete et al. (accepted)	Open	Closed	Present	Open	Closed	Deep	Closed
Z. Zhang et al. (2014); 20 Ma	Open	Closed	Present	Open	Open	Shallow (less than 450 m)	Closed
Getech Plc.	Open	Closed	Filled with land in region of LGM Fennoscandian ice sheet	Open	Closed	Shallow	Closed
Late Miocene							
Markwick (2007)	Open	Closed	Present	Open	Closed	Deep	Closed
Tortonian (11–7 Ma Micheels et al. (2011) with minor modifications cf. Knorr et al. (2011)	Open	Closed	Present	Open	Closed	Deep	Open
Getech Plc.	Open	Closed	Present	Open	Closed	Deep	Closed
Z. Zhang et al. (2014); 10 Ma	Open	Closed	Present	Open	Closed	Shallow (250–300 m)	Closed

HadCM3L-Marzocchi: These orbital parameter sensitivity simulations are initialized from the end of the 2,100-year late Miocene simulation by Bradshaw et al. (2012), so the model setup is identical to that described above as "HadCM3L-Bradshaw" for the late Miocene, apart from version HadCM3LB-M2.1aE (Valdes et al., 2017) was used. These simulations are all run for an additional 200 years with varying orbital parameters. Climatological means of the last 50 years of simulation are used for analyses.

HadCM3L-Farnsworth: These simulations use the HadCM3LB-M2.1aD (Valdes et al., 2017) coupled atmosphere-ocean general circulation model with a dynamic vegetation scheme as used for the late Miocene HadCM3L-Bradshaw simulations. The Getech Plc. paleogeographic (topography, bathymetry, and ice sheets) boundary conditions are the same as Farnsworth, Lunt, Robinson, et al. (2019) with stage specific solar luminosity for the Langhian, Tortonian, and Messinian (see Tables 1 and 2) as calculated by Gough et al. (1981). pCO_2 is set to 400 ppm (as well as two sensitivity studies at 280 and 560 ppm) in line with proxy estimates (Foster et al., 2017). Each simulation is integrated for 7,422 model years and has reached equilibrium in both the atmosphere and deep ocean with climate means taken from the last 100 years of each run. Each simulation was initialized from a stationary state in the ocean with the atmosphere initialized from a preindustrial state (for full details see Lunt et al. [2017] and Farnsworth, Lunt, O'Brien, et al. [2019]).

IPSLCM5A2: These simulations use the IPSL-CM5A2 Earth System Model (Sepulchre et al., 2020), which is built upon IPSL-CM5A-LR; the Coupled Model Intercomparision Project Phase 5 (CMIP5) Earth System Model developed at IPSL (Institut Pierre-Simon Laplace; Dufresne et al., 2013). As IPSL-CM5A-LR, it is composed of the LMDZ atmospheric model (Hourdin et al., 2013), the ORCHIDEE land surface and vegetation model (Krinner et al., 2005), and the NEMO ocean model (NEMO v3.6, Madec, 2008), which include modules for ocean dynamics (OPA8.2), biochemistry (PISCES, Aumont et al., 2015) and sea-ice (LIM2).

Atmospheric and oceanic grids are connected via a coupler (OASIS, Valcke, 2006). The ocean domain is an irregular tri-polar grid (ORCA2, Dufresne et al., 2013; Madec & Imbard, 1996). For more detailed descriptions of the model and its different components, the reader is referred to Sepulchre et al. (2020).

NorESM-L: These simulations use NorESM-L which couples the spectral Community Atmosphere Model (CAM4) (Eaton, 2010; Neale et al., 2013) and the Miami Isopycnic Coordinate Ocean Model (MICOM). NorESM-L performs well in simulating the pre-industrial climate (Z. S. Zhang et al., 2012) and has good skill in simulating paleoclimates (Z. Zhang et al., 2013; Z. Zhang et al., 2014). Detailed introduction of NorESM-L can be found in Z. S. Zhang et al., 2012; Bentsen et al., 2013, and the Miocene boundary conditions can be found in Z. Zhang et al. (2014).

3.2. Available Temperature Reconstructions

Here, we describe the proxy data sources used in the model-data comparison shown.

3.2.1. Late and Middle Miocene Terrestrial Mean Annual Temperature Estimates

The Bradshaw et al. (2012) synthesis has been used, as is, to provide Late Miocene terrestrial Mean Annual Temperature (MAT) estimates. A new synthesis of global terrestrial MATs has been generated for the Middle Miocene through the updating and expansion of the Pound et al. (2012) and Goldner et al. (2014) syntheses. Most estimates are from fossil plant data and use either the Co-existence Approach, CLAMP, or Leaf Margin Analysis. The Co-existence Approach uses the modern climatic range of a fossil taxons nearest living relative to determine the climatic envelope of co-existence for a fossil assemblage (Mosbrugger & Utescher, 1997; Utescher et al., 2014). CLAMP and Leaf Margin Analysis use the morphological characteristics of fossil leaves to determine climatic parameters (Uhl et al., 2003; Wolfe, 1971; Yang et al., 2011). The new synthesis expands the original data sets of 52–110 sites with important additional localities in the southern hemisphere (Table S1). Additional data points have been synthesized from the published literature with a cutoff date of October 2019. To maximize geographic spread, some sites with published taxa lists and no climate reconstructions have had MAT estimates reconstructed. New MAT reconstructions are based upon the Co-existence Approach, following the advice of Utescher et al. (2014) and the updated data set of Pound and Salzmann (2017). All error margins and uncertainty ranges follow the published authors, unless none were provided in which case a 5°C uncertainty range was applied. A subset of the records within this new Middle Miocene MAT data set, with ages that fall between 14.5 and 16.75 Ma, are used to estimate MCO global mean surface temperature as outlined in Section 3.4.

3.2.2. Late, Middle Miocene and MCO Sea Surface Temperature Estimates

Published Miocene SST reconstructions (Mg/Ca, $U^{k}_{37,}$ and TEX_{86}) have been synthesized from the literature to provide Late and Middle Miocene mean annual SST estimates (Figure 2 and Table S2). The Herbert et al. (2016) U^{k}_{37} synthesis was used as a starting point. Both the previously published and new records within this data set were recalibrated/calibrated by Herbert et al. (2016) using the Müller et al. (1998) calibration. Any additional Miocene SST reconstructions not included in Herbert et al. (2016) were then added, without any recalibration or age model adjustments (i.e., the original calibrations and age models were used). A community effort to place all available records within a common calibration and age model framework, similar to the recent Eocene effort of Hollis et al. (2019), is planned, for which the summary provided in Table S2 can serve as a starting point together with new records published as part of this special issue.

The majority of the Miocene SST records are U^{k}_{37} records to which we assign a 95% confidence interval uncertainty of ±3°C (K. T. Lawrence et al., 2007). This value is aligned with one standard deviation uncertainty estimates of ±1.1°C (Conte et al., 2006) to ±1.5°C (Tierney et al., 2018). Care needs to be taken in tropical applications of the U^{k}_{37} ratio especially during past warm intervals because the ratio reaches saturation and thus the thermal limit of the paleothermometer at temperatures below the maximum surface water temperatures in the modern tropical ocean (Tierney et al., 2018). The remainder are Mg/Ca or TEX_{86} records. Care needs to be taken when interpreting TEX_{86} records as they have been shown to be influenced by temperature signals below the surface mixed layer (Lopes dos Santos et al., 2010). For the TEX_{86} uncertainty estimates, we use the stated 90% or 95% confidence intervals published with a given record or convert the stated one standard deviation uncertainty estimate to a 95% confidence interval. Care also needs to be taken when

using Miocene age Mg/Ca records given uncertainties in the Mg/Ca of seawater, salinity, and pH (Gray & Evans, 2019; Holland et al., 2020). Therefore, whilst most modern Mg/Ca-temperature calibrations have a standard deviation on the order of ±1.2°C (Anand et al., 2003), here we assign a 95% confidence interval uncertainty of ±4°C on absolute Mg/Ca SSTs. This Mg/Ca uncertainty estimate is based on the average 95% confidence interval assigned to the Mg/Ca records synthesized for the Eocene in Hollis et al. (2019), where the DeepMIP community did a thorough assessment of the impacts of the above-mentioned factors on Mg/Ca uncertainty for the Eocene. While a comparable assessment for the Miocene Mg/Ca records is planned, this serves as an appropriate intermediate estimate. Given that the number of ocean surface temperature records from high latitude regions is limited, future analysis may consider comparing against published benthic temperature records.

Late Miocene reconstructed values are defined as all available estimates from a given site falling between 11.6 and 5.33 Ma and Middle Miocene reconstructed values are defined as all available estimates falling between 15.97 and 11.63 Ma. It is important to note that the records differ in temporal resolution and while some records span the entire interval, others cover only a portion. To partially address the caveat that some records are more representative of the end of the Middle Miocene interval while others the beginning, and given that significant cooling occurs toward the end of the Middle Miocene (end of the Langhian though the Serravallian), the sensitivity of the model-data SST bias results to focusing on a narrower interval within the MCO (14.5–16.75 Ma) has been assessed—noting however that fewer sites are available for the comparison after this refinement.

3.3. Model-Data Comparison Methodology

The model-data comparison methodology employed in Section 4.3 is similar to that used in previous Miocene studies (Bradshaw et al., 2012, 2015). For each site, the one standard deviation (68%) uncertainty intervals are added to the mean reconstruction values across the given timeslice and the site location is translated back to an estimated paleolocation. The method used to estimate these paleolocations uses plate reconstructions consistent with the paleogeographies described in Markwick and Valdes (2004) that were based on Rowley (1995, pers. comm.). All model output is interpolated, using bilinear interpolation, to a common 1-degree by 1-degree grid. Reconstructed values are compared to the minimum and maximum values simulated in the model grid cell containing the reconstructed data, and all adjacent model grid cells. This allows for data location uncertainties and model uncertainties such as the misplacement of large-scale climate features (it is unreasonable to expect a model to reconstruct the exact climate of a single grid cell, also note that by using degrees this encompasses a larger zonal distance in the tropics than high latitudes). Since the model simulations and data reconstructions are ranges of possible values rather than a single value, the term overlap is used to define where the two value ranges are consistent (see Figure S1). Bias between the model and data is determined where there is no overlap between the model and data uncertainty ranges and the magnitude of this bias is determined by the degree of separation between the uncertainty intervals of the two data sets (see Figure S1, note that as illustrated in Figure S1 this represents the minimum possible bias within the given uncertainty ranges). When, for a given model setup, a grid point that corresponds with a given terrestrial MAT (SST) site location, as well as its neighboring grid points, are in the ocean (over land) the site is removed from the bias calculation.

Note that rather than using the mean reconstructed SST values for the given time interval, ± the assigned data uncertainty, an alternative approach would be to fully encompass the variability in SST estimates seen across the Late Miocene, Middle Miocene, and MCO time intervals and use maximum and minimum recorded values plus uncertainty—as in Bradshaw et al. (2012, 2015). Given that the SST reconstructions have varying temporal resolutions, and are not collocated in time, this approach has the potential to mask spatial covariance signals (e.g., a higher resolution record can capture more of the sample variance even when the two samples have similar means, which in turn could lead to a smaller "bias" derived using the approach outlined above, even though the means are similar). Given that this paper focuses on the ability of Miocene simulations to represent gross features of Miocene warmth, we feel that the use of mean reconstructed SST values is more appropriate in this context.

3.4. Global Mean Surface Temperature Estimates

Global Mean Surface Temperature (GMST) estimates for the Late Miocene, Middle Miocene, and MCO are calculated using the proxy MAT and SST syntheses compiled (Section 3.2). We use a method that has been previously employed to provide Eocene GMST estimates. Despite its simplicity, when applied to the same set of Eocene temperature reconstructions (Hollis et al., 2019), this method produces values that are largely consistent with a range of other methods (Inglis et al., 2020). The zonal mean temperature (T) profile at sea level is approximated using a simple model:

$$\mathrm{T}\left(\phi\right) \approx a + b\theta + c\cos\phi \tag{1}$$

where coefficients a, b, and c are chosen to minimize the sum of the squared residuals relative to the Miocene surface temperature proxy data (Figure 3). As demonstrated in Figure 3 of Inglis et al. (2020), this model provides an accurate approximation of the modern $\mathrm{T}\left(\phi\right)$ profile. For both the MAT and SST data, we account for the uncertainty in each temperature estimate by assuming a normal probability distribution around each temperature estimate with the stated uncertainty interval treated as the 90% confidence interval. For the MAT data, we also account for the uncertainty in the elevation of each site by assuming a skew-normal distribution with a 90% confidence interval equal to the lowest and highest elevations within all paleotopographic grid points adjacent to the given site (with a lower bound of zero). For the Middle Miocene and MCO calculations, the paleotopography from the Middle Miocene paleogeography described in this article (updated Herold, Huber, and Müller [2011]) is used, while the Knorr et al. (2011) paleogeography is used for the Late Miocene. The temperature and elevation distribution at each site is then randomly sampled and corrected to sea level by applying a lapse-rate adjustment of 6 K/km. This implies that errors in the paleotopography may influence the estimate of global mean surface temperature, and the resolution and fidelity of the paleotopography used will be a possible source of errors when the terrestrial data is included. Using a standard Monte Carlo bootstrapping method, we resample the same number of data points with replacement and find the coefficients in Equation 1 that best fit the sub-sampled data. A probability distribution for $\mathrm{T}\left(\phi\right)$ is found by repeating this procedure 10,000 times. The result is shown in Figure 3, with

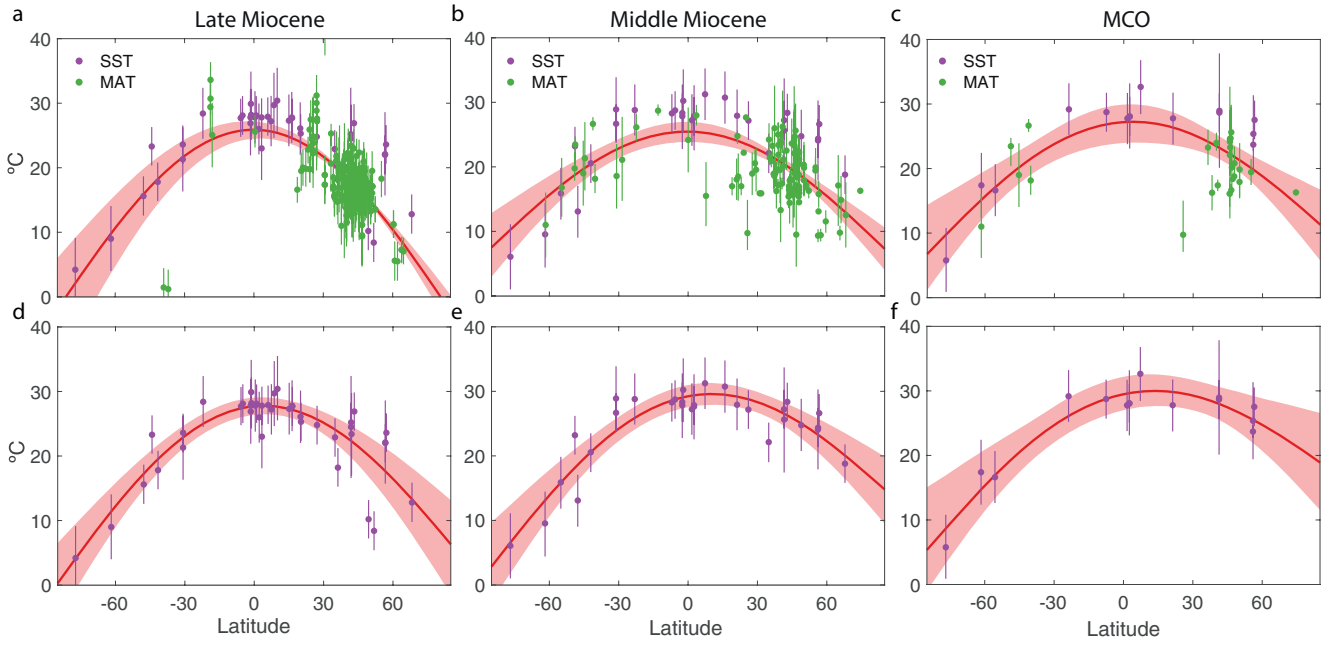

Figure 3. (Top row) Average zonal mean surface temperature estimate (red line), ± one standard deviation (red shading), computed from proxy MAT (green) and SST (purple) data for (a) the Late Miocene, (b) Middle Miocene, and (c) MCO. (Bottom row) Average zonal mean surface temperature estimate calculated using only the SST (purple) data for (d) the Late Miocene, (e) Middle Miocene, and (f) MCO.

shading indicating ± one standard deviation. The latitudinally weighed average of $T(\phi)$ is taken to provide an GMST estimate with an associated uncertainty of one standard deviation.

3.5. Zonal Mean Energy Balance Analysis

To establish the relative contribution of energy flux convergence and each radiative component to the meridional warming patterns within the Miocene simulations, we employ a 1-D zonal mean energy balance analysis framework (Feng et al., 2017; Heinemann et al., 2009; Hill et al., 2014; Lunt, Dunkley Jones, et al., 2012; Lunt, Haywood, et al., 2012; Lunt et al., 2020). 1-D energy balance is used to approximate zonal mean surface temperature:

$$C\partial_t T(\phi) = SW^{\downarrow}_{toa}(\phi)\left[1-\alpha(\phi)\right] + H - \varepsilon\sigma T(\phi)^4 \quad (2)$$

where $T(\phi)$ is the zonal mean surface temperature, a function of latitude, ϕ. $SW^{\downarrow}_{toa}$ is the incoming shortwave radiation at the top of the atmosphere, α the planetary albedo defined as $\alpha = \frac{SW^{\uparrow}_{toa}}{SW^{\downarrow}_{toa}}$, H is the combined atmospheric and oceanic energy flux convergence defined as $H = -\left(SW^{net}_{toa} + LW^{net}_{toa}\right)$, ε is a measure of the emissivity of the atmosphere where $\varepsilon = \frac{LW^{\uparrow}_{toa}}{LW^{\uparrow}_{surf}}$, and C is the surface heat capacity. When applied to equilibrated or near equilibrated, annual-mean, climatological fields, the term on the left-hand side is negligible, and simulated zonal mean surface temperature profiles are well approximated by the balance on the right-hand side of Equation 2. This balance is between net downward shortwave, net outgoing longwave, and the convergence of energy by atmospheric and ocean energy transport, such that the solution for

$$T(\phi) = \left[\frac{SW^{\downarrow}_{toa}(\phi)\left[1-\alpha(\phi)\right] + H(\phi)}{\varepsilon(\phi)\sigma}\right]^{0.25} \equiv T(\varepsilon,\alpha,H)$$

The change in $T(\phi)$ between each Miocene experiment and its respective control is then $\Delta T(\phi) = T(\varepsilon,\alpha,H) - T(\varepsilon',\alpha',H')$, where the prime represents the control simulation. Given that changes in ε, α and H are small relative to their absolute values, the contribution of changes in emissivity, albedo and heat transport can be approximated as $\Delta T(\phi) \cong \Delta T_{emm}(\phi) + \Delta T_{alb}(\phi) + \Delta T_{tran}(\phi)$, where $\Delta T_{emm}(\phi) = T(\varepsilon,\alpha,H) - T(\varepsilon',\alpha,H)$, $\Delta T_{alb}(\phi) = T(\varepsilon,\alpha,H) - T(\varepsilon,\alpha',H)$ and $\Delta T_{tran}(\phi) = T(\varepsilon,\alpha,H') - T(\varepsilon',\alpha,H)$.

Using clear-sky (cs) radiative fluxes ΔT_{emm} can be decomposed into the contribution due to the greenhouse effect (CO_2, water vapor, and lapse rate), $\Delta T_{gg}(\phi) = T(\varepsilon_{cs},\alpha_{cs},H_{cs}) - T(\varepsilon'_{cs},\alpha_{cs},H_{cs})$, and longwave cloud changes $\Delta T_{lwc}(\phi) = \Delta T_{emm}(\phi) - \Delta T_{gg}(\phi)$. Similarly ΔT_{alb} can be decomposed into the contribution of clear-sky changes due to surface albedo and aerosols, $\Delta T_{salb}(\phi) = T(\varepsilon_{cs},\alpha_{cs},H_{cs}) - T(\varepsilon_{cs},\alpha'_{cs},H_{cs})$, and shortwave cloud changes $\Delta T_{swc}(\phi) = \Delta T_{alb}(\phi) - \Delta T_{salb}(\phi)$.

There are limitations in this diagnostic approach, particularly when it comes to separating out the changes due to clear-sky and cloud radiative forcing in the presence of sea-ice, and we have not separated the contribution of changes in surface elevation from the greenhouse effect. Nevertheless, it provides insight into the relative contribution of the five components, $\Delta T(\phi) \cong \Delta T_{gg}(\phi) + \Delta T_{lwc}(\phi) + \Delta T_{salb}(\phi) + \Delta T_{swc} + \Delta T_{tran}(\phi)$, based on what was feasible given the output available within our MioMIP data set.

4. Results

4.1. Global Mean Temperature

Across all the Miocene experiments, which span a range of models and paleogeographic boundary conditions, prescribed CO_2 concentration exerts the primary control on the global mean temperature change

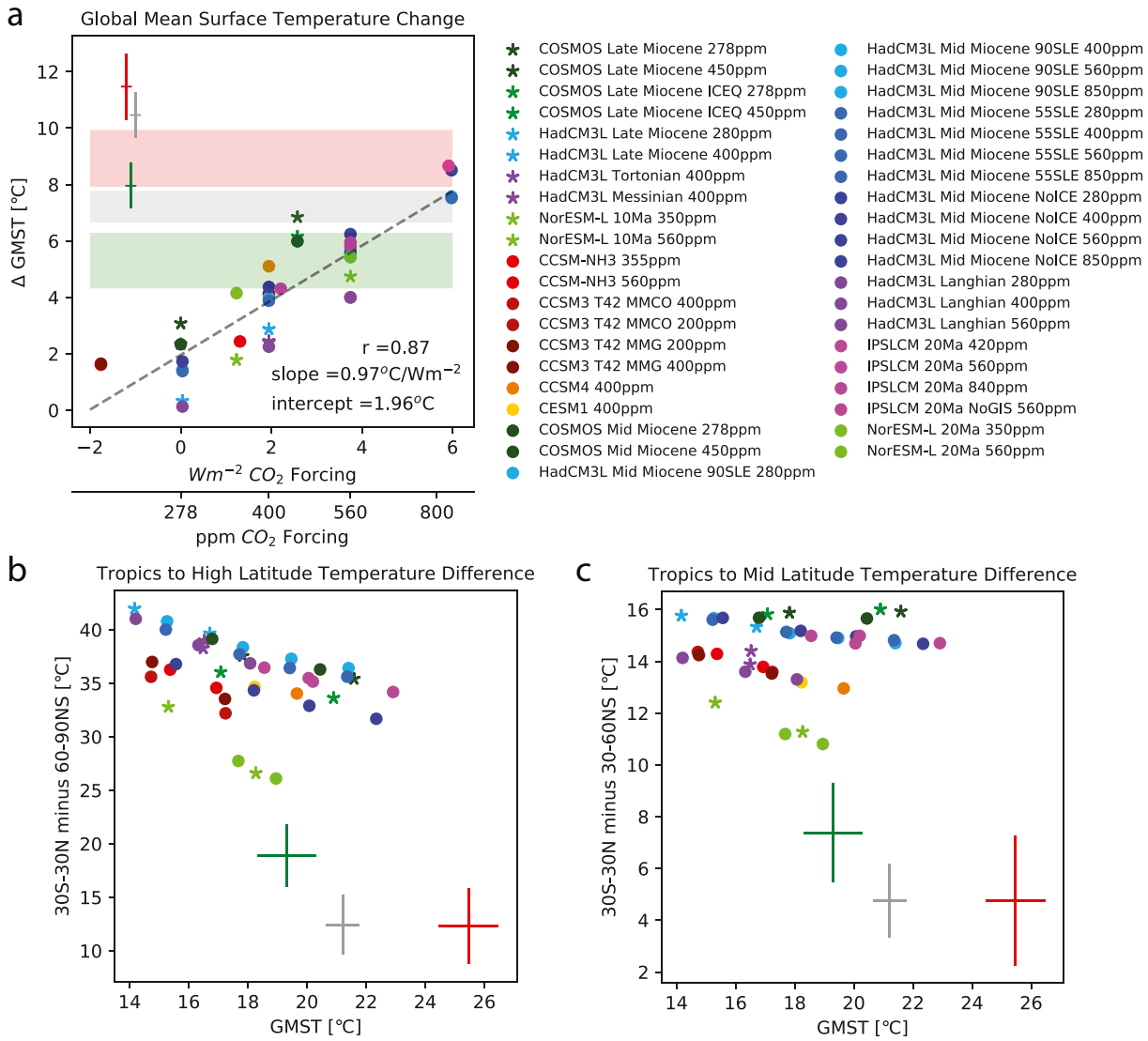

Figure 4. (a) The global mean surface temperature change (relative to the preindustrial control) versus prescribed atmospheric CO_2 concentration. The green, gray, and red shading indicate the Late Miocene, Middle Miocene, and MCO global mean surface temperature change estimates derived from the mean annual terrestrial and sea surface temperature reconstructions (Figure 3, top row), while the crosses show the equivalent global mean surface temperature change estimates based only on the sea surface temperature proxies (Figure 3, bottom row). (b and c) Global mean surface temperature versus (b) the tropics (30°S–30°N) to high latitude (60–90°N and °S) temperature difference and (c) the tropics (30°S–30°N) to middle latitude (30–60°N and °S) temperature difference. The green, gray, and red crosses indicate the Late Miocene, Middle Miocene, and MCO estimates derived from the mean annual terrestrial and sea surface temperature reconstructions (Figure 3, top row).

relative to the preindustrial control climate, explaining around 75% of the variance (Figure 4a). The best fit regression across these experiments is for a climate sensitivity of 0.97℃/Wm^{-2} which assuming ~3.7 Wm^{-2} per CO_2 doubling (this is less valid when doubling at higher CO_2; Etminan et al., 2016) translates into ~3.6°C per doubling. This first-order linear relationship can be used to provide a few additional insights based on this particular ensemble performed with a broad range of boundary conditions reflective of how conditions may have changed throughout the Miocene. First, the *X*-intercept suggests that the mean impact of the range of non–CO_2 Miocene boundary conditions used is to raise global mean surface temperature by 1.96°C (this statement ignores nonlinear interactions between CO_2 induced temperature changes and temperature changes induced by other changes in the boundary conditions but provides an insightful starting point). Second, deviations from this first order linear relationship range from −1.87°C to 2.39°C providing an indication of the spread in warming responses arising due to a combination of the spread in imposed

boundary conditions, as well as the spread in climate feedback strengths across models. Using the above stated climate sensitivity estimate of 0.97℃/Wm^{-2} as an example, this spread in global mean temperature responses is equivalent to an uncertainty of 4.4Wm^{-2} or 1.2 times the forcing from a CO_2 doubling.

As described in Section 3.4, GMST estimates ± one standard deviation have been calculated using the Late Miocene, Middle Miocene and MCO syntheses described in Section 3.2. Two different estimates have been derived for each interval, first an estimate derived using both the terrestrial MAT and SST data sets (Figure 3, top row), and second an estimate based on only the SST data (Figure 3, bottom row). When both the terrestrial MAT and SST are included, this method estimates Late Miocene GMST as 19.30°C ± 0.98°C, Middle Miocene GMST as 21.21°C ± 0.56°C and MCO GMST as 22.93°C ± 1.01°C. If the terrestrial sites are excluded, these GMST estimates based only on SST reconstructions are substantially warmer: Late Miocene GMST 21.95°C ± 0.81°C, Middle Miocene GMST 24.46°C ± 0.81°C and MCO GMST 25.47°C ± 1.17°C. There are several reasons why the terrestrial data might bias the estimate cold, including calibration techniques biased toward the modern temperature range and that many of these records are from mountain ranges (while we have applied a lapse rate correction, it is only as good as our elevation estimate derived from a low resolution paleotopography product which might lead to a cold/warm biasing). On the other hand, the number of SST reconstructions is limited such that increasing the sample size is needed to constrain the large uncertainty in GMST that falls out of our analysis. Using a preindustrial value of 14°C (Hansen et al., 2013), Figure 4a compares these Miocene GMST estimates with the simulated GMST changes. For the Middle Miocene and MCO, with the exception of the COSMOS Late Miocene simulation with 450 ppm CO_2, only Middle to Early Miocene simulations with 840–850 ppm CO_2 intersect with the GMST change estimates based on both terrestrial MAT and SST. All the simulations fall below the higher SST-only Middle Miocene and MCO GMST change estimates. Of the Late Miocene simulations, the COSMOS simulation with 450 ppm and 25% of the modern Antarctic ice sheet height, and the NorESM-L simulation with 560 ppm CO_2, intercept the reconstructed Late Miocene GMST change estimate based on both terrestrial MAT and SST. None of the Late Miocene simulations intercept the reconstructed Late Miocene GMST change estimate based only on SST.

4.2. Warming Patterns

Starting with the zonal-mean changes in surface temperature (Figures S2 and S3), across the entire ensemble the magnitude of tropical warming spans ~0°C–8°C, while high-latitude warming (latitude > 60°N and °S) spans ~0°C–38°C in the SH and ~0°C–18°C in the NH. While there is substantial spread in its magnitude, polar amplified warming is a robust feature across the ensemble (Figure 5). The wide range of warming responses seen in the SH reflects the range of boundary conditions prescribed for the Antarctic Ice Sheet given the uncertainty in its evolution across the Miocene. Interestingly, once the zonal-mean responses are stratified by prescribed CO_2 concentration, there does not appear to be a consistent mapping between the degree of high-latitude warming and tropical warming, with the degree of polar amplification ranging substantially across the experiments (e.g., when looking at the 560 ppm experiments in Figure S3 widely different high latitude warming due to varying ice sheet extents has a limited impact on tropical temperatures). This result points to a somewhat limited impact of high-latitude glacial changes on the tropics relative to the more systematic influence of CO_2 on tropical temperature (Figure 5). This feature appears to hold not only across the different models, but within a given model, namely HadCM3L, for which experiments with a range of Antarctic ice-sheets display considerable variability in high-latitude surface temperature but limited variability in tropical temperature (Figure S3).

Stratifying the energy balance analysis by prescribed CO_2 concentration we see that a stronger polar greenhouse effect (due to CO_2, water vapor and lapse rate) and decreased surface albedo, are the dominant contributors to the polar amplified warming—a result consistent with the literature on future climate change, for example, Pithan and Mauritsen (2014). One caveat with differencing the all-sky and clear-sky to separate the surface and cloud albedo components is that the masking of surface albedo changes by clouds is not adequately deconvolved, particularly in the presence of sea ice. For example, in a polar region where climatologically high cloud cover largely masks the influence of surface albedo, the method will overestimate the contribution of reduced surface albedo given that the cloud albedo is taken as the residual between total albedo and surface albedo. Therefore, the method can incorrectly indicate a cooling signal due to cloud albedo changes even if cloud properties remain similar to the control. Given this caveat, the high-latitude

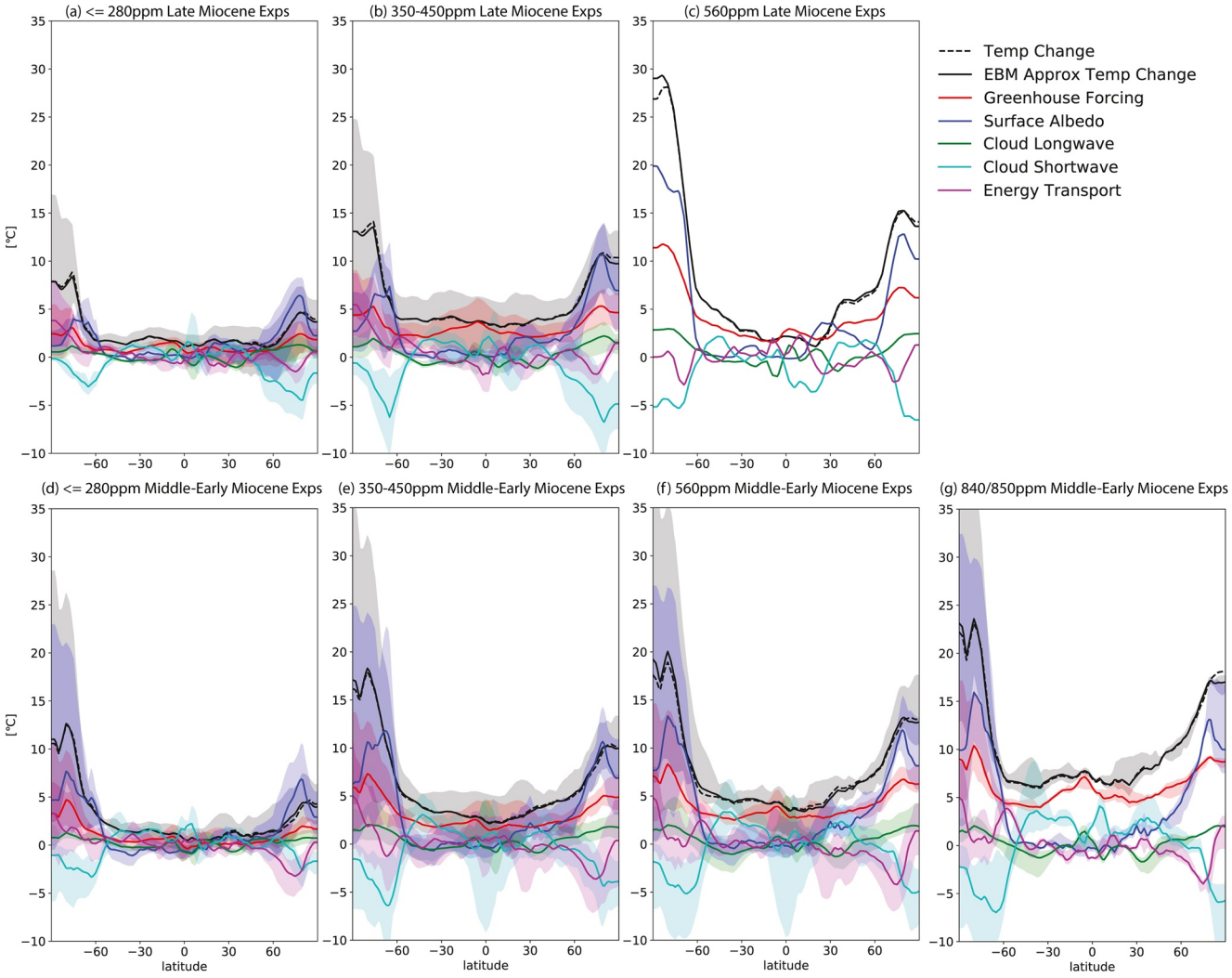

Figure 5. The multi-model-mean of the energy balance analysis for the set of Late Miocene experiments with (a) 278 or 280 ppm, (b) 350–450 ppm, and (c) 560 ppm CO_2, and the set of Middle-Early Miocene experiments with (d) 278 or 280 ppm, (e) 350–450 ppm, (f) 560 ppm, and (g) 840/850 ppm CO_2. Note that the variables required for this analysis were not available for the HadCM3L Tortonia, Messinian, and Langhian experiments, see Figures S2 and S3 for the individual experiments.

cooling/warming signal seen in Figure 5 due to changes in cloud/surface albedo may not be as strong as the analysis suggests. Regardless, the total albedo change due to the combined effect of surface and cloud albedo changes is a dominant driver of high-latitude warming. Interestingly, across the ensemble, changes in oceanic and atmospheric energy flux convergence tends to warm the southern high-latitudes and cool the northern high latitudes (there are of course exceptions, Figures S2 and S3). Cloud longwave forcing are generally second order. Equatorward of ~60°N and °S the warming signal is generally more uniform with the greenhouse effect term dominating as a function of CO_2 concentrations. With this uniformity in mind it is not surprising that while the tropics to high-latitude temperature difference generally scales as a function of global warming across the ensemble (Figure 4b), the tropics to mid-latitude temperature difference only displays a weak sensitivity, with the exception of the NorESM (Figure 4c).

Moving beyond the zonal-mean, the two-dimensional annual mean surface temperature changes for each of the Late and Middle to Early Miocene simulations, relative to their preindustrial control simulations, are shown in Figures S4 and S5, respectively. The limited impact of high-latitude glacial changes relative to CO_2 forcing on tropical warming is further illustrated when looking at the two-dimensional warming patterns stratified according to imposed CO_2 concentration (Figure 6). The ensemble mean captures the average

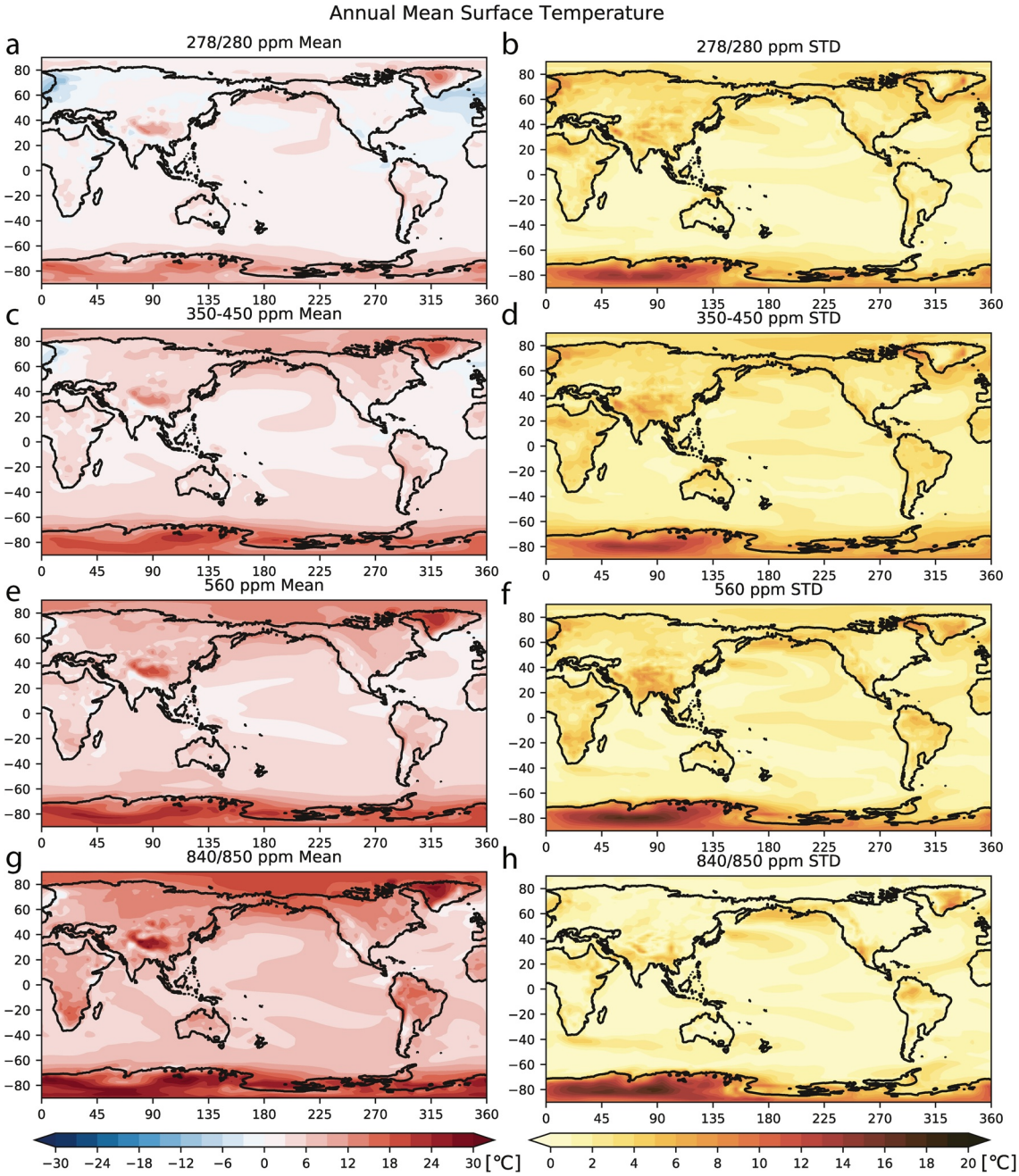

Figure 6. (Left) The multi-model-mean of the annual mean surface temperature change relative to the preindustrial control for the set of experiments with (a) 278 or 280 ppm, (c) 350–450 ppm, (e) 560 ppm, and (g) 840/850 ppm CO_2. (Right) The standard deviation of this temperature change across the experiments making up each set. The continental outline from the updated Herold, Huber, and Müller (2011) paleogeographic boundary conditions described in this study has been used (see supporting information).

response to a given CO_2 concentration across a range of models and Miocene boundary conditions, and broadly indicates an increase in the degree of polar amplification with CO_2. When looking at the variability in warming for a given CO_2 range, the influence of the range of boundary conditions prescribed for the Antarctic Ice Sheet is most evident, giving rise to a substantial range in warming responses over the Antarctic continent. Particularly striking is the limited footprint of this variability. Other dominant sources of spread in the surface temperature response for a given CO_2 concentration include differences in continental warm-

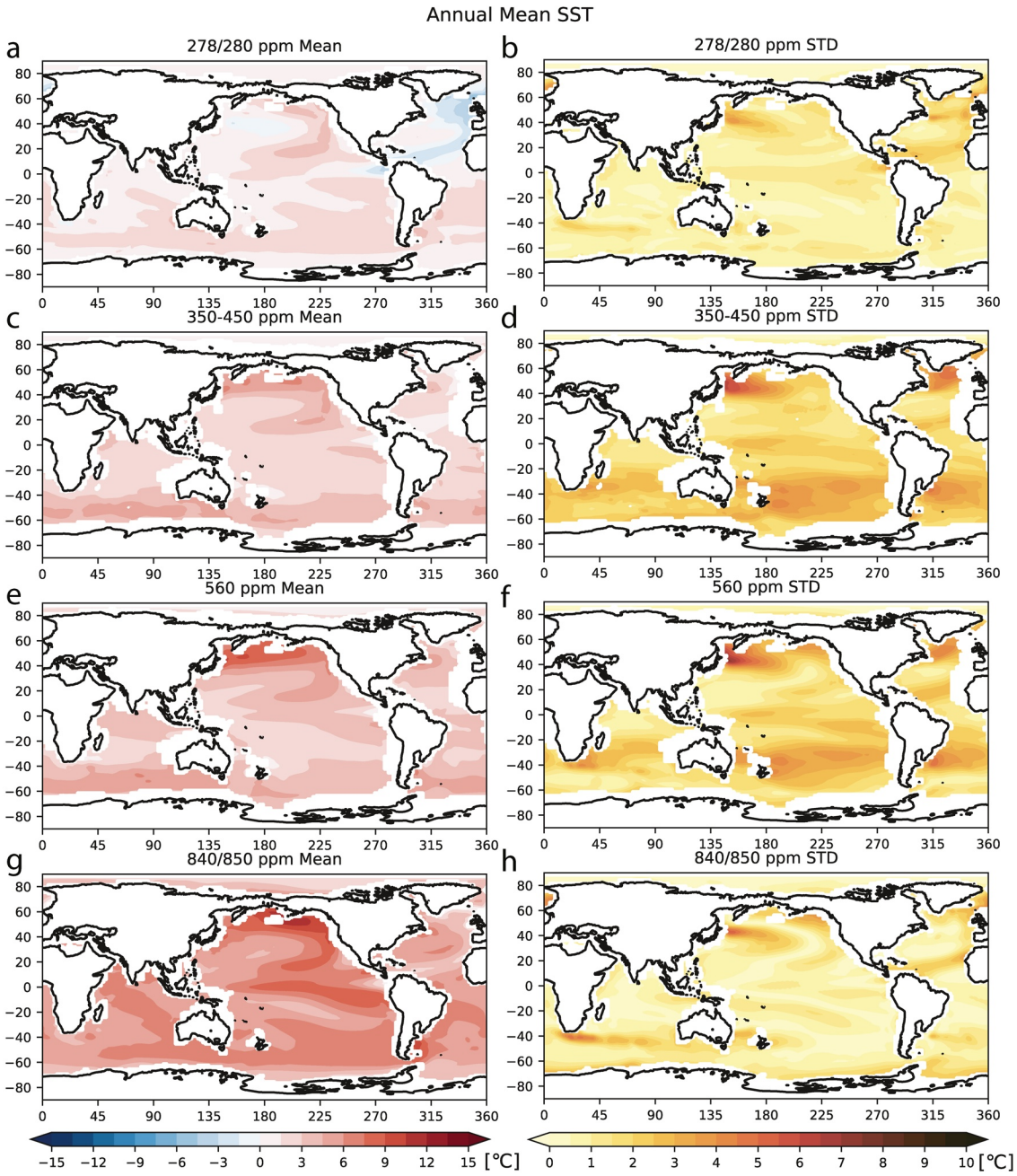

Figure 7. (Left) The multi-model-mean of the annual mean sea surface temperature change relative to the preindustrial control for the set of experiments with (a) 278 or 280 ppm, (c) 350–450 ppm, (e) 560 ppm, and (g) 840/850 ppm CO_2. (right) The standard deviation in this temperature change across the experiments making up each set. The continental outline from the updated Herold, Huber, and Müller (2011) paleogeographic boundary conditions described in this study has been used (see supporting information).

ing. Hotspots like North Africa are presumably due to variability in vegetation changes, either prescribed or dynamic. While differences in prescribed orography may be more important in regions like Southern Asia.

Variability in ocean warming seen across the MioMIP ensemble, once stratified by CO_2 concentration, is muted relative to the spread in warming signals seen over the continents (Figure 7, note the difference in the standard deviation (STD) color bar range when compared to Figure 6), but still substantial. There are several hotspots of large spread in the response seen across the models. First, the spread across models in the degree of warming experienced in the Pacific cold tongue region (typically the central to south-eastern equatorial Pacific, but depending on model biases, this can extend well into the western Pacific) is larger

(STD between 2°C and 4°C) than in the Indo-Pacific and eastern Pacific warm pool regions (STD < 2°C). This result indicates that for a given CO_2 forcing there is considerable spread across models in the warming of equatorial upwelling regions relative to the rest of the tropics, and hence in the zonal gradient response. This disagreement in the response of the tropical Pacific to warming across models is not unique to simulating the Miocene. There is considerable disagreement across CMIP models in the historical and projected response of the tropical Pacific (Kociuba & Power, 2015), due to complex and competing atmosphere-ocean interactions operating on a range of timescales (Heede et al., 2020). Other hotspots in the spread in the SST response include the subpolar gyres in the North Atlantic and Pacific basins and the Southern Ocean. Possible explanations for differing model responses in these regions include differing dynamical responses in wind-driven and thermohaline ocean circulation or regional cloud feedbacks. Alternatively, the model circulation responses might be dynamically similar but there are differences in the extent to which gyre boundaries have shifted.

Speaking specifically to the role of the spread in shortwave cloud feedbacks, Figure S7 confirms that the above-mentioned hotspots of variable SST responses do tend to correspond with hotspots of variable cloud albedo responses - clouds being the primary cause of TOA albedo changes over ocean regions too warm for sea-ice (Figure S7). There are several notable features in the model mean TOA albedo response stratified by CO_2 forcing. First, the north-south dipole signature seen in the eastern equatorial Pacific for all CO_2 concentrations indicates a southward shift in convection and the ITCZ. Similarly, increased albedo in the central Pacific relative to the western Pacific Maritime continent region is indicative of an eastward expansion of tropical convection in the Pacific basin, with a similar westward expansion in the Indian Ocean, a feature consistent with the enhanced ensemble mean SST warming in these regions relative to the western Pacific (Figure 7). Second, the model mean TOA albedo decreases over the subtropical to mid-latitude ocean, more so at higher CO_2 levels (Figure S7). This shortwave cloud feedback mechanism (Figure 5) contributes to

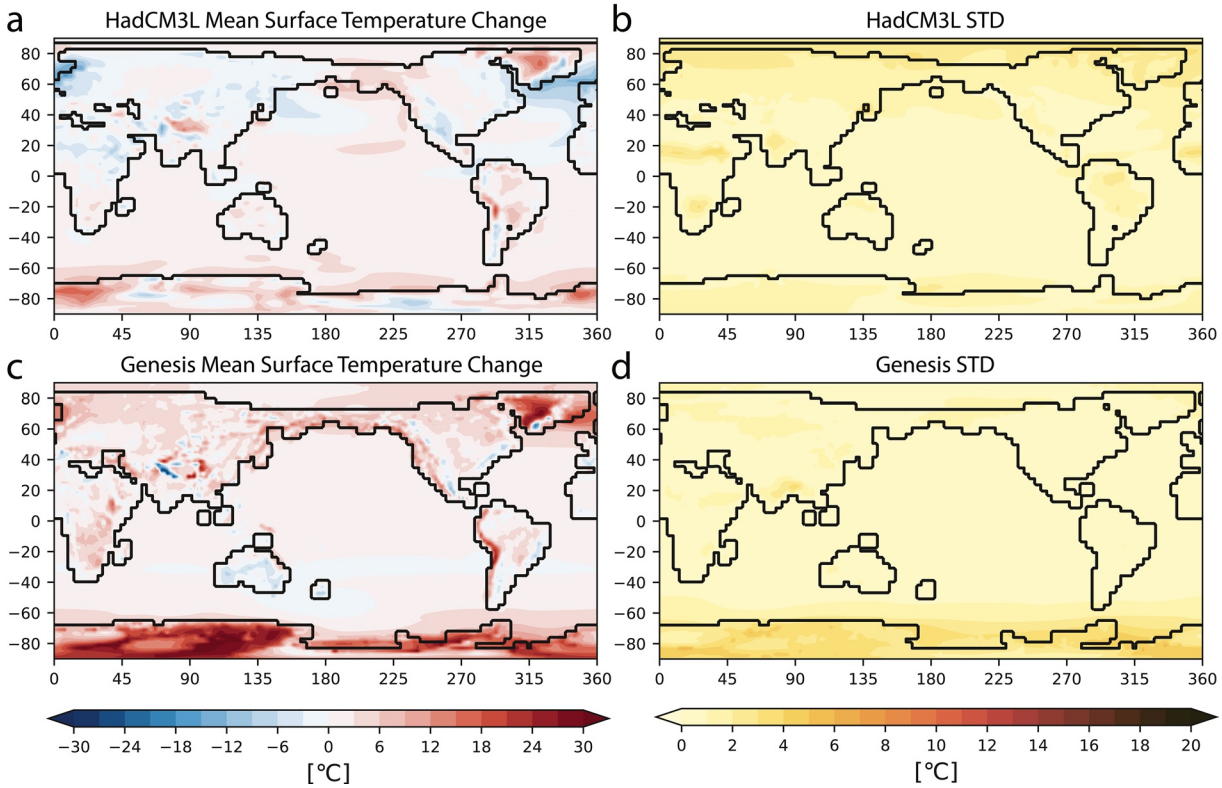

Figure 8. (Left) The multi-model-mean of the annual mean surface temperature change relative to the preindustrial control for the Orbital sensitivity simulations outlined in Table 3 (a) HadCM3L, (c) Genesis (Table 3, only the simulations that have 280 ppm CO_2). (right) The standard deviation in this temperature change across the experiments making up each set of (b) HadCM3L, (d) Genesis 280 ppm CO_2 experiments. *Note*. That the same color bar as in Figure 5 has been used to facilitate comparison. See Figure S6 for a version of the standard deviation plots that has a colorbar that ranges from 1°C to 10°C.

weaker midlatitude to tropical surface temperature gradients with higher CO_2, but as the model-data comparison results in the next section reveal, this does not manifest in enough midlatitude warming to match reconstructed SSTs from these latitudes—with perhaps the exception of the Late Miocene NH at 560 ppm. This in turn has implications for the ability of Miocene simulations to reproduce the reconstructed weakening of the meridional SST gradient between the tropics and the subtropics to mid-latitudes (Figure 4c); and potentially the enhanced warming seen in the eastern equatorial Pacific sites following the ocean tunnel mechanism - whereby the ocean wind-driven subtropical cells communicate subtropical warming signals to equatorial upwelling regions (Erfani & Burls, 2019; Fedorov et al., 2015). Third, Southern Ocean TOA albedo increases poleward of ~50°S, a feature seen in future projections associated with a southward shift in the storm tracks (Ceppi et al., 2014; Shaw et al., 2016). Finally, reductions in both land and sea ice lead to model mean TOA albedo decreases in both the NH and SH high latitudes, with variability in the prescribed extent of ice sheets leading to the large STDs seen over both Antarctica and Greenland (Figure S7).

Sensitivity tests to differences in astronomical parameters were performed with two models in the MioMIP ensemble (Figure 8). Compared with the sensitivity to other uncertain boundary conditions, these results show important, yet relatively small (comparing Figure 8 with Figure 6), and regional, surface temperature sensitivity to changes in orbit. Simulations with differences in atmospheric CO_2 and Antarctic Ice Sheet extent show an increasing sensitivity to astronomical forcing with decreasing CO_2 and with decreasing ice sheet extent (Figure S6). The sensitivity to CO_2 is likely linked to sea ice extent. There is minimal sea ice in the high atmospheric CO_2 simulations, and with lower atmospheric CO_2 the sea ice extent increases as does the variability in sea ice area between simulations with different astronomical boundary conditions. Similarly, in the absence of an Antarctic Ice Sheet, there is greater variability in the Antarctic land surface albedo and increased sensitivity to changes in orbit. It is worth noting that orbital variability during the Miocene likely would have been accompanied by some sort of CO_2 variability (as in the Quaternary), and therefore the magnitude of orbitally induced climate change modeled here is a minimum estimate.

4.3. Model-Data Comparison

Starting with the Late Miocene, Figures 9 and 10 compare the simulated zonal-mean land and SST profiles for all the experiments targeting the Late Miocene against available proxy data estimates. The experiments are again stratified by CO_2 forcing. Both the terrestrial and SST records indicate a reduced meridional surface temperature gradient (Figures 9 and 10). Generally speaking, subtropical to midlatitude warmth tends to fall into better alignment with the proxy data as CO_2 levels increase. For the Northern Hemisphere, the NorESM-L simulation with 10 Ma boundary conditions and 560 ppm of CO_2 appears to provide a reasonable fit from a zonal mean SST perspective (Figure 10), but there are however large zonal asymmetries such that midlatitude SSTs are too warm in the Pacific basin, yet too cold in the Atlantic (Figures 13e and S9). Although still falling short of the proxy estimate, this experiment simulates one of

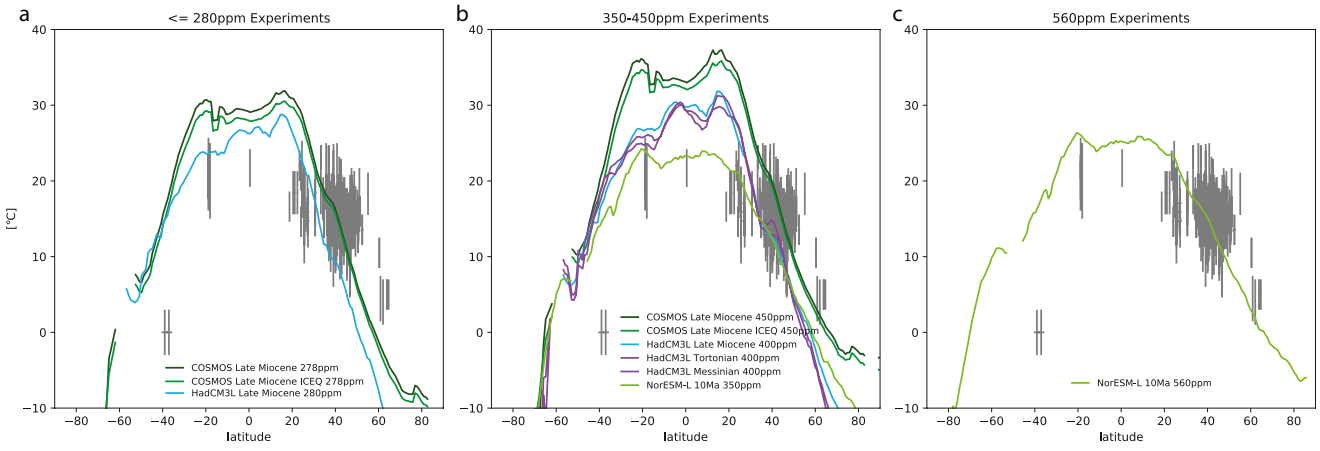

Figure 9. Zonal-mean, annual-mean land surface temperature for all Late Miocene experiments. Superimposed in gray are Late Miocene in age mean annual terrestrial temperature reconstructions. Each panel distills the Late Miocene experiments by prescribed atmospheric CO_2 concentration.

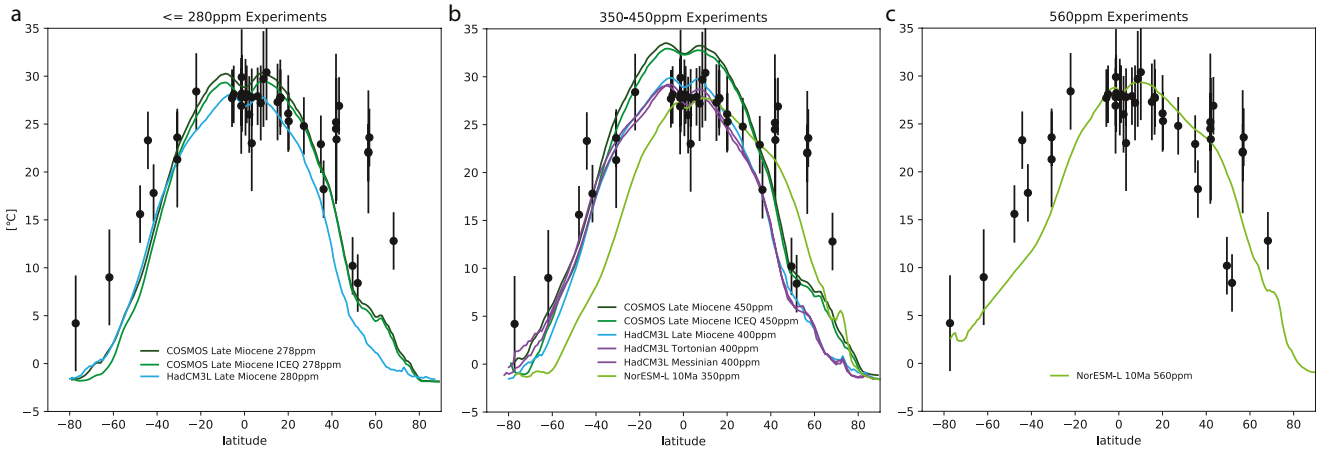

Figure 10. Zonal-mean, annual-mean, sea surface temperature for all Late Miocene experiments. Superimposed in black are Late Miocene in age mean annual sea surface temperature reconstructions. Each panel distills the Late Miocene experiments by prescribed atmospheric CO_2 concentration.

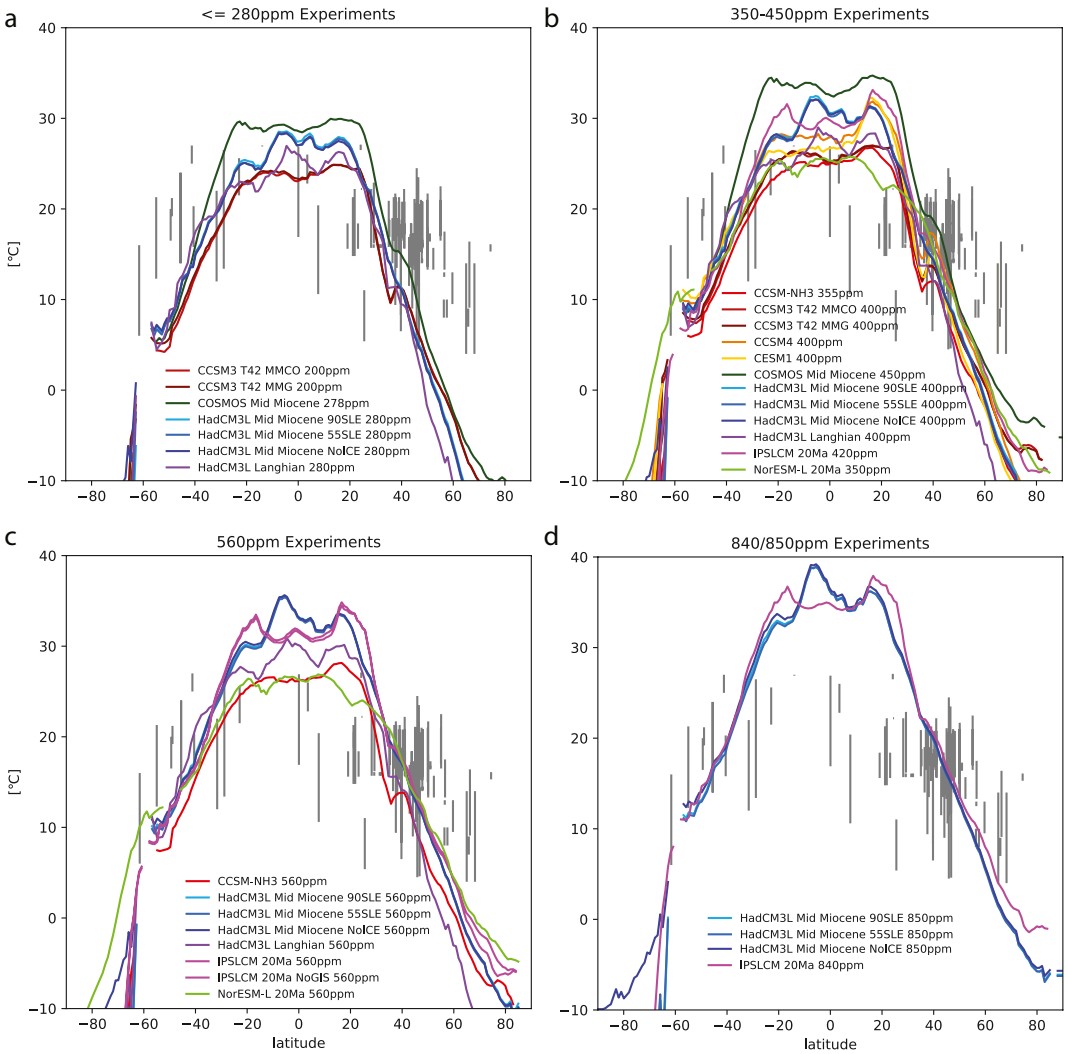

Figure 11. Zonal-mean, annual-mean land surface temperature for all Middle-Early Miocene experiments. Superimposed in gray are Middle Miocene in age mean annual terrestrial temperature reconstructions. Each panel distills the Middle and Early Miocene experiments by prescribed atmospheric CO_2 concentration.

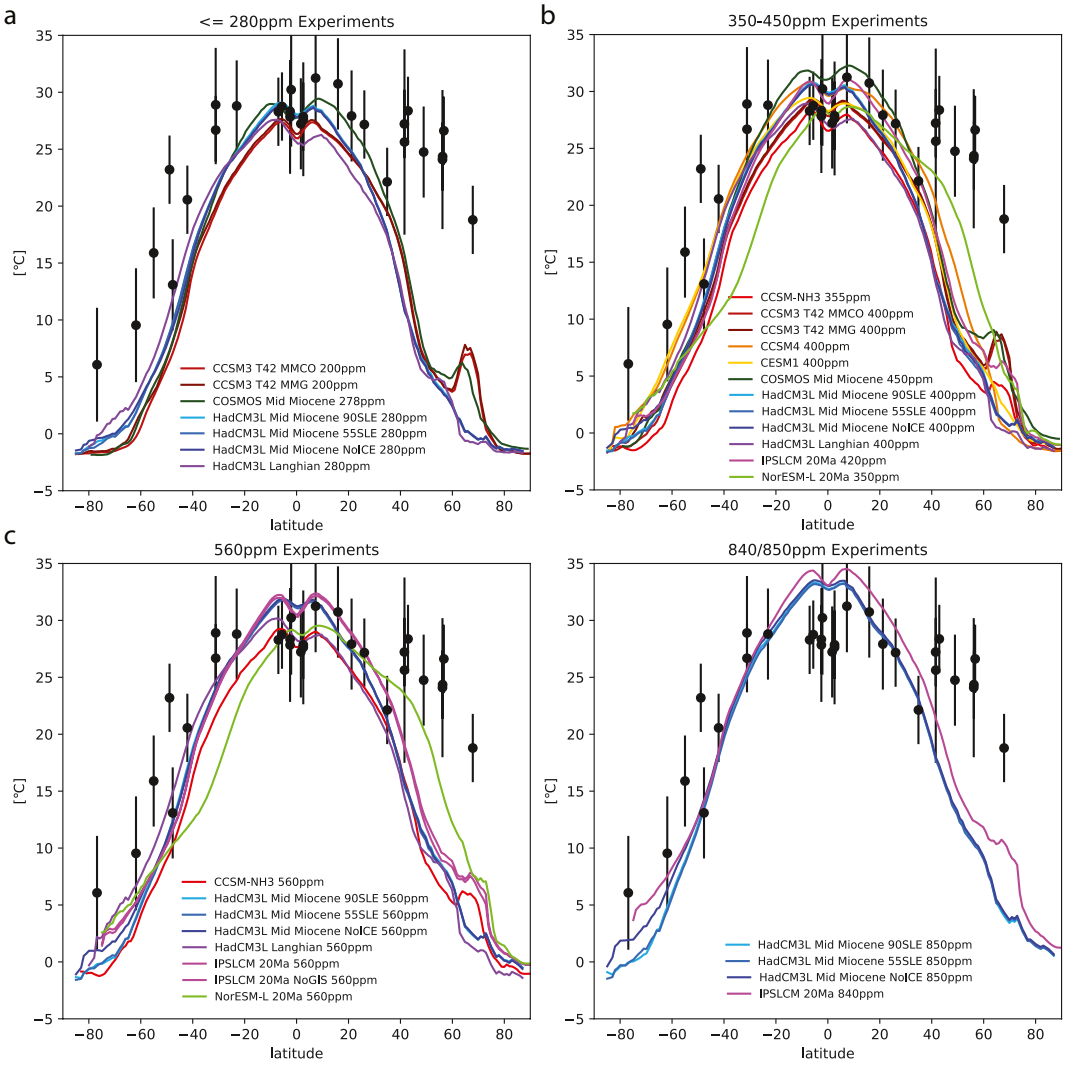

Figure 12. Zonal-mean, annual-mean, sea surface temperature for all Middle and Early Miocene experiments. Superimposed in black are Middle Miocene in age mean annual sea surface temperature reconstructions. Each panel distills the Middle to Early Miocene experiments by prescribed atmospheric CO_2 concentration.

the strongest relaxations of the meridional temperature gradients (Figure 4) with only a few degrees of tropical warming, between ~4°C and 8°C of subtropical warming, and significant high latitude warming, exceeding well over 20°C in the Antarctic. It also provides one of the best fits with the terrestrial data (Figure 9). With Late Miocene CO_2 estimates spanning ~300–450 ppm (Figure 1), one might expect the experiments forced with 350–450 ppm of atmospheric CO_2 to provide the best fit with that data. When looking at the mean SST bias across simulations (Figure 13), the root-mean-square error (RMSE) is lowest for 560 ppm (Figure 13e). That said, there is still the general indication that the deep tropics are warming too much while the mid- to high-latitudes are too cold (Figure 13c). It also appears that the zonal gradient in the equatorial Pacific is generally too strong in the models with not enough warming over the eastern Pacific cold tongue region and too much warming in the western Pacific (Figure 13c). From the perspective of the terrestrial MAT proxies, the 560ppm Late Miocene simulation leads to the lowest RMSE (Figure 13f).

Moving on to the Middle Miocene, both the terrestrial and SST proxies point to a further weakening of the meridional surface temperature gradient with a strikingly flat temperature gradient between the tropics and

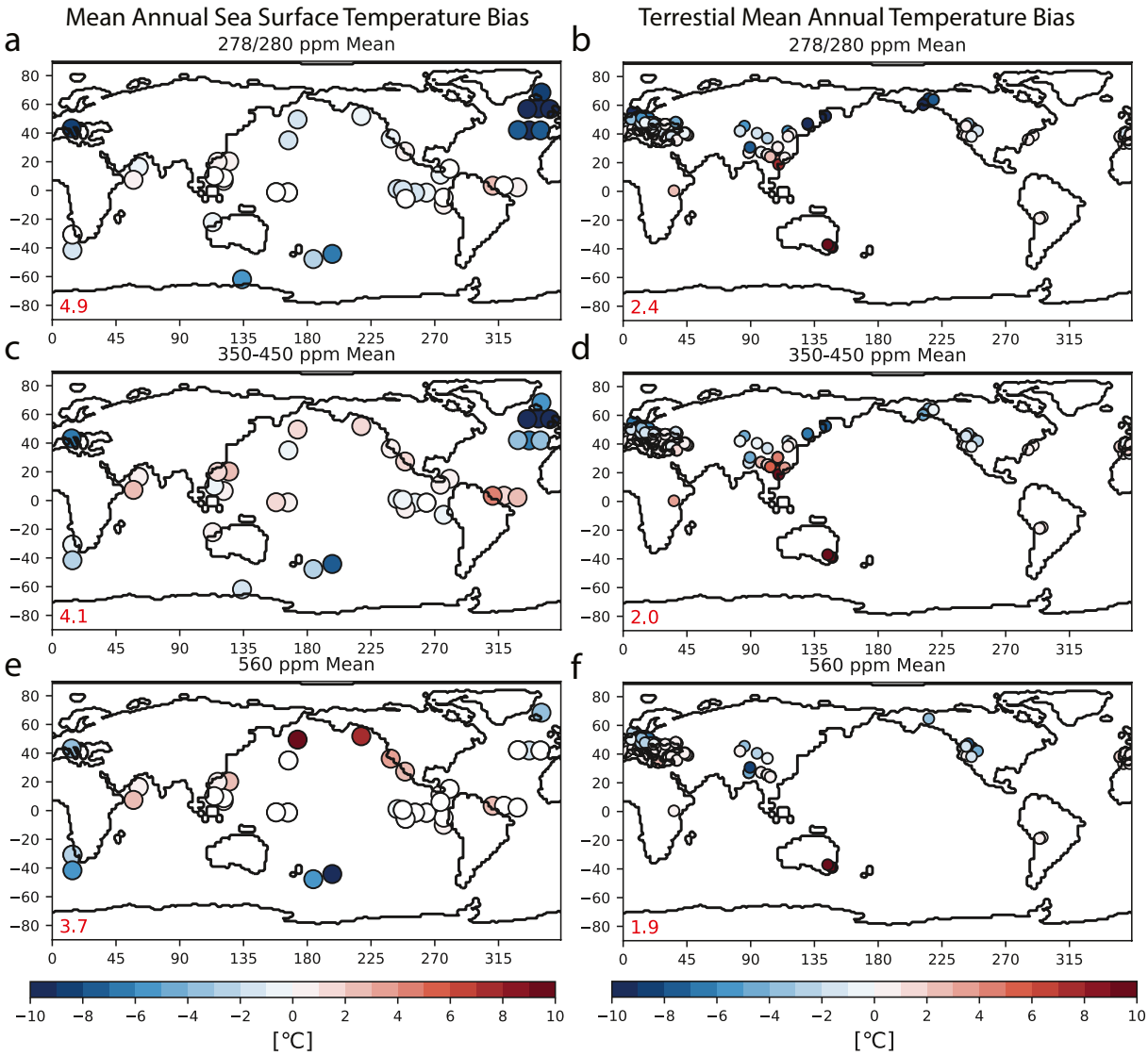

Figure 13. Late Miocene multi-model-mean (left) sea surface, (right) terrestrial mean annual temperature bias. The average of individual model bias at each site (Figures S8 and S9) is calculated across the set of Late Miocene experiments with (a and b) 278 or 280 ppm, (c and d) 350–450 ppm, (e and f) 560 ppm, and (g and h) 840/850 ppm. The root-mean-square error across all the sites is shown in red on the bottom left. The continental outline from COSMOS T31 (Knorr et al., 2011) has been used.

the subtropics to midlatitudes (Figures 4c, 11 and 12). Increasing CO_2 levels brings extra-tropical warmth into better alignment with the proxy data but the models still fall short (Figures 11 and 12), particularly on the regional scale, for example, cold SST biases persist in the North Atlantic and Southern Ocean even at 850 ppm (Figure 14g). Both the tropical Middle Miocene SST proxies and the tropical Middle Miocene terrestrial proxies indicate that 850 ppm of CO_2 leads to too much tropical warming (Figures 14g and 14h). That said, all the simulations with lower CO_2 concentrations generally suffer from cold biases everywhere outside of the tropics (Figures 14 and S11), supporting the conclusion that the models are generally failing to capture the weakening of meridional surface temperature gradients and the full extent of Middle Miocene warmth seen in the proxy data (Figure 4). This finding holds and intensifies when one narrows the data window to the MCO (Figure S12).

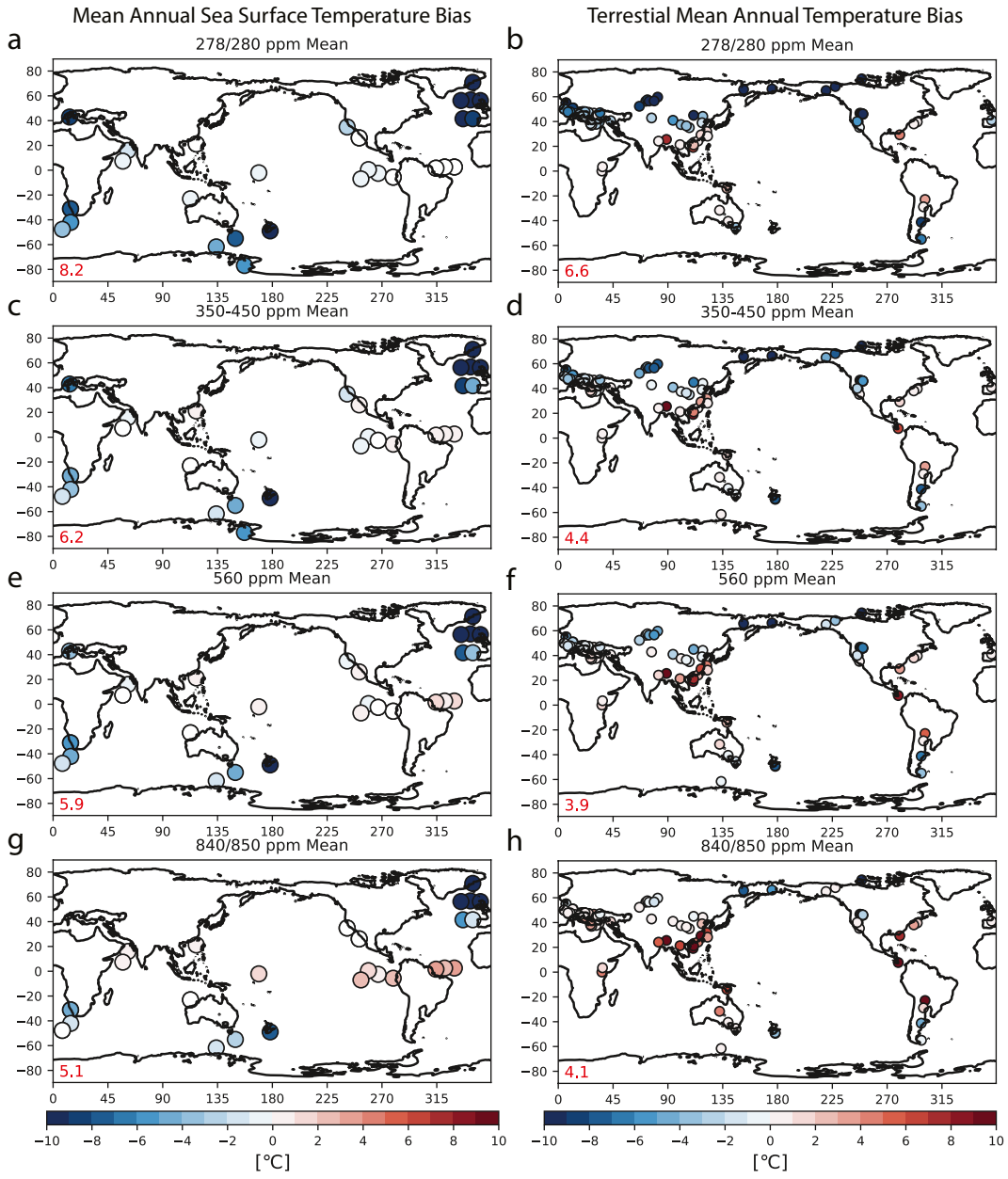

Figure 14. Middle Miocene multi-model-mean (left) sea surface, (right) terrestrial mean annual temperature bias. The average of individual model bias at each site (Figures S10 and S11) is calculated across the set of Middle to Early Miocene experiments with (a and b) 278 or 280 ppm, (c and d) 350–450 ppm, (e and f) 560 ppm, and (g and h) 840/850 ppm. The root-mean-square error across all the sites is shown in red on the bottom left. The continental outline from the updated Herold, Huber, and Müller (2011) paleogeographic boundary conditions described in this article has been used (see supporting information).

5. Conclusions

In this study, we have brought together a suite of Miocene climate simulations performed with a range of climate models and Late to Early Miocene boundary conditions. Serving as a first pass of this multi-model ensemble data set, the focus has been placed on surface warming, specifically the spread and sensitivity of warming responses to the range of boundary conditions imposed across the ensemble. Furthermore, a model-data comparison has been performed to assess the fidelity with which the ensemble is capturing large-scale Miocene warming patterns over both land and ocean, and to develop insight into how high CO_2

concentrations need to be from a modeling perspective to reproduce the broad warming patterns, specifically the weak meridional temperature gradient patterns seen in the data.

Summarizing first the key features emanating from our analysis of the global-mean, zonal-mean, and two-dimensional surface warming seen across the ensemble:

- Prescribed CO_2 forcing is the primary boundary condition controlling the global mean temperature change relative to preindustrial across the Miocene simulations analyzed
- On average, Miocene boundary conditions other than CO_2 raise global mean temperature by just under 2°C
- Reconstructed global mean surface temperature estimates range from 19.30°C ± 0.98°C to 21.95°C ± 0.81°C for the Late Miocene, from 21.21°C ± 0.56°C to 24.46°C ± 0.81°C for the Middle Miocene, and from 22.93°C ± 1.01°C to 25.47°C ± 1.17°C for the MOC, depending on the type of surface temperature proxy informing the estimate
- While some Miocene simulations with ≥400 ppm CO_2 forcing overlap with the minimum bound of the reconstructed global mean surface temperature estimates for their target Miocene interval, they generally fail to capture the reconstructed warming pattern. No combination of model and boundary condition choices to date satisfactorily simulates Miocene climate
- A stronger polar greenhouse effect and decreased surface albedo are the dominant contributors to the polar amplified warming
- Strong regional warming is seen in response to prescribed changes in the Antarctic Ice Sheet but the influence beyond the Southern Hemisphere high latitudes is limited
- The degree of polar amplified warming and weakening of the meridional temperature gradient increases with prescribed CO_2 forcing, but generally falls short of the reconstructed meridional gradient weakening seen in the proxies
- "Hot spots" in which the SST response within a narrow range of CO_2 forcings is particularly variable across models including the eastern equatorial upwelling regions, the subpolar gyres, and the Southern Ocean, and appear to be linked to the spread in cloud albedo and ocean responses in these regions
- Simulations with perturbed orbital parameters show important, yet relatively small and regional, surface temperature sensitivity with an increased sensitivity to orbital changes as CO_2 concentrations, or the extent of the Antarctic Ice Sheet, decrease

The extent to which the Miocene surface temperatures within the ensemble align with available terrestrial and SST reconstructions have been assessed. Broadly speaking, the low meridional temperature gradient indicated by the proxies, specifically between the mid-latitudes and tropics, is difficult to reconcile with the simulations. Under Miocene-like CO_2 forcing (the 350–450 ppm experiments), the modeled climates still retain relatively large equator-to-pole temperature gradients, especially in the Northern Hemisphere. The models do not exhibit the estimated 5°C–10℃ warming of the high latitudes with these CO_2 levels. In practice, this means that to produce realistic warming of the northern high-latitudes, the models require higher CO_2. Increasing CO_2 forcing leads to enhanced warming bringing the midlatitudes into better alignments with the data, but this in turn leads to overshooting in the tropics that become too warm. This pattern is surprisingly robust across both the Late Miocene, Middle Miocene, and MCO data sets, as well as the independent terrestrial and ocean data sets. Achieving the low meridional temperature gradient recorded in the Miocene thus remains an outstanding problem for most models.

That said, the latest generation of climate models with state-of-the-art parameterizations of cloud microphysics and cloud-aerosol interactions tend to support more positive cloud radiative feedbacks of the midlatitude oceans (Lunt et al., 2020; Zhu et al., 2019; Zhu & Poulsen, 2019). In addition, changes in aerosols may also be important as seen for the Eocene (Lunt et al., 2020) and Pliocene (Feng et al., 2019; Sagoo & Storelvmo, 2017). These model improvements may lead to enhanced midlatitude warming at lower CO_2 concentrations, but how they will then fare at simulating tropical Miocene warmth and the reduced meridional temperature gradient remains to be evaluated. More idealized sensitivity studies have revealed that both the meridional and the zonal equatorial Pacific SST gradients scale with the meridional gradient in cloud radiative forcing (specifically cloud albedo, Burls & Fedorov, 2014a, 2014b; Erfani & Burls, 2019), and provide a plausible mechanism for maintaining Early Pliocene SST patterns (Burls & Fedorov, 2014a, 2014b; Fedorov et al., 2015) and the hydrological cycle response (Burls & Fedorov, 2017).

The model ensemble we have used here was an "post-hoc" model intercomparison using different boundary conditions and forcings for each model. Although we can still group the models into two timeframes (Early Middle and Late Miocene) and into different CO_2 forcing ranges, it is impossible to cleanly assess how much of the inter-model spread can be attributed to differences in boundary conditions versus model feedback strengths. In particular, even if we could assign one simulation as a good match with the proxies, the reasons for this better match would not necessarily be clear. Therefore, to more rigorously test the models' ability to simulate Miocene warmth, meridional gradients, and other features such as ocean circulation, cloud feedbacks, land surface behavior, and the hydrological cycle, carrying out a formal MIP is desirable.

The current study can guide a discussion on the careful design of the boundary conditions and model configurations to be used in such a formal model intercomparison.

I. In terms of paleogeography, the modeling groups participating in a formal MIP should use the same configuration for each model, and specific time slices (e.g., the MCO) should be chosen.
II. A common set of prescribed ice sheet boundary conditions that sample the uncertainty in reconstructed estimate should be used.
III. Sensitivity studies isolating the impact of gateway changes can then be encouraged by providing alternative continental geometries exploring different depths and widths of gateways based on minimum/maximum estimates from plate tectonic reconstructions. Key gateways to be investigated include the Central American Seaway, the Tethys Seaway, the Indonesian Seaway, the Fram Strait as well as the Greenland-Scotland Ridge and Canadian archipelago. More detailed discussions about these gateway conditions can be found in He et al. (this issue) and Brierley and Fedorov (2016).
IV. Models should be grouped into those with static or dynamic vegetation, and all models with static vegetation should use the same static vegetation distributions. Using a dynamic vegetation model is optimal as this allows for more direct comparison with vegetation cover indicated by the fossil flora record, for example, Henrot et al. (2017). Care needs to be taken to ensure that plant functional types are appropriate for the Miocene.
V. Ideally, all models would treat aerosols in the same way, but if this is not feasible, differences should at least be well-documented (e.g., the PlioMIP2 protocol, Haywood et al. [2016], and DeepMIP protocol, Lunt et al. [2017]).
VI. Finally, simulation should be run with a set of CO_2 concentrations that span the spread of uncertainty within Miocene CO_2 reconstructions. With the "best estimate" CO_2 concentration specified for when modeling groups can only carry out one simulation.

While a coordinated Miocene model intercomparison effort is an aspiration within the Miocene community, the analysis of the informal multi-model ensemble presented here has focused only on annual mean surface temperature and albedo responses and there remain several other aspects within this valuable data set for investigation in future study, for example, the hydrological cycle, subsurface ocean temperature, and circulation, differences in seasonality, and so on. We hope that the synthesis presented here will serve as a valuable starting point. We plan on describing updates and future community efforts on the DeepMIP Miocene website—https://www.deepmip.org/deepmip-miocene/.

Data Availability Statement

The new synthesis of terrestrial MATs generated here for the Middle Miocene can be found in the supporting information of this study (additional excel file Table S1). As described in Section 3 of the study, the Late, Middle and MCO SST estimates where compiled using published data sets, a summary of these data sets with links to their repositories has been complied in the supporting information, together with the average estimates derived from each data set for each time period (additional excel file Table S2). This effort to synthesis available Miocene SST will be continually updated as part of the Miocene Temperature Portal (https://bolin.su.se/data/miocene-temperature-portal) hosted at Stockholm University. These Tables S1 and S2 excel files have been archived in the Zenodo repository https://doi.org/10.5281/zenodo.4568897 together with NetCDF files containing the updated Middle Miocene paleogeography and land surface data sets described in supporting information, and a NetCDF file containing the MioMIP variables used to make all the figures shown. The code used to make the figures is available on GitHub (https://github.com/nburls/MioMIP1). A description of each model's setup is provided in Section 3 of this study, together with the relevant configuration information and reference to the original modeling study in Tables 1 and 2.

Acknowledgments
N. J. Burls acknowledges the support from the National Science Foundation (NSF; AGS-1844380 and OCN-2002448), as well as the Alfred P. Sloan Foundation as a Research Fellow. A. M. De Boer acknowledges the support of the Swedish Research Council Project 2016-03912. A. S. von der Heydt acknowledges the support by the program of the Netherlands Earth System Science Center (NESSC), financially supported by the Ministry of Education, Culture and Science (OCW) (Grant no. 024.002.001). D. K. Hutchinson acknowledges the support of FORMAS Grant 2018-01621. C. D. Bradshaw acknowledges NERC Grant NE I006281/1 and a NERC PhD studentship. C. H. Lear acknowledges NERC Grant NE/P019102/1. D. J. Lunt and A. Farnsworth acknowledge NERC Grant NE/K014757/1. M. Huber and N. Herold acknowledge funding from the NSF P2C2 program for this project through Grant #1602905. E. Gasson acknowledges funding from the Royal Society and NERC Grant NE/T007397/1. The authors thank S. Sosdian, S. Modestou, and F. Sangiorgi for assistance in compiling the ocean temperature data.

References

Anand, P., Elderfield, H., & Conte, M. H. (2003). Calibration of Mg/Ca thermometry in planktonic foraminifera from a sediment trap time series. *Paleoceanography*, *18*(2). https://doi.org/10.1029/2002pa000846

Aumont, O., Ethé, C., Tagliabue, A., Bopp, L., & Gehlen, M. (2015). PISCES-v2: An ocean biogeochemical model for carbon and ecosystem studies. *Geoscientific Model Development*, *8*, 2465–2513. https://doi.org/10.5194/gmd-8-2465-2015

Bacmeister, J. T., Lauritzen, P. H., Dai, A., & Truesdale, J. E. (2012). Assessing possible dynamical effects of condensate in high resolution climate simulations. *Geophysical Research Letters*, *39*(4), L04806. https://doi.org/10.1029/2011gl050533

Bartoli, G., Sarnthein, M., Weinelt, M., Erlenkeuser, H., Garbe-Schönberg, D., & Lea, D. W. (2005). Final closure of Panama and the onset of northern hemisphere glaciation. *Earth and Planetary Science Letters*, *237*(1–2), 33–44. https://doi.org/10.1016/j.epsl.2005.06.020

Bentsen, M., Bethke, I., Debernard, J. B., Iversen, T., Kirkevåg, A., Seland, Ø., et al. (2013). The Norwegian Earth System Model, NorESM1-M – Part 1: Description and basic evaluation of the physical climate. *Geoscientific Model Development*, *6*, 687–720. https://doi.org/10.5194/gmd-6-687-2013

Bitz, C. M., Shell, K. M., Gent, P. R., Bailey, D. A., Danabasoglu, G., Armour, K. C., et al. (2012). Climate sensitivity of the Community Climate System Model, Version 4. *Journal of Climate*, *25*, 3053–3070. https://doi.org/10.1175/JCLI-D-11-00290.1

Bradshaw, C. D., Langebroek, P. M., Lear, C. H., Lunt, D. J., Coxall, H. K., Sosdian, S. M., & de Boer, A.M. (2021). Hydrological impact of Middle Miocene Antarctic ice-free areas coupled to deep ocean temperatures. *Nature Geoscience*, In press.

Bradshaw, C. D., Lunt, D., Flecker, R., Salzmann, U., Pound, M., Haywood, A., & Eronen, J. (2012). The relative roles of CO_2 and palaeogeography in determining late Miocene climate: Results from a terrestrial model-data comparison. *Climate of the Past*, *8*(2), 715–786. https://doi.org/10.5194/cp-8-1257-2012

Bradshaw, C. D., Lunt, D. J., Flecker, R., & Davies-Barnard, T. (2015). Disentangling the roles of late Miocene palaeogeography and vegetation: Implications for climate sensitivity. *Palaeogeography, Palaeoclimatology, Palaeoecology*, *417*, 17–34. https://doi.org/10.1016/j.palaeo.2014.10.003

Bretherton, C. S., & Park, S. (2009). A new moist turbulence parameterization in the Community Atmosphere Model. *Journal of Climate*, *22*(12), 3422–3448. https://doi.org/10.1175/2008jcli2556.1

Brierley, C. M., & Fedorov, A. V. (2016). Comparing the impacts of Miocene-Pliocene changes in inter-ocean gateways on climate: Central American Seaway, Bering Strait, and Indonesia. *Earth and Planetary Science Letters*, *444*, 116–130. https://doi.org/10.1016/j.epsl.2016.03.010

Brovkin, V., Raddatz, T., Reick, C., Claussen, M., & Gayler, V. (2009). Global biogeophysical interactions between forest and climate. *Geophysical Research Letters*, *36*, L07405. https://doi.org/10.1029/2009gl037543

Burke, K. D., Williams, J. W., Chandler, M. A., Haywood, A. M., Lunt, D. J., & Otto-Bliesner, B. L. (2018). Pliocene and Eocene provide best analogs for near-future climates. *Proceedings of the National Academy of Sciences of the United States of America*, *115*, 13288–13293. https://doi.org/10.1073/pnas.1809600115

Burls, N. J., & Fedorov, A. V. (2014a). Simulating Pliocene warmth and a permanent El Niño-like state: The role of cloud albedo. *Paleoceanography*, *29*(10), 893–910. https://doi.org/10.1002/2014PA002644

Burls, N. J., & Fedorov, A. V. (2014b). What controls the Mean East-West Sea surface temperature gradient in the Equatorial Pacific: The role of cloud albedo. *Journal of Climate*, *27*(7), 2757–2778. https://doi.org/10.1175/JCLI-D-13-00255.1

Burls, N. J., & Fedorov, A. V. (2017). Wetter subtropics in a warmer world: Contrasting past and future hydrological cycles. *Proceedings of the National Academy of Sciences of the United States of America*, *114*(49), 12888–12893. https://doi.org/10.1073/pnas.1703421114

Burton, K. W., Ling, H.-F., & O'Nions, R. K. (1997). Closure of the Central American Isthmus and its effect on deep-water formation in the North Atlantic. *Nature*, *386*(6623), 382–385. https://doi.org/10.1038/386382a0

Ceppi, P., Zelinka, M. D., & Hartmann, D. L. (2014). The response of the Southern Hemispheric eddy-driven jet to future changes in shortwave radiation in CMIP5. *Geophysical Research Letters*, *41*(9), 3244–3250. https://doi.org/10.1002/2014gl060043

Chandan, D., & Peltier, W. R. (2018). On the mechanisms of warming the mid-Pliocene and the inference of a hierarchy of climate sensitivities with relevance to the understanding of climate futures. *Climate of the Past*, *14*, 825–856. https://doi.org/10.5194/cp-14-825-2018

Conte, M. H., Sicre, M. A., Ruhlemann, C., Weber, J. C., Schulte, S., Schulz-Bull, D., & Blanz, T. (2006). Global temperature calibration of the alkenone unsaturation index (UK'_{37}) in surface waters and comparison with surface sediments. *Geochemistry, Geophysics, Geosystems*, *7*(1). https://doi.org/10.1029/2005GC00105410.1029/2005gc001054

Coxall, H. K., Huck, C. E., Huber, M., Lear, C. H., Legarda-Lisarri, A., O'Regan, M., et al. (2018). Export of nutrient rich Northern Component Water preceded early Oligocene Antarctic glaciation. *Nature Geosciences*, *11*(3), 190–196. https://doi.org/10.1038/s41561-018-0069-9

Dicks, A. J. (2019). Understanding Miocene climatic warmth (Thesis). Purdue University Graduate School https://doi.org/10.25394/PGS.8956736.v1

Dufresne, J.-L., Foujols, M.-A., Denvil, S., Caubel, A., Marti, O., Aumont, O., et al. (2013). Climate change projections using the IPSL-CM5 Earth System Model: From CMIP3 to CMIP5. *Climate Dynamics*, *40*(9–10), 2123–2165. https://doi.org/10.1007/s00382-012-1636-1

Eaton, B. (2010). User's guide to the community atmosphere model CAM-4.0. Retrieved from http://www.cesm.ucar.edu/models/ccsm4.0/cam/docs/users_guide/ug.html

Ehlers, B.-M., & Jokat, W. (2013). Paleo-bathymetry of the northern North Atlantic and consequences for the opening of the Fram Strait. *Marine Geophysical Researches*, *34*(1), 25–43. https://doi.org/10.1007/s11001-013-9165-9

Erfani, E., & Burls, N. J. (2019). The strength of low-cloud feedbacks and tropical climate: A CESM sensitivity study. *Journal of Climate*, *32*(9), 2497–2516. https://doi.org/10.1175/jcli-d-18-0551.1

Etminan, M., Myhre, G., Highwood, E. J., & Shine, K. P. (2016). Radiative forcing of carbon dioxide, methane, and nitrous oxide: A significant revision of the methane radiative forcing. *Geophysical Research Letters*, *43*(24), 12614–12623. https://doi.org/10.1002/2016gl071930

Farnsworth, A., Lunt, D., Robinson, S., Valdes, P., Roberts, W., Clift, P., et al. (2019). Past East Asian monsoon evolution controlled by palaeogeography, not CO_2. *Science Advances*, *5*(10), eaax1697. https://doi.org/10.1126/sciadv.aax1697

Farnsworth, A., Lunt, D. J., O'Brien, C. L., Foster, G. L., Inglis, G. N., Markwick, P., et al. (2019). Climate sensitivity on geological timescales controlled by nonlinear feedbacks and ocean circulation. *Geophysical Research Letters*, *46*, 9880–9889. https://doi.org/10.1029/2019gl083574

Fedorov, A. V., Burls, N. J., Lawrence, K. T., & Peterson, L. C. (2015). Tightly linked zonal and meridional sea surface temperature gradients over the past five million years. *Nature Geosciences*, *8*(12), 975–980. https://doi.org/10.1038/ngeo2577

Feng, R., Otto-Bliesner, B. L., Fletcher, T. L., Tabor, C. R., Ballantyne, A. P., & Brady, E. C. (2017). Amplified Late Pliocene terrestrial warmth in northern high latitudes from greater radiative forcing and closed Arctic Ocean gateways. *Earth and Planetary Science Letters*, *466*, 129–138. https://doi.org/10.1016/j.epsl.2017.03.006

Feng, R., Otto-Bliesner, B. L., Xu, Y., Brady, E., Fletcher, T., & Ballantyne, A. (2019). Contributions of aerosol-cloud interactions to mid-Piacenzian seasonally sea ice-free Arctic Ocean. *Geophysical Research Letters*, *46*. https://doi.org/10.1029/2019GL083960
Ferguson, D. K., Pingen, M., Zetter, R., & Hofmann, C.-C. (1998). Advances in our knowledge of the Miocene plant assemblage from Kreuzau, Germany. *Review of Palaeobotany and Palynology*, *101*, 147–177. https://doi.org/10.1016/s0034-6667(97)00074-2
Foster, G. L., Lear, C. H., & Rae, J. W. B. (2012). The evolution of pCO_2, ice volume and climate during the middle Miocene. *Earth and Planetary Science Letters*, *341–344*, 243–254. https://doi.org/10.1016/j.epsl.2012.06.007
Foster, G. L., Royer, D. L., & Lunt, D. J. (2017). Future climate forcing potentially without precedent in the last 420 million years. *Nature Communications*, *8*, 14845. https://doi.org/10.1038/ncomms14845
Frigola, A., Prange, M., & Schulz, M. (2018). Boundary conditions for the Middle Miocene Climate Transition (MMCT v1.0). *Geoscientific Model Development*, *11*, 1607–1626. https://doi.org/10.5194/gmd-11-1607-2018
Gasson, E., DeConto, R. M., Pollard, D., & Levy, R. H. (2016). Dynamic Antarctic ice sheet during the early to mid-Miocene. *Proceedings of the National Academy of Sciences of the United States of America*, *113*(13), 3459–3464. https://doi.org/10.1073/pnas.1516130113
Gent, P. R., Danabasoglu, G., Donner, L. J., Holland, M. M., Hunke, E. C., Jayne, S. R., et al. (2011). The Community Climate System Model Version 4. *Journal of Climate*, *24*, 4973–4991. https://doi.org/10.1175/2011JCLI4083.1
Gettelman, A., Liu, X., Ghan, S., Morrison, H., Park, S., Conley, A., et al. (2010). Global simulations of ice nucleation and ice supersaturation with an improved cloud scheme in the community atmosphere model. *Journal of Geophysical Research*, *115*(D18), D18216. https://doi.org/10.1029/2009jd013797
Gettelman, A., Morrison, H., & Ghan, S. J. (2008). A new two-moment bulk stratiform cloud microphysics scheme in the Community Atmosphere Model, Version 3 (CAM3). Part II: Single-column and global results. *Journal of Climate*, *21*(15), 3660–3679. https://doi.org/10.1175/2008jcli2116.1
Gettelman, A., Morrison, H., Santos, S., Bogenschutz, P., & Caldwell, P. M. (2015). Advanced two-moment bulk microphysics for global models. Part II: Global model solutions and aerosol-cloud interactions. *Journal of Climate*, *28*, 1288–1307. https://doi.org/10.1175/jcli-d-14-00103.1
Goldner, A., Herold, N., & Huber, M. (2014). The challenge of simulating the warmth of the mid-Miocene climatic optimum in CESM1. *Climate of the Past*, *10*(2), 523–536. https://doi.org/10.5194/cp-10-523-2014
Gough, D. O. (1981). Solar interior structure and luminosity variations. *Solar Physics*, *74*, 21–34. https://doi.org/10.1007/bf00151270
Gray, W. R., & Evans, D. (2019). Nonthermal influences on Mg/Ca in planktonic foraminifera: A review of culture studies and application to the last glacial maximum. *Paleoceanography and Paleoclimatology*, *34*(3), 306–315. https://doi.org/10.1029/2018pa003517
Grimaldi, D. A., & Triplehorn, D. M. (2008). Insects from the Upper Miocene Grubstake Formation of Alaska. *American Museum Novitates*, *3612*, 1–19.
Hall, R. (2012). Sundaland and Wallacea: Geology, plate tectonics and palaeogeography. In D. J. Gower, J. E. Richardson, B. R. Rosen, L. Rueber, & S. T. Williams, (Eds.), *Biotic evolution and environmental change in Southeast Asia* (pp. 32–78). Cambridge University Press.
Hansen, J., Sato, M., Russell, G., & Kharecha, P. (2013). Climate sensitivity, sea level and atmospheric carbon dioxide. *Philosophical Transactions of the Royal Society A: Mathematical, Physical & Engineering Sciences*, *371*, 20120294. https://doi.org/10.1098/rsta.2012.0294
Hargreaves, J. C., & Annan, J. D. (2016). Could the Pliocene constrain the equilibrium climate sensitivity? *Climate of the Past*, *12*, 1591–1599. https://doi.org/10.5194/cp-12-1591-2016
Haug, G. H., & Tiedemann, R. (1998). Effect of the formation of the Isthmus of Panama on Atlantic Ocean thermohaline circulation. *Nature*, *393*(6686), 673–676. https://doi.org/10.1038/31447
Haywood, A. M., Dowsett, H. J., Dolan, A. M., Rowley, D., Abe-Ouchi, A., Otto-Bliesner, B., et al. (2016). The Pliocene Model Intercomparison Project (PlioMIP) Phase 2: Scientific objectives and experimental design. *Climate of the Past*, *12*(3), 663–675. https://doi.org/10.5194/cp-12-663-2016
Haywood, A. M., Dowsett, H. J., Robinson, M. M., Stoll, D. K., Dolan, A. M., Lunt, D. J., et al. (2011). Pliocene Model Intercomparison Project (PlioMIP): Experimental design and boundary conditions (Experiment 2). *Geoscientific Model Development*, *4*, 571–577. https://doi.org/10.5194/gmd-4-571-2011
Haywood, A. M., Hill, D. J., Dolan, A. M., Otto-Bliesner, B. L., Bragg, F., Chan, W.-L., et al. (2013). Large-scale features of Pliocene climate: Results from the Pliocene Model Intercomparison Project. *Climate of the Past*, *9*, 191–209. https://doi.org/10.5194/cp-9-191-2013
Haywood, A. M., Tindall, J. C., Dowsett, H. J., Dolan, A. M., Foley, K. M., Hunter, S. J., et al. (2020). A return to large-scale features of Pliocene climate: The Pliocene Model Intercomparison Project Phase 2. *Climate of the Past Discussions*. *16*, 2095–2123. https://doi.org/10.5194/cp-2019-145
Heede, U. K., Fedorov, A. V., & Burls, N. J. (2020). Timescales and mechanisms for the Tropical Pacific response to global warming: A tug of war between the Ocean Thermostat and weaker Walker. *Journal of Climate*. *33*, 6101–6118. https://doi.org/10.1175/JCLI-D-19-0690.1
Heinemann, M., Jungclaus, J. H., & Marotzke, J. (2009). Warm Paleocene/Eocene climate as simulated in ECHAM5/MPI-OM. *Climate of the Past*, *5*, 785–802. https://doi.org/10.5194/cp-5-785-2009
Henrot, A.-J., Utescher, T., Erdei, B., Dury, M., Hamon, N., Ramstein, G., et al. (2017). Middle Miocene climate and vegetation models and their validation with proxy data. *Palaeogeography, Palaeoclimatology, Palaeoecology*, *467*, 95–119. https://doi.org/10.1016/j.palaeo.2016.05.026
Herbert, T. D., Lawrence, K. T., Tzanova, A., Peterson, L. C., Caballero-Gill, R., & Kelly, C. S. (2016). Late Miocene global cooling and the rise of modern ecosystems. *Nature Geosciences*, *9*(11), 843–847. https://doi.org/10.1038/ngeo2813
Herold, N., Huber, M., Greenwood, D. R., Müller, R. D., & Seton, M. (2011). Early to middle Miocene monsoon climate in Australia. *Geology*, *39*(1), 3–6. https://doi.org/10.1130/g31208.1
Herold, N., Huber, M., & Müller, R. D. (2011). Modeling the Miocene Climatic optimum. Part I: Land and atmosphere. *Journal of Climate*, *24*, 6353–6372. https://doi.org/10.1175/2011JCLI4035.1
Herold, N., Huber, M., Müller, R. D., & Seton, M. (2012). Modeling the Miocene climatic optimum: Ocean circulation. *Paleoceanography*, *27*, PA1209. https://doi.org/10.1029/2010PA002041
Herold, N., Müller, R. D., & Seton, M. (2010). Comparing early to middle Miocene terrestrial climate simulations with geological data. *Geosphere*, *6*, 952–961. https://doi.org/10.1130/ges00544.1
Herold, N., Seton, M., Müller, R. D., You, Y., & Huber, M. (2008). Middle Miocene tectonic boundary conditions for use in climate models. *Geochemistry, Geophysics. Geosystems*, *9*(10), Q10009. https://doi.org/10.1029/2008gc002046
Hill, D. J., Haywood, A. M., Lunt, D. J., Hunter, S. J., Bragg, F. J., Contoux, C., et al. (2014). Evaluating the dominant components of warming in Pliocene climate simulations. *Climate of the Past*, *10*, 79–90. https://doi.org/10.5194/cp-10-79-2014
Holland, K., Branson, O., Haynes, L. L., Hönisch, B., Allen, K. A., Russell, A. D., et al. (2020). Constraining multiple controls on planktic foraminifera Mg/Ca. *Geochimica et Cosmochimica Acta*, *273*, 116–136. https://doi.org/10.1016/j.gca.2020.01.015

Hollis, C. J., Dunkley Jones, T., Anagnostou, E., Bijl, P. K., Cramwinckel, M. J., Cui, Y., et al. (2019). The DeepMIP contribution to PMIP4: Methodologies for selection, compilation and analysis of latest Paleocene and early Eocene climate proxy data, incorporating version 0.1 of the DeepMIP database. *Geoscientific Model Development*, *12*, 3149–3206. https://doi.org/10.5194/gmd-12-3149-2019

Hoorn, C., Wesselingh, F. P., ter Steege, H., Bermudez, M. A., Mora, A., Sevink, J., et al. (2010). Amazonia through time: Andean uplift, climate change, landscape evolution, and biodiversity. *Science*, *330*(6006), 927–931. https://doi.org/10.1126/science.1194585

Hourdin, F., Grandpeix, J.-Y., Rio, C., Bony, S., Jam, A., Cheruy, F., et al. (2013). LMDZ5B: The atmospheric component of the IPSL climate model with revisited parameterizations for clouds and convection. *Climate Dynamics*, *40*(9–10), 2193–2222. https://doi.org/10.1007/s00382-012-1343-y

Huang, X., Stärz, M., Gohl, K., Knorr, G., & Lohmann, G. (2017). Impact of Weddell Sea shelf progradation on Antarctic bottom water formation during the Miocene. *Paleoceanography*, *32*, 304. https://doi.org/10.1002/2016PA002987

Huber, M. (2013). A sensitivity to history. *Nature Geoscience*, *6*(1), 15–16.

Huber, M., & Caballero, R. (2011). The early Eocene equable climate problem revisited. *Climate of the Past*, *7*(2), 603–633. https://doi.org/10.5194/cp-7-603-2011

Huber, M., & Sloan, L. C. (2001). Heat transport, deep waters, and thermal gradients: Coupled simulation of an Eocene greenhouse climate. *Geophysical Research Letters*, *28*(18), 3481–3484. https://doi.org/10.1029/2001gl012943

Hutchinson, D. K., Boer, A. M. D., Coxall, H. K., Caballero, R., Nilsson, J., & Baatsen, M. (2018). Climate sensitivity and meridional overturning circulation in the late Eocene using GFDL CM2. 1. *Climate of the Past*, *14*(6), 789–810.

Iacono, M. J., Delamere, J. S., Mlawer, E. J., Shephard, M. W., Clough, S. A., & Collins, W. D. (2008). Radiative forcing by long-lived greenhouse gases: Calculations with the AER radiative transfer models. *Journal of Geophysical Research*, *113*(D13). https://doi.org/10.1029/2008jd009944

Inglis, G. N., Bragg, F., Burls, N., Evans, D., Foster, G. L., Huber, M., et al. (2020). Global mean surface temperature and climate sensitivity of the EECO, PETM and latest Paleocene. *Climate of the Past Discussions*. *16*(5), 1953–1968. https://doi.org/10.5194/cp-2019-167

Jungclaus, J. H., Keenlyside, N., Botzet, M., Haak, H., Luo, J.-J., Latif, M., et al. (2006). Ocean circulation and tropical variability in the coupled model ECHAM5/MPI-OM. *Journal of Climate*, *19*, 3952–3972. https://doi.org/10.1175/jcli3827.1

Kiehl, J. T., & Shields, C. A. (2001). Sensitivity of the Palaeocene-Eocene thermal maximum climate to cloud properties. *Philosophical Transactions of the Royal Society A: Mathematical, Physical & Engineering Science*, *371*, 20130093. https://doi.org/10.1098/rsta.2013.0093

Knorr, G., Butzin, M., Micheels, A., & Lohmann, G. (2011). A warm Miocene climate at low atmospheric CO_2 levels. *Geophysical Research Letters*, *38*(20). https://doi.org/10.1029/2011GL048873

Knorr, G., Butzin, M., Micheels, A., & Lohmann, G. (2019). Late Miocene model boundary conditions. PANGAEA. https://doi.org/10.1594/PANGAEA.904264

Knorr, G., & Lohmann, G. (2014). Climate warming during Antarctic ice sheet expansion at the Middle Miocene transition. *Nature Geosciences*, *7*(5), 376–381. https://doi.org/10.1038/ngeo2119

Kociuba, G., & Power, S. B. (2015). Inability of CMIP5 models to simulate recent strengthening of the Walker circulation: Implications for projections. *Journal of Climate*, *28*(1), 20–35. https://doi.org/10.1175/jcli-d-13-00752.1

Krapp, M., & Jungclaus, J. H. (2011). The Middle Miocene climate as modelled in an atmosphere-ocean-biosphere model. *Climate of the Past*, *7*, 1169–1188. https://doi.org/10.5194/cp-7-1169-2011

Krinner, G., Viovy, N., de Noblet-Ducoudré, N., Ogée, J., Polcher, J., Friedlingstein, P., et al. (2005). A dynamic global vegetation model for studies of the coupled atmosphere-biosphere system. *Global Biogeochemical Cycles*, *19*(1). https://doi.org/10.1029/2003GB002199

Kutzbach, J. E., Prell, W. L., & Ruddiman, W. F. (1993). Sensitivity of Eurasian climate to surface uplift of the Tibetan Plateau. *The Journal of Geology*, *101*(2), 177–190. https://doi.org/10.1086/648215

LaRiviere, J. P., Ravelo, A. C., Crimmins, A., Dekens, P. S., Ford, H. L., Lyle, M., & Wara, M. W. (2012). Late Miocene decoupling of oceanic warmth and atmospheric carbon dioxide forcing. *Nature*, *486*, 97–100. https://doi.org/10.1038/nature11200

Lawrence, K. T., Herbert, T. D., Dekens, P. S., & Ravelo, A. C. (2007). The application of the alkenone organic proxy to the study of Plio-Pleistocene climate. In *Deep-time perspectives on climate change: Marrying the signal from computer models and biological*, 539–562. Geological Society of London.

Lear, C. H., Coxall, H. K., Foster, G. L., Lunt, D. J., Mawbey, E. M., Rosenthal, Y., et al. (2015). Neogene ice volume and ocean temperatures: Insights from infaunal foraminiferal Mg/Ca paleothermometry. *Paleoceanography 30*(11), 1437–1454. https://doi.or10.1002/2015PA002833

Lear, C. H., Elderfield, H., & Wilson, P. A. (2000). Cenozoic deep-sea temperatures and global ice volumes from Mg/Ca in benthic foraminiferal calcite. *Science*, *287*(5451), 269–272. https://doi.org/10.1126/science.287.5451.269

Lear, C. H., Rosenthal, Y., & Wright, J. D. (2003). The closing of a seaway: Ocean water masses and global climate change. *Earth and Planetary Science Letters*, *210*(3–4), 425–436. https://doi.org/10.1016/s0012-821x(03)00164-x

Ling, H. F., Burton, K. W., O'Nions, R. K., Kamber, B. S., von Blanckenburg, F., Gibb, A. J., & Hein, J. R. (1997). Evolution of Nd and Pb isotopes in Central Pacific seawater from ferromanganese crusts. *Earth and Planetary Science Letters*, *146*(1–2), 1–12. https://doi.org/10.1016/s0012-821x(96)00224-5

Liu, X., Easter, R. C., Ghan, S. J., Zaveri, R., Rasch, P., Shi, X., et al. (2012). Toward a minimal representation of aerosols in climate models: Description and evaluation in the Community Atmosphere Model CAM5. *Geoscientific Model Development*, *5*, 709–739. https://doi.org/10.5194/gmd-5-709-2012

Lopes dos Santos, R. A., Prange, M., Castañeda, I. S., Schefuß, E., Mulitza, S., Schulz, M., et al. (2010). Glacial-interglacial variability in Atlantic meridional overturning circulation and thermocline adjustments in the tropical North Atlantic. *Earth and Planetary Science Letters*, *300*, 407–414. https://doi.org/10.1016/j.epsl.2010.10.030

Lunt, D. J., Bragg, F., Chan, W.-L., Hutchinson, D. K., Ladant, J.-B., Niezgodzki, I., et al. (2020). DeepMIP: Model intercomparison of early Eocene climatic optimum (EECO) large-scale climate features and comparison with proxy data. *Climate of the Past Discussions*. *17*, 203–227. https://doi.org/10.5194/cp-2019-149

Lunt, D. J., Dunkley Jones, T., Heinemann, M., Huber, M., LeGrande, A., Winguth, A., et al. (2012). A model-data comparison for a multi-model ensemble of early Eocene atmosphere-ocean simulations: EoMIP. *Climate of the Past*, *8*(5), 1717–1736. https://doi.org/10.5194/cp-8-1717-2012

Lunt, D. J., Haywood, A. M., Schmidt, G. A., Salzmann, U., Valdes, P. J., & Dowsett, H. J. (2010). Earth system sensitivity inferred from Pliocene modelling and data. *Nature Geoscience*, *3*(1), 60–64.

Lunt, D. J., Haywood, A. M., Schmidt, G. A., Salzmann, U., Valdes, P. J., Dowsett, H. J., & Loptson, C. A. (2012). On the causes of mid-Pliocene warmth and polar amplification. *Earth and Planetary Science Letters*, *321–322*, 128–138. https://doi.org/10.1016/j.epsl.2011.12.042

Lunt, D. J., Huber, M., Anagnostou, E., Baatsen, M. L. J., Caballero, R., DeConto, R., et al. (2017). The DeepMIP contribution to PMIP4: Experimental design for model simulations of the EECO, PETM, and pre-PETM (version 1.0). *Geoscientific Model Development*, *10*(2), 889–901. https://doi.org/10.5194/gmd-10-889-2017

Lunt, D. J., Valdes, P. J., Haywood, A., & Rutt, I. C. (2008). Closure of the Panama Seaway during the Pliocene: Implications for climate and Northern Hemisphere glaciation. *Climate Dynamics*, *30*(1), 1–18.

Madec, G. (2008). NEMO ocean engine (Technical note). IPSL. Retrieved from https://www.nemo-ocean.eu/content/download/11245/56055/file/NEMO_book_v3_2.pdf

Madec, G., & Imbard, M. (1996). A global ocean mesh to overcome the North Pole singularity. *Climate Dynamics*, *12*(6), 381–388. https://doi.org/10.1007/BF00211684

Maier-Reimer, E., Mikolajewicz, U., & Crowley, T. (1990). Ocean general circulation model sensitivity experiment with an open Central American Isthmus. *Paleoceanography*, *5*(3), 349–366. https://doi.org/10.1029/pa005i003p00349

Markwick, P. J. (2007). Deep time perspectives on climate change: Marrying the signal from computer models and biological proxies. In M. Williams, A. M. Haywood, F. J. Gregory, & D. N. Schmidt, (Eds.), *The palaeogeographic and paleoclimatic significance of climate proxies for data-model comparisons)*. The Micropalaeontological Society Special Publications, Geological Society of London.

Markwick, P. J., & Valdes, P. J. (2004). Palaeo-digital elevation models for use as boundary conditions in coupled ocean–atmosphere GCM experiments: A Maastrichtian (late Cretaceous) example. *Palaeogeography, Palaeoclimatology, Palaeoecology*, *213*(1–2), 37–63.

Marsland, S. J., Haak, H., Jungclaus, J. H., Latif, M., & Röske, F. (2003). The Max-Planck-Institute global ocean/sea ice model with orthogonal curvilinear coordinates. *Ocean Modelling*, *5*, 91–127. https://doi.org/10.1016/s1463-5003(02)00015-x

Marzocchi, A., Flecker, R., Lunt, D. J., Krijgsman, W., & Hilgen, F. J. (2019). Precessional drivers of late Miocene Mediterranean sedimentary sequences: African summer monsoon and Atlantic winter storm tracks. *Paleoceanography and Paleoclimatology*, *34*, 1980–1994. https://doi.org/10.1029/2019pa003721

Marzocchi, A., Flecker, R., Van Baak, C. G., Lunt, D. J., & Krijgsman, W. (2016). Mediterranean outflow pump: An alternative mechanism for the Lago-mare and the end of the Messinian Salinity Crisis. *Geology*, *44*(7), 523–526.

Marzocchi, A., Lunt, D. J., Flecker, R., Bradshaw, C. D., Farnsworth, A., & Hilgen, F. J. (2015). Orbital control on late Miocene climate and the North African monsoon: Insight from an ensemble of sub-precessional simulations. *Climate of the Past*, *11*, 1271–1295. https://doi.org/10.5194/cp-11-1271-2015

McClymont, E. L., Ford, H. L., Ho, S. L., Tindall, J. C., Haywood, A. M., Alonso-Garcia, M., et al. (2020). Lessons from a high-CO_2 world: An ocean view from ~3 million years ago. *Climate of the Past*, *16*, 1599–1615. https://doi.org/10.5194/cp-16-1599-2020

Micheels, A., Bruch, A. A., Eronen, J., Fortelius, M., Harzhauser, M., Utescher, T., & Mosbrugger, V. (2011). Analysis of heat transport mechanisms from a Late Miocene model experiment with a fully-coupled atmosphere–ocean general circulation model. *Palaeogeography, Palaeoclimatology, Palaeoecology*, *304*(3–4), 337–350. https://doi.org/10.1016/j.palaeo.2010.09.021

Micheels, A., Bruch, A. A., Uhl, D., Utescher, T., & Mosbrugger, V. (2007). A Late Miocene climate model simulation with ECHAM4/ML and its quantitative validation with terrestrial proxy data. *Palaeogeography, Palaeoclimatology, Palaeoecology*, *253*, 267–286. https://doi.org/10.1016/j.palaeo.2007.03.042

Mikolajewicz, U., Maier-Reimer, E., Crowley, T. J., & Kim, K.-Y. (1993). Effect of Drake and Panamanian gateways on the circulation of an ocean model. *Paleoceanography*, *8*(4), 409–426. https://doi.org/10.1029/93pa00893

Montes, C., Cardona, A., McFadden, R., Morón, S. E., Silva, C. A., Restrepo-Moreno, S., et al. (2012). Evidence for middle Eocene and younger land emergence in central Panama: Implications for Isthmus closure. *GSA Bulletin*, *124*(5–6), 780–799. https://doi.org/10.1130/b30528.1

Morley, R. J. (2011). Cretaceous and Tertiary climate change and the past distribution of megathermal rainforests. In: M. Bush, J. Flenley & W. Gosling (Eds.), (pp. 1–34). Berlin, Heidelberg: Springer Praxis Books.

Mosbrugger, & Utescher, T. (1997). The coexistence approach—a method for quantitative reconstructions of Tertiary terrestrial palaeoclimate data using plant fossils. *Palaeogeography, Palaeoclimatology, Palaeoecology*, *134*(1–4), 61–86. https://doi.org/10.1016/s0031-0182(96)00154-x

Müller, P. J., Kirst, G., Ruhland, G., von Storch, I., & Rosell-Melé, A. (1998). Calibration of the alkenone paleotemperature index U37K′ on core-tops from the eastern South Atlantic and the global ocean (60°N–60°S). *Geochimica et Cosmochimica Acta*, *62*, 1757–1772.

Neale, R. B., Chen, C.-C., Gettelman, A., Lauritzen, P. H., Park, S, Williamson, D. L., Conley, A. J., et al. (2010). Description of the NCAR Community Atmosphere Model (CAM5.0) (Technical Note). NCAR. NCAR/TN-486-STR:268.

Neale, R. B., Richter, J., Park, S., Lauritzen, P. H., Vavrus, S. J., Rasch, P. J., & Zhang, M. (2013). The mean climate of the Community Atmosphere Model (CAM4) in forced SST and fully coupled experiments. *Journal of Climate*, *26*, 5150–5168. https://doi.org/10.1175/jcli-d-12-00236.1

O'Dea, A., Lessios, H. A., Coates, A. G., Eytan, R. I., Restrepo-Moreno, S. A., Cione, A. L., et al. (2016). Formation of the Isthmus of Panama. *Science Advances*, *2*(8), e1600883.

Omta, A. W., & Dijkstra, H. A. (2003). A physical mechanism for the Atlantic-Pacific flow reversal in the early Miocene. *Global and Planetary Change*, *36*, 265–276. https://doi.org/10.1016/s0921-8181(02)00221-7

Otto-Bliesner, B. L., Jahn, A., Feng, R., Brady, E. C., Hu, A., & Löfverström, M. (2017). Amplified North Atlantic warming in the late Pliocene by changes in Arctic gateways. *Geophysical Research Letters*, *44*, 957–964.

Pithan, F., & Mauritsen, T. (2014). Arctic amplification dominated by temperature feedbacks in contemporary climate models. *Nature Geosciences*, *7*, 181–184. https://doi.org/10.1038/ngeo2071

Pound, M. J., Haywood, A. M., Salzmann, U., & Riding, J. B. (2012). Global vegetation dynamics and latitudinal temperature gradients during the Mid to Late Miocene (15.97–5.33 Ma). *Earth-Science Reviews*, *112*(1–2), 22. https://doi.org/10.1016/j.earscirev.2012.02.005

Pound, M. J., & Salzmann, U. (2017). Heterogeneity in global vegetation and terrestrial climate change during the late Eocene to early Oligocene transition. *Scientific Reports*, *7*, 43386. https://doi.org/10.1038/srep43386

Raddatz, T. J., Reick, C. H., Knorr, W., Kattge, J., Roeckner, E., Schnur, R., et al. (2007). Will the tropical land biosphere dominate the climate-carbon cycle feedback during the twenty-first century? *Climate Dynamics*, *29*, 565–574. https://doi.org/10.1007/s00382-007-0247-8

Renoult, M., Annan, J. D., Hargreaves, J. C., Sagoo, N., Flynn, C., Kapsch, M.-L., et al. (2020). A Bayesian framework for emergent constraints: Case studies of climate sensitivity with PMIP. *Climate of the Past*, *16*, 1715–1735. https://doi.org/10.5194/cp-16-1715-2020

Roeckner, E., Bäuml, G., Bonaventura, L., Brokopf, R., Esch, M., Giorgetta, M., et al. (2003). The atmospheric general circulation model ECHAM5, Part I: Model description. Report No. 349., Max-Planck-Institut für Meteorologie.

Ruddiman, W. F., & Kutzbach, J. E. (1989). Forcing of late Cenozoic northern hemisphere climate by plateau uplift in southern Asia and the American west. *Journal of Geophysical Research*, *94*(D15), 18409–18427. https://doi.org/10.1029/JD094iD15p1840s9

Sagoo, N., & Storelvmo, T. (2017). Testing the sensitivity of past climates to the indirect effects of dust. *Geophysical Research Letters*, *44*, 5807–5817. https://doi.org/10.1002/2017gl072584

Sagoo, N., Valdes, P., Flecker, R., & Gregoire, L. J. (2013). The Early Eocene equable climate problem: Can perturbations of climate model parameters identify possible solutions? *Philosophical Transactions of the Royal Society A: Mathematical, Physical & Engineering Sciences*, *371*, 20130123. https://doi.org/10.1098/rsta.2013.0123

Sangiorgi, F., Bijl, P. K., Passchier, S., Salzmann, U., Schouten, S., McKay, R., et al. (2018). Southern Ocean warming and Wilkes Land ice sheet retreat during the mid-Miocene. *Nature Communications*, *9*(1), 317. https://doi.org/10.1038/s41467-017-02609-7

Sepulchre, P., Caubel, A., Ladant, J.-B., Bopp, L., Boucher, O., Braconnot, P., et al. (2020). IPSL-CM5A2 – An Earth system model designed for multi-millennial climate simulations. *Geoscientific Model Development*, *13*, 3011–3053. https://doi.org/10.5194/gmd-13-3011-2020

Shaw, T. A., Baldwin, M., Barnes, E. A., Caballero, R., Garfinkel, C. I., Hwang, Y.-T., et al. (2016). Storm track processes and the opposing influences of climate change. *Nature Geosciences*, *9*(9), 656–664. https://doi.org/10.1038/ngeo2783

Shevenell, A. E., Kennett, J. P., & Lea, D. W. (2004). Middle Miocene Southern Ocean cooling and Antarctic cryosphere expansion. *Science*, *305*(5691), 1766–1770. https://doi.org/10.1126/science.1100061

Shields, C. A., Bailey, D. A., Danabasoglu, G., Jochum, M., Kiehl, J. T., Levis, S., & Park, S. (2012). The low-resolution CCSM4. *Journal of Climate*, *25*, 3993–4014. https://doi.org/10.1175/JCLI-D-11-00260.1

Sijp, W. P., von der Heydt, A. S., Dijkstra, H. A., Flögel, S., Douglas, P. M. J., & Bijl, P. K. (2014). The role of ocean gateways on cooling climate on long time scales. *Global and Planetary Change*, *119*, 1–22. https://doi.org/10.1016/j.gloplacha.2014.04.004

Simon, D., Marzocchi, A., Flecker, R., Lunt, D. J., Hilgen, F. J., & Meijer, P. T. (2017). Quantifying the Mediterranean freshwater budget throughout the late Miocene: New implications for sapropel formation and the Messinian Salinity Crisis. *Earth and Planetary Science Letters*, *472*, 25–37. https://doi.org/10.1016/j.epsl.2017.05.013

Sosdian, S. M., Babila, T. L., Greenop, R., Foster, G. L., & Lear, C. H. (2020). Ocean Carbon Storage across the middle Miocene: A new interpretation for the Monterey Event. *Nature Communications*, *11*(1), 1–11. https://doi.org/10.1038/s41467-019-13792-0

Sosdian, S. M., Greenop, R., Hain, M. P., Foster, G. L., Pearson, P. N., & Lear, C. H. (2018). Constraining the evolution of Neogene ocean carbonate chemistry using the boron isotope pH proxy. *Earth and Planetary Science Letters*, *498*, 362–376. https://doi.org/10.1016/j.epsl.2018.06.017

Stärz, M., Jokat, W., Knorr, G., & Lohmann, G. (2017). Threshold in North Atlantic-Arctic Ocean circulation controlled by the subsidence of the Greenland-Scotland Ridge. *Nature Communications*, *8(1)*, 15681. https://doi.org/10.1038/ncomms15681

Stein, R., Fahl, K., Schreck, M., Knorr, G., Niessen, F., Forwick, M., et al. (2016). Evidence for ice-free summers in the late Miocene central Arctic Ocean. *Nature Communications*, *7*(1), 1–13. https://doi.org/10.1038/ncomms11148

Steinthorsdottir, M., Coxall, H. K., de Boer, A. M., Huber, M., Barbolini, N., Bradshaw, C. D., et al. (2020). The Miocene: The Future of the Past. *Paleoceanography and Paleoclimatology*, e2020PA004037.

Stoll, H. M., Guitian, J., Hernandez-Almeida, I., Mejía, L. M., Phelps, S., Polissar, P., et al. (2019). Upregulation of phytoplankton carbon concentrating mechanisms during low CO_2 glacial periods and implications for the phytoplankton pCO_2 proxy. *Quaternary Science Reviews*, *208*, 1–20. https://doi.org/10.1016/j.quascirev.2019.01.012

Su, B., Jiang, D., Zhang, R., Sepulchre, P., & Ramstein, G. (2018). Difference between the North Atlantic and Pacific meridional overturning circulation in response to the uplift of the Tibetan Plateau. *Climate of the Past*, *14*, 751–762. https://doi.org/10.5194/cp-14-751-2018

Super, J. R., Thomas, E., Pagani, M., Huber, M., O'Brien, C. L., & Hull, P. M. (2020). Miocene evolution of North Atlantic Sea surface temperature. *Paleoceanography and Paleoclimatology*, *35*. https://doi.org/10.1029/2019PA003748

Thiede, J., Jessen, C., Knutz, P., Kuijpers, A., Mikkelsen, N., Nørgaard-Pedersen, N., & Spielhagen, R. F. (2011). Millions of Years of Greenland Ice Sheet History Recorded in Ocean Sediments. *Polarforschung, Bremerhaven, Alfred Wegener Institute for Polar and Marine Research & German Society of Polar Research*, *80*(3), 141–159.

Thompson, S. L., & Pollard, D. (1997). Greenland and Antarctic mass balances for present and doubled atmospheric CO_2 from the GENESIS Version-2 Global Climate Model. *Journal of Climate*, *10*, 871–900. https://doi.org/10.1175/1520-0442(1997)010<0871:gaambf>2.0.co;2

Tierney, J. E., & Tingley, M. P. (2018). BAYSPLINE: A new calibration for the alkenone paleothermometer. *Paleoceanography and Paleoclimatology*, *33*(3), 281–301.

Uhl, D., Mosbrugger, V., Bruch, A., & Utescher, T. (2003). Reconstructing palaeotemperatures using leaf floras—Case studies for a comparison of leaf margin analysis and the coexistence approach. *Review of Palaeobotany and Palynology*, *126*(1–2), 49–64. https://doi.org/10.1016/s0034-6667(03)00058-7

Utescher, T., Bruch, A. A., Erdei, B., François, L., Ivanov, D., Jacques, F. M. B., et al. (2014). The coexistence approach—Theoretical background and practical considerations of using plant fossils for climate quantification. *Palaeogeography, Palaeoclimatology, Palaeoecology*, *410*, 58–73. https://doi.org/10.1016/j.palaeo.2014.05.031

Utescher, T., Djordjevic-Milutinovic, D., Bruch, A., Mosbrugger, V. (2007). Palaeoclimate and vegetation change in Serbia during the last 30 Ma. *Palaeogeography, Palaeoclimatology, Palaeoecology*, *253*, 141–152

Valcke, S. (2006). OASIS3 user's guide (prism-2–5) Tech. Rep. TR/CMGC/06/73, PRISM Report No 3. CERFACS.

Valdes, P. J., Armstrong, E., Badger, M. P. S., Bradshaw, C. D., Bragg, F., Crucifix, M., et al. (2017). The BRIDGE HadCM3 family of climate models: HadCM3@Bristol v1.0. *Geoscientific Model Development*, *10*, 3715–3743. https://doi.org/10.5194/gmd-10-3715-2017

Vincent, E., & Berger, W. H. (1985). Carbon dioxide and polar cooling in the Miocene: The Monterey hypothesis. *In The carbon cycle and atmospheric CO_2 natural variations Archean to present*, *32*, 455–468.

von der Heydt, A., & Dijkstra, H. A. (2006). Effect of ocean gateways on the global ocean circulation in the late Oligocene and early Miocene. *Paleoceanography*, *21*, PA1011. https://doi.org/10.1029/2005PA001149

Wang, W.-M. (2006). Correlation of pollen sequences in the Neogene palynofloristic regions of China. *Palaeoworld*, *15*, 77–99. https://doi.org/10.1016/j.palwor.2006.03.002

Warny, S., Askin, R. A., Hannah, M. J., Mohr, B. A., Raine, J. I., Harwood, D. M., & SMS Science Team. (2009). Palynomorphs from a sediment core reveal a sudden remarkably warm Antarctica during the middle Miocene. *Geology*, *37*(10), 955–958.

Weidick, A., Williams, R. S., & Ferrigno, J. G. (1995). Satellite image atlas of glaciers of the world: Greenland. US Government Printing Office.

Winkler, A., Wolf-Welling, T., Stattegger, K., & Thiede, J. (2002). Clay mineral sedimentation in high northern latitude deep-sea basins since the Middle Miocene (ODP Leg 151, NAAG). *International Journal of Earth Sciences*, *91*, 133–148. https://doi.org/10.1007/s005310100199

Wolfe, J. A. (1971). Tertiary climatic fluctuations and methods of analysis of Tertiary floras. *Palaeogeography, Palaeoclimatology, Palaeoecology*, *9*(1), 27–57. https://doi.org/10.1016/0031-0182(71)90016-2

Wolfe, J. A. (1985). Distribution of major vegetational types during the Tertiary. In E. T. Sundquist & W. S. Broecker (Eds.), *The carbon cycle and atmospheric CO_2: natural variations Archean*, Vol. 32 (pp. 357–375). American Geophysical Union Monograph. https://doi.org/10.1029/GM032p0357

Yang, J., Spicer, R. A., Spicer, T. E. V., & Li, C.-S. (2011). 'CLAMP Online': A new web-based palaeoclimate tool and its application to the terrestrial Paleogene and Neogene of North America. *Palaeobiodiversity and Palaeoenvironments*, *91*(3), 163. https://doi.org/10.1007/s12549-011-0056-2

You, Y., Huber, M., Müller, R. D., Poulsen, C. J., & Ribbe, J. (2009). Simulation of the middle Miocene climate optimum. *Geophysical Research Letters*, *36*(4). https://doi.org/10.1029/2008gl036571

Zachos, J. C., Dickens, G. R., & Zeebe, R. E. (2008). An early Cenozoic perspective on greenhouse warming and carbon-cycle dynamics. *Nature*, *451*(7176), 279–283. https://doi.org/10.1038/nature06588

Zachos, J. C., Pagani, M., Sloan, L., Thomas, E., & Billups, K. (2001). Trends, rhythms, and aberrations in global climate 65 Ma to present. *Science*, *292*(5517), 686–693. https://doi.org/10.1126/science.1059412

Zhang, X., Prange, M., Steph, S., Butzin, M., Krebs, U., Lunt, D. J., et al. (2012). Changes in equatorial Pacific thermocline depth in response to Panamanian seaway closure: Insights from a multi-model study. *Earth and Planetary Science Letters*, *317–318*, 76–84. https://doi.org/10.1016/j.epsl.2011.11.028

Zhang, Z., Nisancioglu, K. H., & Ninnemann, U. S. (2013). Increased ventilation of Antarctic deep water during the warm mid-Pliocene. *Nature Communications*, *4*, 1499. https://doi.org/10.1038/ncomms2521

Zhang, Z., Ramstein, G., Schuster, M., Li, C., Contoux, C., & Yan, Q. (2014). Aridification of the Sahara Desert caused by Tethys Sea shrinkage during the Late Miocene. *Nature*, *513*, 401–404. https://doi.org/10.1038/nature13705

Zhang, Z. S., Nisancioglu, K., Bentsen, M., Tjiputra, J., Bethke, I., Yan, Q., et al. (2012). Pre-industrial and mid-Pliocene simulations with NorESM-L. *Geoscientific Model Development*, *5*, 523–533. https://doi.org/10.5194/gmd-5-523-2012

Zhou, H., Helliker, B. R., Huber, M., Dicks, A., & Akçay, E. (2018). C4 photosynthesis and climate through the lens of optimality. *Proceedings of the National Academy of Sciences of the United States of America*, *115*(47), 12057–12062. https://doi.org/10.1073/pnas.1718988115

Zhu, J., & Poulsen, C. J. (2019). Quantifying the cloud particle-size feedback in an Earth System Model. *Geophysical Research Letters*, *46*(19), 10910–10917. https://doi.org/10.1029/2019GL083829

Zhu, J., Poulsen, C. J., & Tierney, J. E. (2019). Simulation of Eocene extreme warmth and high climate sensitivity through cloud feedbacks. *Science Advances*, *5*(9), eaax1874. https://doi.org/10.1126/sciadv.aax1874

References From the Supporting Information

Akgün, F., & Akyol, E. (1999). Palynostratigraphy of the coal-bearing Neogene deposits graben in Büyük Menderes Western Anatolia. *Geobios*, *32*, 367–383. https://doi.org/10.1016/s0016-6995(99)80013-8

Akgün, F., Kayseri, M. S., & Akkiraz, M. S. (2007). Palaeoclimatic evolution and vegetational changes during the Late Oligocene-Miocene period in Western and Central Anatolia (Turkey). *Palaeogeography, Palaeoclimatology, Palaeoecology*, *253*, 56–90. https://doi.org/10.1016/j.palaeo.2007.03.034

Axelrod, D. I. (1995). The Miocene Purple Mountain flora of western Nevada. University of California Publications in Geological Sciences, 139, 1–63.

Axelrod, D. I. (2000). A Miocene (10-12 Ma) Evergreen Laurel-Oak forest from Carmel Valley, California. University of California Publications in Geological Sciences.

Barrón, E., Rivas-Carballo, R., Postigo-Mijarra, J. M., Alcalde-Olivares, C., Vieira, M., Castro, L., et al. (2010). The Cenozoic vegetation of the Iberian Peninsula: A synthesis. *Review of Palaeobotany and Palynology*, *162*, 382–402. https://doi.org/10.1016/j.revpalbo.2009.11.007

Böhme, M., Bruch, A. A., & Selmeier, A. (2007). The reconstruction of Early and Middle Miocene climate and vegetation in Southern Germany as determined from the fossil wood flora. *Palaeogeography, Palaeoclimatology, Palaeoecology*, *253*, 91–114. https://doi.org/10.1016/j.palaeo.2007.03.035

Bruch, A., & Gabrielyan, I. (2002). Quantitative data of the Neogene climatic development in Armenia and Nakhichevan. *Acta Universitatis Carolinae: Geologica*, *46*, 41–48.

Bruch, A. A., Uhl, D., & Mosbrugger, V. (2007). Miocene climate in Europe – Patterns and evolution. *Palaeogeography, Palaeoclimatology, Palaeoecology*, *253*, 1–7. https://doi.org/10.1016/j.palaeo.2007.03.030

Chirilă, G., & Tabără, D. (2008). Palaeofloristic study of the Volhyian from Rasca (Moldavian Platform) – Palaeoclimatic and palaeoenvironmental implications. *Acta Palaeontologica Romaniae*, *6*, 29–42.

Chirilă, G., & Ţabără, D. (2010). Palynological study of the outcrop from the Ciofoaia Brook (Moldavian Platform) – Palaeoclimatic and palaeoenvironmental implications. Paper presented at International Symposium Geology of Natural Systems – Geo Iaşi 2010, 94–99.

Cramer, B. S., Miller, K. G., Barrett, P. J., & Wright, J. D. (2008). Late Cretaceous–Neogene trends in deep ocean temperature and continental ice volume: Reconciling records of benthic foraminiferal geochemistry ($\delta^{18}O$ and Mg/Ca) with sea level history. *Journal of Geophysical Research*, *116*(C12), C12023. https://doi.org/10.1029/2011jc007255

Deng, T., Hou, S., & Wang, H. (2007). The Tunggurian stage of the continental Miocene in China. *Acta Geologica Sinica - English Edition*, *81*, 709–721.

Denk, T., Grímsson, F., & Kvaček, Z. (2005). The Miocene floras of Iceland and their significance for late Cainozoic North Atlantic biogeography. *Botanical Journal of the Linnean Society*, *149*(4), 369–417. https://doi.org/10.1111/j.1095-8339.2005.00441.x

Dolan, A. M. (2012). Modelling mid-Pliocene climate and ice sheets (Ph. D. Thesis). University of Leeds.

Drury, A. J., Lee, G. P., Gray, W. R., Lyle, M., Westerhold, T., Shevenell, A. E., & John, C. M. (2018). Deciphering the state of the late Miocene to early Pliocene equatorial Pacific. *Paleoceanography and Paleoclimatology*, *33*(3), 246–263. https://doi.org/10.1002/2017pa003245

Dunn, R. E., Strömberg, C. A. E., Madden, R. H., Kohn, M. J., & Carlini, A. A. (2015). Linked canopy, climate, and faunal change in the Cenozoic of Patagonia. *Science*, *347*, 258–261. https://doi.org/10.1126/science.1260947

Emeis, K.-C., Schulz, H., Struck, U., Rossignol-Strick, M., Erlenkeuser, H., Howell, M. W., et al. (2003). Eastern Mediterranean surface water temperatures and $\delta^{18}O$ composition during deposition of sapropels in the late Quaternary. *Paleoceanography*, *18*(1). https://doi.org/10.1029/2000PA000617

Emeis, K.-C., Struck, U., Schulz, H.-M., Rosenberg, R., Bernasconi, S., Erlenkeuser, H., et al. (2000). Temperature and salinity variations of Mediterranean Sea surface waters over the last 16,000 years from records of planktonic stable oxygen isotopes and alkenone unsaturation ratios. *Palaeogeography, Palaeoclimatology, Palaeoecology*, *158*(3), 259–280. https://doi.org/10.1016/s0031-0182(00)00053-5

Erdei, B., Hably, L., Kázmér, M., Utescher, T., & Bruch, A. A. (2007). Neogene flora and vegetation development of the Pannonian domain in relation to palaeoclimate and palaeogeography. *Palaeogeography, Palaeoclimatology, Palaeoecology*, *253*, 115–140. https://doi.org/10.1016/j.palaeo.2007.03.036

Figueiral, I., Mosbrugger, V., Rowe, N. P., Utescher, T., Jones, T. P., & Von Der Hocht, F. (2002). Role of charcoal analysis for interpreting vegetation change and Paleoclimate in the Miocene Rhine Embayment (Germany). *PALAIOS*, *17*, 347–365. https://doi.org/10.1669/0883-1351(2002)017<0347:rocafi>2.0.co;2

Frederiksen, N. O. (1984). Stratigraphic, paleoclimatic and paleobiogeographic significance of Tertiary sporomorphs from Massachusetts. U.S. *Geological Survey Professional Paper*, *1308*, 1–25.

Fretwell, P., Pritchard, H. D., Vaughan, D. G., Bamber, J. L., Barrand, N. E., Bell, R., et al. (2012). Bedmap2: Improved ice bed, surface and thickness datasets for Antarctica. *The Cryosphere Discussions*, *6*(5), 4305–4361.

Gnibidenko, Z. N., Martynov, V. A., Nikitin, V. P., & Semakov, N. N. (1999). Magnetostratigraphic and paleobotanical description of the Miocene deposits in the Beshcheul Horizon of West Siberia. *Russian Geology and Geophysics*, *40*, 1776–1788.

Graham, A., Gregory-Wodzicki, K. M., & Wright, K. L. (2001). Studies in neotropical paleobotany. XV. A Mio-Pliocene palynoflora from the Eastern Cordillera, Bolivia: Implications for the uplift history of the Central Andes. *American Journal of Botany*, *88*, 1545–1557. https://doi.org/10.2307/3558398

Gregory-Wodzicki, K. M., McIntosh, W. C., & Velasquez, K. (1998). Climatic and tectonic implications of the late Miocene Jakokkota flora, Bolivian Altiplano. *Journal of South American Earth Sciences*, *11*, 533–560. https://doi.org/10.1016/s0895-9811(98)00031-5

Grímsson, F., Denk, T., & Símonarson, L. A. (2007). Middle Miocene floras of Iceland – The early colonization of an island? *Review of Palaeobotany and Palynology*, *144*(3–4), 181–219. https://doi.org/10.1016/j.revpalbo.2006.07.003

Guitián, J., Phelps, S., Polissar, P. J., Ausín, B., Eglinton, T. I., & Stoll, H. M. (2019). Midlatitude temperature variations in the oligocene to early Miocene. *Paleoceanography and Paleoclimatology*, *34*(8), 1328–1343. https://doi.org/10.1029/2019PA003638

Hartley, A. (2003). Andean uplift and climate change. *Journal of the Geological Society*, *160*(1), 7–10. https://doi.org/10.1144/0016-764902-083

Herbert, T. D., Ng, G., & Cleaveland Peterson, L. (2015). Evolution of Mediterranean Sea surface temperatures 3.5—1.5 Ma: Regional and hemispheric influences. *Earth and Planetary Science Letters*, *409*, 307–318. https://doi.org/10.1016/j.epsl.2014.10.006

Herbert, T. D., Peterson, L. C., Lawrence, K. T., & Liu, Z. (2010). Tropical ocean temperatures over the past 3.5 million years. *Science*, *328*, 1530–1534. https://doi.org/10.1126/science.1185435

Hobbs, K. M., & Parrish, J. T. (2016). Miocene global change recorded in Columbia River basalt-hosted paleosols. *The Geological Society of America Bulletin*, *128*, 1543–1554. https://doi.org/10.1130/b31437.1

Holbourn, A. E., Kuhnt, W., Clemens, S. C., Kochhann, K. G. D., Jöhnck, J., Lübbers, J., & Andersen, N. (2018). Late Miocene climate cooling and intensification of southeast Asian winter monsoon. *Nature Communications*, *9*(1), 1584. https://doi.org/10.1038/s41467-018-03950-1

Holbourn, A. E., Kuhnt, W., Regenberg, M., Schulz, M., Mix, A., & Andersen, N. (2010). Does Antarctic glaciation force migration of the tropical rain belt? *Geology*, *38*(9), 783–786. https://doi.org/10.1130/G31043.1

Holdgate, G. R., Cartwright, I., Blackburn, D. T., Wallace, M. W., Gallagher, S. J., Wagstaff, B. E., & Chung, L. (2007). The Middle Miocene Yallourn coal seam – The last coal in Australia. *International Journal of Coal Geology*, *70*, 95–115. https://doi.org/10.1016/j.coal.2006.01.007

Huang, Y., Clemens, S. C., Liu, W., Wang, Y., & Prell, W. L. (2007). Large-scale hydrological change drove the late Miocene C4 plant expansion in the Himalayan foreland and Arabian Peninsula. *Geology*, *35*(6), 531–534. https://doi.org/10.1130/G23666A

Hui, Z., Zhang, J., Ma, Z., Li, X., Peng, T., Li, J., & Wang, B. (2018). Global warming and rainfall: Lessons from an analysis of Mid-Miocene climate data. *Palaeogeography, Palaeoclimatology, Palaeoecology*, *512*, 106–117. https://doi.org/10.1016/j.palaeo.2018.10.025

Hüsing, S. K., Zachariasse, W.-J., van Hinsbergen, D. J. J., Krijgsman, W., Inceöz, M., Harzhauser, M., et al. (2009). Oligocene-Miocene basin evolution in SE Anatolia, Turkey: Constraints on the closure of the eastern Tethys gateway. *Geological Society, London, Special Publications*, *311*(1), 107–132. https://doi.org/10.1144/sp311.4

Iturralde-Vinent, M. A. (2006). Meso-Cenozoic Caribbean Paleogeography: Implications for the historical biogeography of the region. *International Geology Review*, *48*(9), 791–827. https://doi.org/10.2747/0020-6814.48.9.791

Ivanov, D. A., Ashraf, A. R., & Mosbrugger, V. (2007). Late Oligocene and Miocene climate and vegetation in the Eastern Paratethys area (northeast Bulgaria), based on pollen data. *Palaeogeography, Palaeoclimatology, Palaeoecology*, *255*, 342–360. https://doi.org/10.1016/j.palaeo.2007.08.003

Ivanov, D. A., Ashraf, A. R., Mosbrugger, V., & Palamarev, E. (2002). Palynological evidence for Miocene climate change in the Forecarpathian Basin (Central Paratethys, NW Bulgaria). *Palaeogeography, Palaeoclimatology, Palaeoecology*, *178*, 19–37. https://doi.org/10.1016/s0031-0182(01)00365-0

Jacobs, B. F., & Deino, A. L. (1996). Test of climate-leaf physiognomy regression models, their application to two Miocene floras from Kenya, and 40Ar/39Ar dating of the Late Miocene Kapturo site. *Palaeogeography, Palaeoclimatology, Palaeoecology*, *123*, 259–271. https://doi.org/10.1016/0031-0182(96)00102-2

Jarzen, D. M., Corbett, S. L., & Manchester, S. R. (2010). Palynology and paleoecology of the Middle Miocene Alum Bluff flora, Liberty County, Florida, USAPalynology. *Palynology*, *34*, 261–286.

Jiménez-Moreno, G. (2006). Progressive substitution of a subtropical forest for a temperate one during the middle Miocene climate cooling in Central Europe according to palynological data from cores Tengelic-2 and Hidas-53 (Pannonian Basin, Hungary). *Review of Palaeobotany and Palynology*, *142*, 1–14. https://doi.org/10.1016/j.revpalbo.2006.05.004

Karami, M. P. (2011). Paleoceanography of the Miocene Mediterranean Sea and Paratethys: Regional ocean modelling of the response to closure of the Tethys Seaway. Utrecht University.

Kayseri, M. S., & Akgün, F. (2010). The Late Burdigalian-Langhian interval in Turkey and the palaeoenvironmental and palaeoclimatic implications and correlation of Europe and Turkey: Late Burdigalian-Langhian palynofloras and palaeoclimatic properties of the Muğla-Milas (Kultak). *Geological Bulletin of Turkey*, *53*, 1–44.

Kayseri Özer, M. S., Sözbilir, H., & Akgün, F. (2014). Miocene palynoflora of the Kocaçay and Cumaovası basins: A contribution to the synthesis of Miocene palynology, palaeoclimate, and palaeovegetation in western Turkey. *Turkish Journal of Earth Sciences*, *23*, 233–259.

Kershaw, A. P. (1997). A bioclimatic analysis of early to middle Miocene brown coal floras, Latrobe Valley, south-eastern Australia. *Australian Journal of Botany*, *45*, 373–387. https://doi.org/10.1071/bt96033

Khan, M. A., Spicer, R. A., Bera, S., Ghosh, R., Yang, J., Spicer, T. E. V., et al. (2014). Miocene to Pleistocene floras and climate of the Eastern Himalayan Siwaliks, and new palaeoelevation estimates for the Namling-Oiyug Basin, Tibet. *Global and Planetary Change*, *113*, 1–10. https://doi.org/10.1016/j.gloplacha.2013.12.003

Kotthoff, U., Greenwood, D. R., McCarthy, F. M. G., Müller-Navarra, K., Prader, S., & Hesselbo, S. P. (2014). Late Eocene to middle Miocene (33 to 13 million years ago) vegetation and climate development on the North American Atlantic Coastal Plain (IODP Expedition 313, Site M0027). *Climate of the Past*, *10*, 1523–1539. https://doi.org/10.5194/cp-10-1523-2014

Kováčová, M., Hohenegger, J., & Ćorić, S. (2009). Palaeovegetation and climate based on pollen analysis of the Baden-Sooss section (Middle Miocene, Vienna Basin, Austria). In: In Filipescu, S., Ed. (Ed.), Paper presented at Third International Workshop Neogene of Central and South-Eastern Europe. Cluj University Press, Cluj-Napoca, 65

Langford, R. P., Wilford, G. E., Truswell, E. M., & Isern, A. R. (1995). Palaeogeographic Atlas of Australia. Australian Geological Survey Organisation. Canberra. Retrieved from https://www.ga.gov.au/resources/multimedia/animation/palaeo/html/palaeo.html

Larsson, L. M., Dybkjær, K., Rasmussen, E. S., Piasecki, S., Utescher, T., & Vajda, V. (2011). Miocene climate evolution of northern Europe: A palynological investigation from Denmark. *Palaeogeography, Palaeoclimatology, Palaeoecology*, *309*, 161–175. https://doi.org/10.1016/j.palaeo.2011.05.003

Lawrence, K. T. (2006). Characterizing the Plio-Pleistocene evolution of sea surface conditions using the alkenone organic proxy (PhD). Brown University.

Lawrence, K. T., Herbert, T. D., Brown, C. M., Raymo, M. E., & Haywood, A. M. (2009). High-amplitude variations in North Atlantic sea surface temperature during the early Pliocene warm Period. *Paleoceanography*, *24*. https://doi.org/10.1029/2008PA001669

Leopold, E. B., & Liu, G. (1994). A long pollen sequence of Neogene age, Alaska Range. *Quaternary International*, *22–23*, 103–140. https://doi.org/10.1016/1040-6182(94)90009-4

Levy, R., Harwood, D., Florindo, F., Sangiorgi, F., Tripati, R., von Eynatten, H., et al. (2016). Antarctic ice sheet sensitivity to atmospheric CO_2 variations in the early to mid-Miocene. *Proceedings of the National Academy of Sciences of the United States of America*, *113*(13), 3453–3458. https://doi.org/10.1073/pnas.1516030113

Liang, M. M., Bruch, A., Collinson, M., Mosbrugger, V., Li, C. S., Sun, Q. G., & Hilton, J. (2003). Testing the climatic estimates from different palaeobotanical methods: An example from the Middle Miocene Shanwang flora of China. *Palaeogeography, Palaeoclimatology, Palaeoecology*, *198*(3–4), 279–301. https://doi.org/10.1016/s0031-0182(03)00471-1

Liu, G., & Leopold, E. B. (1994). Climatic comparison of Miocene pollen floras from northern East-China and south-central Alaska, USA. *Palaeogeography, Palaeoclimatology, Palaeoecology*, *108*, 217–228. https://doi.org/10.1016/0031-0182(94)90235-6

Liu, Y.-S., Utescher, T., Zhou, Z., & Sun, B. (2011). The evolution of Miocene climates in North China: Preliminary results of quantitative reconstructions from plant fossil records. *Palaeogeography, Palaeoclimatology, Palaeoecology*, *304*, 308–317. https://doi.org/10.1016/j.palaeo.2010.07.004

Liu, Z., & Herbert, T. D. (2004). High-latitude influence on the eastern equatorial Pacific climate in the early Pleistocene epoch. *Nature*, *427*, 720–723. https://doi.org/10.1038/nature02338

Löwemark, L., Zheng, Y.-C., Das, S., Yeh, C.-P., & Chen, T.-T. (2016). A peculiar reworking of Ophiomorpha shafts in the Miocene Nangang Formation, Taiwan. *Geodinamica Acta*, *28*, 71–85. https://doi.org/10.1080/09853111.2015.1035208

Ma, Y. (1991). Tertiary sporo-pollen assemblages from southern Dunhuang Basin, Gansu Province. *Acta Micropalaeontologica Sinica*, *8*, 207–225.

Mao, X., & Retallack, G. (2019). Late Miocene drying of central Australia. *Palaeogeography, Palaeoclimatology, Palaeoecology*, *514*, 292–304. https://doi.org/10.1016/j.palaeo.2018.10.008

Meulenkamp, J. E., & Sissingh, W. (2003). Tertiary palaeogeography and tectonostratigraphic evolution of the Northern and Southern Peri-Tethys platforms and the intermediate domains of the African-Eurasian convergent plate boundary zone. *Palaeogeography, Palaeoclimatology, Palaeoecology*, *196*(1–2), 209–228. https://doi.org/10.1016/s0031-0182(03)00319-5

Milovanovic, D., & Mihajlovic, D. (1984). A Miocene flora from Zagubica basin, eastern Serbia. *Annales Geologiques de la Peninsule Balkanique*, *48*, 201–213.

Molnar, P. (2008). Closing of the Central American Seaway and the Ice Age: A critical review. *Paleoceanography*, *23*(2), PA2201.

Mosbrugger, V., Utescher, T., & Dilcher, D. L. (2005). Cenozoic continental climatic evolution of Central Europe. *Proceedings of the National Academy of Sciences of the United States of America*, *102*, 14964–14969. https://doi.org/10.1073/pnas.0505267102

Müller, R. D., Sdrolias, M., Gaina, C., & Roest, W. R. (2008a). Age, spreading rates, and spreading asymmetry of the world's ocean crust. *Geochemistry, Geophysics, Geosystems*, *9*(4), Q04006. https://doi.org/10.1029/2007gc001743

Müller, R. D., Sdrolias, M., Gaina, C., Steinberger, B., & H. CC. (2008b). Long-term sea-level fluctuations driven by ocean basin dynamics. *Science*, *319*(5868), 1357–1362. https://doi.org/10.1126/science.1151540

Nagy, E. (2005). Palynological evidence for Neogene climatic change in Hungary. *Ocassional Papers of the Geological Institute of Hungary*, *205*, 5–120.

Pantic, N. K. (1956). Biostratigraphie des flores tertiaires de Serbie. *Annales Geologiques de la Peninsule Balkanique*, *24*, 199–317.

Pantic, N. K., & Mihajlovic, D. S. (1977). Neogene floras of the Balkan land areas and their bearing on the study of palaeoclimatology, palaeobiogeography and biostratigraphy (Part 2). The lower Sarmatian flora of Beograd. Annales Geologiques de la Peninsule Balkanique, *Geološki anali Balkanskoga poluostrva*, *41*.

Pekar, S. F., & DeConto, R. M. (2006). High-resolution ice-volume estimates for the early Miocene: Evidence for a dynamic ice sheet in Antarctica, *Palaeogeography, Palaeoclimatology, Palaeoecology*, *231*(1–2), 101–109. https://doi.org/10.1016/j.palaeo.2005.07.027

Pollard, D., & DeConto, R. M. (2009). Modelling West Antarctic ice sheet growth and collapse through the past five million years. *Nature*, *458*(7236), 329–332. https://doi.org/10.1038/nature07809

Poore, H. R., Samworth, R., White, N. J., Jones, S. M., & McCave, I. N. (2006). Neogene overflow of Northern Component Water at the Greenland-Scotland Ridge. *Geochemistry, Geophysics, Geosystems*, *7*(6), Q06010. https://doi.org/10.1029/2005gc001085

Popova, S., Utescher, T., Gromyko, D., Bruch, A., & Mosbrugger, V. (2012). Palaeoclimate evolution in Siberia and the Russian Far East from the Oligocene to Pliocene—Evidence from fruit and seed floras. *Turkish Journal of Earth Sciences*, *21*, 315–334.

Prebble, J. G., Reichgelt, T., Mildenhall, D. C., Greenwood, D. R., Raine, J. I., Kennedy, E. M., & Seebeck, H. C. (2017). Terrestrial climate evolution in the Southwest Pacific over the past 30 million years. *Earth and Planetary Science Letters*, *459*, 136–144. https://doi.org/10.1016/j.epsl.2016.11.006

Reichgelt, T., Kennedy, E. M., Conran, J. G., Mildenhall, D. C., & Lee, D. E. (2015). The early Miocene paleolake Manuherikia: Vegetation heterogeneity and warm-temperate to subtropical climate in southern New Zealand. *Journal of Paleolimnology*, *53*, 349–365. https://doi.org/10.1007/s10933-015-9827-5

Retallack, G. J., & Kirby, M. X. (2007). Middle Miocene global change and paleogeography of Panama. *Palaios*, *22*, 667–679. https://doi.org/10.2110/palo.2006.p06-130r

Roeckner, E., Brokopf, R., Esch, M., Giorgetta, M., Hagemann, S., Kornblueh, L., et al. (2006). Sensitivity of simulated climate to horizontal and vertical resolution in the ECHAM5 atmosphere model. *Journal of Climate*, *19*, 3771–3791. https://doi.org/10.1175/jcli3824.1

Rommerskirchen, F., Condon, T., Mollenhauer, G., Dupont, L. M., & Schefuss, E. (2011). Miocene to Pliocene development of surface and subsurface temperatures in the Benguela current system. *Paleoceanography*, *26*(PA3216). https://doi.org/10.1029/2010PA002074

Rousselle, G., Beltran, C., Sicre, M.-A., Raffi, I., & De Rafélis, M. (2013). Changes in sea-surface conditions in the Equatorial Pacific during the middle Miocene-Pliocene as inferred from coccolith geochemistry. *Earth and Planetary Science Letters*, *361*, 412–421. https://doi.org/10.1016/j.epsl.2012.11.003

Scheiner, F., Holcová, K., Milovský, R., & Kuhnert, H. (2018). Temperature and isotopic composition of seawater in the epicontinental sea (Central Paratethys) during the Middle Miocene Climate Transition based on Mg/Ca, δ18O and δ13C from foraminiferal tests. *Palaeogeography, Palaeoclimatology, Palaeoecology*, *495*, 60–71. https://doi.org/10.1016/j.palaeo.2017.12.027

Seki, O., Schmidt, D. N., Schouten, S., Hopmans, E. C., Damsté, S., & Pancost, R. D. (2012). Paleoceanographic changes in the Eastern Equatorial Pacific over the last 10 Myr. *Paleoceanography*, *27*(3). https://doi.org/10.1029/2011PA002158

Shephard, G. E., Müller, R. D., Liu, L., & Gurnis, M. (2010). Miocene drainage reversal of the Amazon River driven by plate-mantle interaction. *Nature Geosciences*, *3*(12), 870–875. https://doi.org/10.1038/ngeo1017

Spicer, R. A., Harris, N. B. W., Widdowson, M., Herman, A. B., Guo, S., Valdes, P. J., et al. (2003). Constant elevation of Southern Tibet over the past 15 million years. *Nature*, *421*, 622–624. https://doi.org/10.1038/nature01356

Steinke, S., Groeneveld, J., Johnstone, H., & Rendle-Bühring, R. (2010). East Asian summer monsoon weakening after 7.5Ma: Evidence from combined planktonic foraminifera Mg/Ca and δ18O (ODP Site 1146; northern South China Sea). *Palaeogeography, Palaeoclimatology, Palaeoecology*, *289*(1), 33–43. https://doi.org/10.1016/j.palaeo.2010.02.007

Stevanovic, M. P., & Pantic, N. (1954). O sarmatskoj flori i fauni iz zeleznickih useka kod Bozdarevca, *Annales Geologiques de la Peninsule Balkanique*, *22*, 53–68.

Sun, X., & Wang, P. (2005). How old is the Asian monsoon system?—Palaeobotanical records from China. *Palaeogeography, Palaeoclimatology, Palaeoecology*, *222*, 181–222. https://doi.org/10.1016/j.palaeo.2005.03.005

Super, J. R., Thomas, E., Pagani, M., Huber, M., O'Brien, C., & Hull, P. M. (2018). North Atlantic temperature and pCO_2 coupling in the early-middle Miocene. *Geology*, *46*(6), 519–522. https://doi.org/10.1130/g40228.1

Syabryaj, S. (2002). Vegetation and climate of the Ukraine in the Neogene. *Acta Universitatis Carolinae: Geologica*, *46*, 49–55.

Syabryaj, S., Utescher, T., Molchanoff, S., & Bruch, A. A. (2007). Vegetation and palaeoclimate in the Miocene of Ukraine. *Palaeogeography, Palaeoclimatology, Palaeoecology*, *253*, 153–168. https://doi.org/10.1016/j.palaeo.2007.03.038

Takeuchi, A., Larson, P. B., & Suzuki, K. (2007). Influence of paleorelief on the Mid-Miocene climate variation in southeastern Washington, northeastern Oregon, and western Idaho, USA. *Palaeogeography, Palaeoclimatology, Palaeoecology*, *254*, 462–476. https://doi.org/10.1016/j.palaeo.2007.06.023

Tao, J.-J. (1997). The paleofloristic and paleoclimatic changes during the Mid-Miocene in China. In N. G. Jablonski, (Ed.), *The changing face of East Asia during the tertiary and quaternary*. The University of Hong Kong.

Tzanova, A., Herbert, T. D., & Peterson, L. (2015). Cooling Mediterranean Sea surface temperatures during the Late Miocene provide a climate context for evolutionary transitions in Africa and Eurasia. *Earth and Planetary Science Letters*, *419*, 71–80. https://doi.org/10.1016/j.epsl.2015.03.016

Uhl, D., Bruch, A. A., Traiser, C., & Klotz, S. (2006). Palaeoclimate estimates for the Middle Miocene Schrotzburg flora (S Germany): A multi-method approach. *International Journal of Earth Sciences*, *95*, 1071–1085. https://doi.org/10.1007/s00531-006-0083-9

Utescher, T., Djordjevic-Milutinovic, D., Bruch, A., & Mosbrugger, V. (2007). Palaeoclimate and vegetation change in Serbia during the last 30 Ma. *Palaeogeography, Palaeoclimatology, Palaeoecology*, *253*, 141–152. https://doi.org/10.1016/j.palaeo.2007.03.037

Utescher, T., Mosbrugger, V., & Ashraf, A. R. (2000). Terrestrial climate evolution in northwest Germany over the last 25 million years. *Palaios*, *15*, 430–449. https://doi.org/10.1669/0883-1351(2000)015<0430:tceing>2.0.co;2

van Ufford, A. Q., & Cloos, M. (2005). Cenozoic tectonics of New Guinea. *Bulletin*, *89*(1), 119–140. https://doi.org/10.1306/08300403073

Wang, P. (1990). Neogene stratigraphy and paleoenvironments of China. *Palaeogeography, Palaeoclimatology, Palaeoecology*, *77*, 315–334. https://doi.org/10.1016/0031-0182(90)90183-8

Wang, S., Shi, Q., Hui, Z., Li, Y., Zhang, J., & Peng, T. (2015). Diversity of Moschidae (Ruminantia, Artiodactyla, Mammalia) in the Middle Miocene of China. *Paleontological Research*, *19*(2), 143–155. https://doi.org/10.2517/2014pr032

Wheeler, E. A., Wiemann, M. C., & Fleagle, J. G. (2007). Woods from the Miocene Bakate Formation, Ethiopia. *Review of Palaeobotany and Palynology*, *146*, 193–207. https://doi.org/10.1016/j.revpalbo.2007.04.002

White, J. M., & Ager, T. A. (1994). Palynology, paleoclimatology and correlation of middle Miocene beds from Porcupine River (locality 90-1), Alaska. *Quaternary International*, *22–23*, 43–77. https://doi.org/10.1016/1040-6182(94)90006-x

Wiemann, M. C., Manchester, S. R., & Wheeler, E. A. (1999). Paleotemperature estimation from dicotyledonous wood anatomical characters. *PALAIOS*, *14*, 459–474. https://doi.org/10.2307/3515397

Wilson, D. S., Jamieson, S. S. R., Barrett, P. J., Leitchenkov, G., Gohl, K., & Larter, R. D. (2012). Antarctic topography at the Eocene-Oligocene boundary. *Palaeogeography, Palaeoclimatology, Palaeoecology*, *335–336*, 24–34. https://doi.org/10.1016/j.palaeo.2011.05.028

Wilson, D. S., & Luyendyk, B. P. (2009). West Antarctic paleotopography estimated at the Eocene-Oligocene climate transition. *Geophysical Research Letters*, *36*(16), L16302. https://doi.org/10.1029/2009gl039297

Yao, Y.-F., Bruch, A. A., Mosbrugger, V., & Li, C.-S. (2011). Quantitative reconstruction of Miocene climate patterns and evolution in Southern China based on plant fossils. *Palaeogeography, Palaeoclimatology, Palaeoecology*, *304*, 291–307. https://doi.org/10.1016/j.palaeo.2010.04.012

Zhang, Y. G., Pagani, M., & Liu, Z. (2014). A 12-million-year temperature history of the tropical Pacific Ocean. *Science*, *344*, 84–87. https://doi.org/10.1126/science.1246172

Zhang, Y. G., Pagani, M., Liu, Z., Bohaty, S., & DeConto, R. (2013). A 40-million-year history of atmospheric CO_2. *Philosophical Transactions of the Royal Society of London, Series A*, *371*. https://doi.org/10.1098/20130096

Zhao, L.-C., Wang, Y.-F., Liu, C.-J., & Li, C.-S. (2004). Climatic implications of fruit and seed assemblage from Miocene of Yunnan, southwestern China. *Quaternary International*, *117*, 81–89. https://doi.org/10.1016/s1040-6182(03)00118-6

Zhi-Cheng, L., Lin, A. T.-S., Shun-Wen, Y., Liao, T.-P., & Gui-Wen, X. (2013). Fossil seed from the Miocene Shihti formation of Taiwan. *Terrestrial, Atmospheric and Oceanic Sciences*, *24*, 731.